INVESTIGATION OF FLUORESCENCE LIFETIME IMAGING FOR QUANTITATIVE CERVICAL CANCER SCREENING AND DIAGNOSIS

GU JUN

SCHOOL OF ELECTRICAL AND ELECTRONIC ENGINEERING

A thesis submitted to the Nanyang Technological University
In partial fulfilment of the requirement for the degree of
Doctor of Philosophy

2014

To my beloved parents, Zhang You Yun (张有云) and Gu Yue Lan (顾月兰), you gave me everything. Special acknowledgement to my biological brother Zhang Jun (张俊), without you being my role model, I could not have achieved what I am today.

ACKNOWLEDGMENT

I want to acknowledge my supervisor Associate Professor Ng Beng Koon for his consistent guidance and support during my PhD studies. He is a young handsome gentleman, who is knowledgeable and insightful and discussions with him are always encouraging, inspiring and rewarding. He always encourages me to explore topics that genuinely interest me and he would point me to the right direction. My ability to work independently and think rigorously was intensively trained by him.

I would like to thank my group members Dr. Fu Chit Yaw, Dr. Benjamin Tay Chia Meng, Chow Tzu Hao and Dr. Srivathsan Vasudevan for the time we spent working and playing together. I want to appreciate Dr. Sirajudeen s/o Gulam Razul for his contribution of expertise in probability and stochastics to my research work.

I want to show my sincere gratitude to Dr. Lim-Tan Kim Soon, a senior histopathologist from KK Women's and Children Hospital for providing histological and cytological samples needed for cervical cancer studies. Discussions with her are always exciting and thought provoking and many new areas were identified in our meetings.

I would like to extend my deep thankfulness to Dr. Caroline G. Lee, National Cancer Center (NCC) for her generous sharing of the confocal laboratory facilities required in the fluorescence lifetime experiments. I want to acknowledge Mr. Gerald Chua, laboratory executive at NCC for providing good service consistently when I was using the laboratory facilities.

I am grateful to Yee Yang Boey Yvonne and Tsay Chi Huang, technical staff from Photonics Laboratory 1, Nanyang Technological University for providing fantastic laboratory support.

I owe special thanks to my parents, Zhang You Yun and Gu Yue Lan for all their cultivation, support, patience and love in my PhD study and my life since I was born.

TABLE OF CONTENTS

SUMMARY

To supplement the traditional histopathological examination of early cervical cancer, fluorescence lifetime imaging microscopy (FLIM) of H&E stained cervical tissue sections was investigated. Categories comprising normal, cervical intraepithelial neoplasia (CIN1, CIN2, CIN3), squamous cell carcinoma (SCC) and microinvasive were imaged and analyzed. Lifetime calculated from fluorescence emission decay in cervical epithelium region was used to correlate with tissue pathology. Mean and standard deviation of the characteristic fluorescence lifetime were used as feature vectors to feed into a neural network extreme learning machine (ELM) classifier for discrimination. An averaged sensitivity and specificity of 92.8% and 80.2%, respectively, were achieved when differentiating normal from precancerous (CIN1, CIN2, CIN3) samples. Discriminations between low-risk group (normal, CIN1) and high-risk group (CIN2, CIN3) were also conducted due to the clinical importance for treatment and a sensitivity of 85.0% and specificity of 87.6% were obtained. The results suggest that the proposed fluorescence lifetime imaging of H&E stained cervical tissue sections with the quantitative neural network ELM could be used to aid and supplement the traditional histopathological examinations.

Epithelial layer analysis of cervical fluorescence lifetime images was investigated to improve the diagnosis of H&E stained cervical tissue sections. The previously defined ROIs in cervical epithelium regions were divided into even layers in the tissue growth direction and diagnostic value in each of the divided layers was explored. It was found that feature vectors including a combination of the characteristic lifetime from the top-half epithelium gave the maximum diagnostic accuracy. Neural network ELM classifier

was used for discrimination and an averaged sensitivity of 94.6% and specificity of 84.3% were obtained when differentiating normal from precancerous cervical tissues. The proposed layer analysis technique has the advantage of achieving a concurrently higher sensitivity and specificity. In addition, analyzing only the top-half of the cervical epithelium shortens the calculation time. The proposed method can provide more accurate and faster cervical diagnosis, which can better supplement traditional gold standard histopathological examination.

Liquid based cytological (LBC) Papanicolaou test is a very effective pre-invasive tool to screen for cervical intraepithelial neoplasia (CIN). However, LBC has limited sensitivity and specificity. Fluorescence lifetime imaging modality was applied to study H&E stained LBC cells. The resulting lifetime images were processed to extract the whole cell and cytoplasmic regions for analysis. The result shows that whole cell fluorescence lifetime distribution is highly similar to the cytoplasmic region fluorescence lifetime distribution. The mean of the characteristic fluorescence lifetime in the whole cell region was used to differentiate between normal and precancerous cells. A concurrently high sensitivity and specificity of 92.6% and 71.2% were achieved, respectively. This preliminary study suggests that the proposed method can potentially supplement and improve the automated screening of cervical LBC samples.

The origin to the correlation between fluorescence lifetime changes and the associated cervical pathological states was investigated. Five proteins including BSA, poly-L-arginine, poly-L-histidine, poly-L-lysine and poly-L-tryptophan were used to simulate the proteins in cervical cytoplasm. Eosin Y, which is the only fluorophore involved in H&E staining, were used to bind with these proteins. Fluorescence lifetimes from the

bound protein-dye complex were measured and compared. It was found that fluorescence lifetime varied with the solution pH value and environment solvent. The results obtained are in good agreement with the lifetime shortening trend observed in H&E stained cervical tissue sections and the lifetime lengthening behavior found in LBC cells.

LIST OF FIGURES

LIST OF TABLES

LIST OF ABBREVIATIONS

ADC	Analog-to-Digital converter
AI	Artificial Intelligence
ANN	Artificial Neural Network
BP	Back Propagation
BSA	Bovine Serum Albumin
CFD	Constant Fraction Discriminator
CIN	Cervical Intraepithelial Neoplasia
CIRB	Committee and Institutional Review Board
CIS	Carcinoma-in-Situ
CGIN	Cervical Glandular Intraepithelial Neoplasia
DMSO	Dimethyl Sulphoxide
DNA	Deoxyribonucleic acid
DVI	Direct Visual Inspection
ELM	Extreme Learning Machine
FD	Frequency Domain
FLIM	Fluorescence Lifetime Imaging Microscopy
FNNS	Feedforward Neural Networks
H-CGIN	High-grade Cervical Glandular Intraepithelial Neoplasia
H&E	Haematoxylin and Eosin
HPV	Human Papilloma Virus
IRF	Instrumental Response Function
KKH	KK Women's and Children's Hospital
LBC	Liquid Based Cytological

L-CGIN	Low-grade Cervical Glandular Intraepithelial Neoplasia
LED	Light-Emitting Diode
MCA	Multichannel Analyzer
NA	Numerical Aperture
NLLS	Non-Linear Least-Square
OG	Orange G
Pap	Papanicolaou
PMT	Photomultiplier Tube
RBF	Radial Basis Function
ROIs	Region-of-Interests
SCC	Squamous Cell Carcinoma
SLFN	Single Hidden Layer Feedforward Neural Network
SNR	Signal-to-Noise Ratio
SVM	Support Vector Machine
TAC	Time-to-Amplitude Converter
TCSPC	Time-Correlated Single-Photon Counting
TD	Time Domain
TPE	Two-Photon Excitation
UV	Ultraviolet
WD	Window Discriminator

Chapter 1. INTRODUCTION

1.1 Motivation

Cervical cancer is the second most common cancer in women which accounts for about 12% of all female cancers and causes approximately 250,000 deaths every year [1]. The cervix carcinoma is often preceded by a long precancerous stage of 10 to 15 years and the most effective way to reduce cervical cancer incidence and mortality is early diagnosis and early treatment. The current routine way for early cervical cancer diagnosis is Papanicolaou (Pap) smear and histology, which examines the exfoliated cells and excised tissues from the cervix, respectively. In a Pap smear, cervical cells are scraped from the cervix wall and morphologically evaluated by a cytopathologist. However, the Pap smear has a low sensitivity and specificity and multiple Pap tests are required to reduce the false-negatives [2]. Cervical histology is subsequently followed for definitive diagnosis once abnormality is found in Pap smear. In histological diagnosis, a biopsy is collected from the patient and then fixed in formalin, dehydrated, mounted onto wax blocks, sectioned and stained with haematoxylin and eosin (H&E). Finally, an experienced histopathologist is required to evaluate the tissue under a microscope and this is still regarded as the gold standard for cervical cancer diagnosis [3, 4]. Both Pap smear and histology diagnosis have limitations of diagnostic variability cuased by subjective interpretations, dependence on professionally trained personnel, time-consuming and inaccuracy. Therefore, development of effective screening

protocols that are objective, independent on professionally trained personnel, fast and more accurate are demanded to diagnose cervical precancersou lesions.

Optical imaging, a promising imaging technique that uses light to assess optical properties of tissues, has been widely used in cancer diagnosis because of its advantages such as extreme low energy radiation, high sensitivity, accessibility and relatively cheap price. Imaging techniques such as reflectance spectroscopy [5], scattering spectroscopy [6] have been investigated in cervical cancer screening. As compared to these methods, fluorescence spectroscopy has many advantages: high sensitivity, minimized nosie due to filters to separate the excitation source and emission signal, endogenous fluorophores as well as exogenous fluorophores could be utilized for imaging. Disadvantages of fluorescence microscopy which might limit its clinical use are the relatively small number of fluorescent stains approved for use in human samples. Fluorescence lifetime imaging (FLIM) is a novel imaging technique that measures the temporal decay of fluorescence emission following a laser pulse excitation. The obtained fluorescence lifetime describes the average time that a fluorescent molecule stays in the excited state. The use of fluorescence lifetime rather than intensity has a number of advantages including the reduction of effects due to photobleaching, scattering and intensity variations in the excitation source. This characteristic lifetime is not only reliant on the fluorophore property but also on the micro-environment of the fluorescent compound. Parameters such as pH, temperature, viscosity and oxygen concentration [7-9] could be probed by measuring the fluorescence lifetime of the fluorophore. Therefore, lifetime values originating from intrinsic or exogenous fluorophores could be used to study tissue structure as well as tissue chemistry [10, 11]. In addition, as compared to traditional intensity-based fluorescence imaging technique, fluorescence lifetime is independent of

fluorophore concentration and laser excitation power. This allows for a wide variety of applications of FLIM in histopathological specimen examinations [12]. In this work, since samples are the H&E stained cervical tissues sections, the use of FLIM could probe many cervical cancer associated microenvironment parameters changes while minimum disruptions are caused to the samples because eosin gives fluorescence. The potential of FLIM in diagnosis could be fully explored while its drawback in the requirement for fluorophore is avoided. To the best of our knowledge, FLIM has never been used in cancer diagnosis of H&E stained cervical samples.

The whole thesis is structured under the target to solve the problems in early cervical cancer diagnosis which include diagnostic variability due to subjective interpretations, lack of well trained personnel, time-consuming and inaccurate followed by four major contents of experiments and analysis. The first work investigated the use of FLIM to diagnose H&E stained cervical tissue sections followed by the second work using an innovative way to analyze FLIM data in cervical epithelium to improve the diagnostic accuracy and reduce calculation time. Subsequently, the thesis explored using FLIM to diagnose Pap smear which is the earlier and less-invasive stage for cervical precancer diagnosis. Finally, the thesis wrapped up with a biochemical mechanism study to explain why FLIM could be used to diagnose early cervical cancer and to explain the data trend obtained in the fluorescence lifetimes of different tissue pathological types.

1.2 Objectives

The objectives of this thesis are:

a) Fluorescence lifetime characterization of H&E stained cervical tissue sections.

Traditional gold standard diagnosis of cervical cancer relies on visual inspection of morphological changes in H&E stained tissue sections. The aim of this work is to utilize fluorescence lifetime to probe the biochemical changes occurring in abnormal cervical tissues. A quantitative analysis of lifetime values was conducted to achieve objective and accurate diagnosis of cervical neoplasia. Successful implementation of fluorescence lifetime imaging to diagnose cervical cancer would supplement the traditional histopathological examination without alteration in the tissue preparation protocol.

b) Epithelial layer analysis for lifetime diagnosis of H&E stained cervical tissues.

Mean and standard deviation of lifetimes in the region of interest (ROI) of cervical tissue epithelium has proved to provide diagnostic information to supplement the traditional histopathological examination of early cervical cancer. The purpose of this work is to investigate the diagnostic value in the layered structures of H&E stained cervical tissue sections after these ROIs were evenly divided into layers. Effective feature vectors were used for discrimination and redundant feature vectors were excluded. The proposed layer analysis could potentially enhance the lifetime diagnostic accuracy and shorten the calculation time.

c) Fluorescence lifetime characterization of H&E stained cervical liquid based cytological (LBC) cells.

Conventional early cervical cancer diagnosis depends on microscopic examination of LBC cells. Automated screening overcomes the challenges of

traditional visual inspection. The motivation of this work is to harness fluorescence lifetime to detect the biochemical changes occurring in abnormal cervical cytological cells. Quantitative analysis of lifetime values was conducted to achieve objective and accurate diagnosis of cervical neoplasia. The proposed method could supplement the automated screening and improve the accuracy of LBC smears diagnosis.

d) Investigation of the biochemical mechanisms contributing to fluorescence lifetime diagnosis of cervical precancer.

The aim of this work is to explore the potential reasons that resulted in the lifetime changes among different H&E stained histological and cytological cervical samples.

1.3 Originality of thesis

The major originality and contributions of the thesis are summarized as follows:

1. Fluorescence lifetime imaging (FLIM) is an emerging fluorescence imaging technique in biomedical applications because of its sensitivity to biological microenvironment parameters. To the best of our knowledge, it is the first time to be investigated to diagnose H&E stained cervical tissue sections. Lifetimes for the whole range of cervical pathological states including normal, CIN1, CIN2, CIN3, squamous cell carcinoma (SCC) and microinvasive carcinoma were calculated. Fluorescence lifetime in cervical epithelium was found useful to be correlated to tissue histology. Mean and standard deviation of epithelium cell

lifetimes were used as feature vectors and a neural network extreme learning machine (ELM) classifier was used for tissue discrimination in order to distinguish between normal and precancerous (CIN1, CIN2, CIN3) samples. ELM could achieve very good generalization performance with extreme fast speed. Differentiation between low-risk (normal, CIN1) and high-risk groups (CIN2, CIN3) was also performed due to the clinical importance for treatment. The obtained high sensitivity and specificity suggest that the proposed fluorescence lifetime imaging of H&E stained cervical tissue sections with neural network ELM classifier could be used to aid and supplement the traditional histopathological examinations.

2. The diagnosis of H&E stained cervical tissue sections using fluorescence lifetime imaging was further investigated with epithelial layer analysis. Cervical epithelium was evenly divided into layers in the direction of tissue growth. Each divided layer was found to carry certain level of diagnostic information and a combination of fluorescence lifetime from some layers was used as feature vectors for discriminations. An improved diagnostic accuracy was achieved with a sensitivity of 94.6% and specificity of 84.3%, and the top-half epithelium was identified as the most effective zone for fluorescence lifetime diagnosis. The results suggest that the proposed layer analysis could enhance the diagnostic accuracy and shortens the calculation time for fluorescence lifetime diagnosis of H&E stained cervical tissue sections.

3. Fluorescence lifetime imaging was applied to study H&E stained liquid based cytological (LBC) Papanicolaou smear cells for the first time. Haematoxylin and

eosin were used to stain smear cells instead of the traditional multi-chromatic staining. Fluorescence lifetimes from cervical cells were collected and analyzed. Mean lifetimes in cellular regions were found to be correlated to cervical cytopathology and used as feature vectors. A concurrently high sensitivity and specificity of 92.6% and 71.2% were achieved, respectively. This preliminary study suggests that the proposed method could supplement and improve the automated screening of cervical LBC samples.

4. The origins to the correlation between fluorescence lifetime changes and the associated cervical pathological states were investigated. BSA and polyamino acids were used to simulate the proteins in cervical cytoplasm and bound with eosin Y, which is involved in the H&E staining protocol used in this thesis. Fluorescence lifetimes from the protein-dye complex were measured. It was found that solution pH and environment solvent changes the fluorescence lifetime. The result could explain the lifetime shortening and lengthening trends observed in H&E stained cervical tissue sections and LBC cells, respectively. This biochemical study also potentially laid the foundation for future clinical applications.

1.4 Organization of thesis

The thesis is organized into seven chapters as described below:

Chapter 1 presents the motivation, objectives, and major originality of the thesis.

Chapter 2 provides an overview of the fluorescence techniques. In particular, fluorescence lifetime imaging and TCSPC technique are discussed. Cervical cancer types, screening methods and extreme learning machine (ELM) classifier are also described.

Chapter 3 reports the use of fluorescence lifetime imaging to diagnose H&E stained cervical tissue sections. Lifetime feature vectors and discrimination classifier parameters are described. The lifetime distributions of cervical tissue sections are presented and the discrimination accuracy between different cervical histological stages is discussed.

Chapter 4 describes the use of layer analysis to further investigate fluorescence lifetime diagnosis of H&E stained cervical tissue sections. Epithelium regions are divided into even layers and the diagnostic information in each of these layers is explored. Feature vectors, comprising a combination of fluorescence lifetime from each layer, which were used to differentiate between normal and neoplastic samples, are elaborated in this chapter.

Chapter 5 deals with the use of fluorescence lifetime imaging modality to study H&E stained liquid based cytological (LBC) Papanicolaou smear cells. Lifetime characterization of cellular contents in the cytoplasm and whole cell regions are studied and discriminations are made between normal and precancerous LBC samples.

Chapter 6 presents the study of biochemical mechanism that leads to the diagnosis of H&E stained cervical tissue sections and LBC slides using fluorescence lifetime. The results obtained are presented and discussed in this chapter.

Chapter 7 concludes with the major findings obtained in this thesis and proposes future research directions in this area.

Chapter 2. BACKGROUND

2.1 Fluorescence

2.1.1 Overview

Fluorescence technique is one of the dominant methodologies with extensive usage for fundamental research in biology and biomedical sciences as well as in materials science. Fluorescence is the emission of light from a substance that has absorbed certain wavelength of light. It is the result of a three-stage process that occurs in fluorescent dyes or fluorophores following the absorption of a photon. The process that occurs between light excitation and light emission is illustrated by a simple electronic-state diagram, which is also known as Jablonski diagram [13], as shown in Figure 2-1. S_0, S_1 and S_2 represent the ground state, first and second excited electronic states, respectively. Within each of these electronic energy levels, fluorophores can exist in a series of vibrational level indicated as 0, 1 and 2. At room temperature, most of the fluorescent molecules would stay in the lowest vibration level of the ground state because thermal energy is not sufficient to pump them to higher energy levels.

Absorption is an instantaneous process where a fluorophore molecule in the ground state is excited to a higher energy state in either S_1 or S_2 by a photon with energy $h\nu_A$ provided by an external source such as an incandescent lamp or a laser. The transitions between energy states are depicted by vertical lines to illustrate the absorption process. Absorption takes place within a time of 10^{-15} s which is significantly faster than molecular vibration. Following light absorption, the fluorophore is promoted to any of

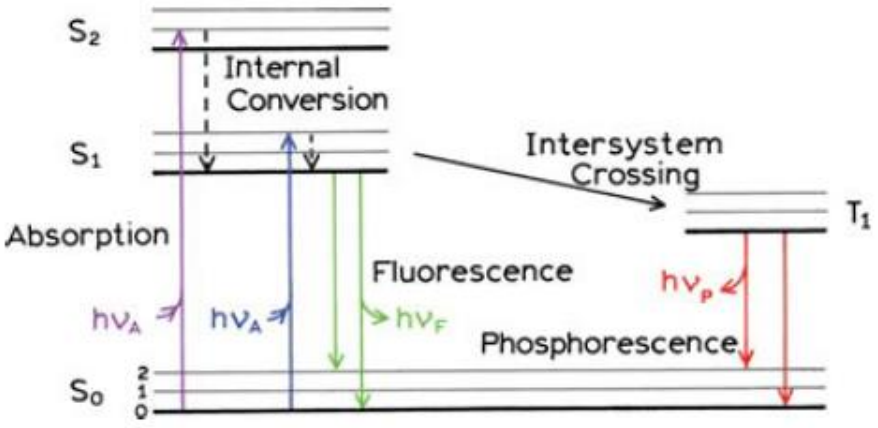

Figure 2-1 Jablonski diagram [13] illustrating the excitation and relaxation processes following light absorption.

the vibrational sub-levels associated with each electronic state. An excited state molecule can then undergo several processes such as vibrational relaxation, fluorescence, phosphorescence, internal conversion and intersystem crossing before it finally returns to its ground state.

The fluorophore molecule in one of the higher vibrational levels would rapidly lose its excess vibrational energy by collisions and drops to the lowest vibrational level of S_1. This process is known as internal conversion and it generally occurs within a time window of 10^{-12} s. This period of time is significantly shorter than fluorescence lifetimes of an excited state molecule which is typically 10^{-8} s. Internal conversion is a nonradiative process and the efficiency of internal conversion increases with decreasing energy gap between the initial and final energy level. Molecules in the S_1 state can also undergo a spin conversion to the first triplet state T_1 and the transition from S_1 to T_1 is called intersystem crossing. Light emission from T_1 is termed phosphorescence and the

wavelength is generally longer as compared to fluorescence. Transition from T_1 to singlet ground state is much less probable than singlet-singlet transition, and therefore phosphorescence has a longer average lifetime which ranges from 10^{-4} to 10 s or more [14].

Fluorescence, however, involves a transition from the lowest vibrational level of a higher excited energy state to any of the vibrational sub-levels of the ground state. Fluorophore molecules would return to the ground state and emit light. These molecules in a sub-level of the ground state would rapidly fall to the lowest vibrational level of the electronic ground state through vibrational relaxation and achieve thermal equilibrium.

2.1.2 Theory

2.1.2.1 Stokes' Shift

In fluorescence emission, vibrational energy is lost before electrons relax from the excited state to the ground state, which results in longer wavelengths in the emission fluorescence as compared to the excitation spectrum. This difference between the excitation and emission spectrum is known as the Stokes' shift. As Stokes' shift values increase, it becomes easier to separate excitation and emission light by using fluorescence filters. The fluorescence emission intensity peak is usually lower than that of the excitation peak and the emission spectrum is often a mirror image of the excitation spectrum as illustrated in *Figure 2-2*. The absorption and emission maxima of Alexa Fluor 555 are 555 nm and 565 nm, respectively, giving a Stokes' shift of about 10 nm. The Stokes' shift is an important characteristic of all fluorescent dyes as it allows the effective separation and detection of excitation and emission light through the proper

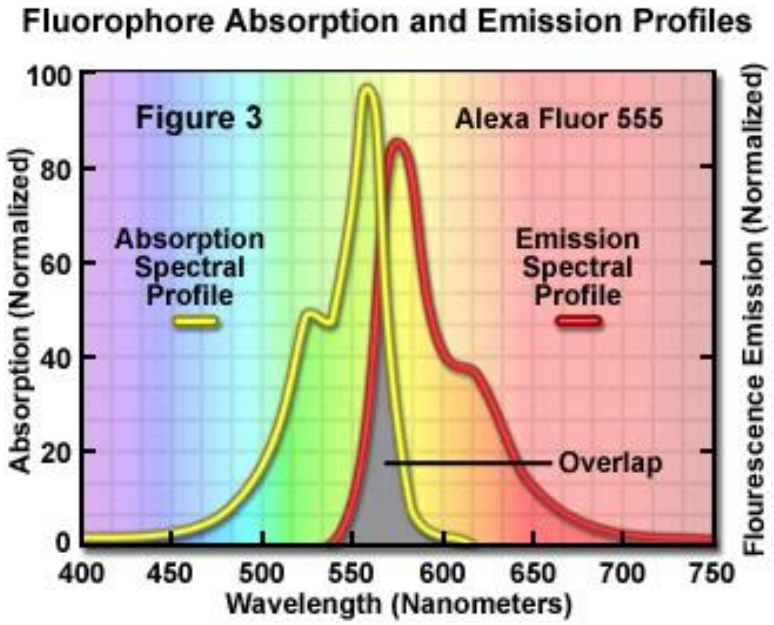

Figure 2-2 Absorption and emission spectrum for the fluorescent dye Alexa Fluor 555 [15]. The excitation and emission maxima are at the wavelengths of 555 nm and 565 nm, respectively.

selection of filters to block or pass certain wavelengths of light. This allows high sensitivity to be achieved in fluorescence microscopy since a low background noise is detected in fluorescence measurements.

2.1.2.2 The Beer-Lambert law

The Beer-Lambert law describes the absorption process when light passes through a medium. The absorbance, *A*, of the medium is the product of the concentration of absorbing medium (C), molar absorptivity (ε) and the distance the light travels in the medium (L) and is written as:

$$A = \varepsilon \cdot C \cdot L \tag{2-1}$$

The transmittance (*T*), which is defined as the ratio of incident light and transmitted light, is expressed as:

$$T = \frac{I}{I_0} = 10^{-\varepsilon CL} \tag{2-2}$$

where I and I_0 are the intensity of incident light and the transmitted light, respectively.

2.1.2.3 Fluorescence Quantum Yield

Fluorescence quantum yield Φ is defined as the number of emitted photons relative to the number of photons absorbed and is given by:

$$\Phi = \frac{\text{number of emitted photons}}{\text{number of absorbed photons}} = \frac{K_r}{K_r + K_{nr}} = \frac{\tau}{\tau_n} \tag{2-3}$$

where K_r and K_{nr} are the radiative and non-radiative decay rate constants, respectively. τ_n is the natural lifetime of the fluorophore and is also called the intrinsic lifetime without any non-radiative process. τ is the fluorescence lifetime and is the average value of time a fluorophore spends in the excited state. Quantum yield Φ measures the efficiency of the fluorescence process and the value falls within the range of 0 to 1. A high value of Φ approaching unity is generally associated with molecules possessing an extensive delocalized system of conjugated double bonds which result in a relatively rigid structure. This accounts for the strong fluorescence emission observed with molecules such as fluorescein, anthracene, perylene and other condensed ring aromatic structures [16]. In this case, the non-radiative decay rate is much smaller than the radiative decay rate and Φ is close to unity.

2.1.2.4 Two-photon Fluorescence Microscopy

Two-photon fluorescence microscopy is one of the most important biomedical imaging techniques because of its unique advantages of reduced specimen photodamage and increased tissue penetration depth [17]. It achieves noninvasive imaging of biological structures with submicrometer resolution in three dimensions. The physical principles of two-photon fluorescence microscopy involves the absorption of two photons simultaneously to excite a fluorescent molecule to a higher energy level [18]. Each photon possesses half the energy required to excite the fluorescent molecule. Since the probability of simultaneous absorption of two photons is extremely low, high power lasers such as mode-locked (pulsed) lasers are required to generate two-photon excited fluorescence. A key feature of two-photon fluorescence microscopy is that the excitation is limited within a femtoliter focal volume. This confines the two-photon induced absorption to the adjacent region of focal plane where the photon intensity is the highest. Therefore, two-photon excitation provides three-dimensional optical sectioning without absorption above and below the focus plane, which enables deep tissue imaging without photobleaching and phototoxicity.

2.1.3 Fluorescence Measurement Techniques

2.1.3.1 Steady-State Fluorescence

Fluorescence spectroscopy measurements are generally classified into two categories: steady-state and time-resolved. Steady-state measurement is the most common type which is performed with constant illumination and detection. The emission spectrum is recorded while the sample is constantly illuminated with a beam of light. Because

fluorescence emission occurs within a nanosecond timescale, steady state is reached almost instantly once the sample is exposed to light.

Steady-state fluorescence is usually measured by using a spectrofluorometer as shown in *Figure 2-3*. The spectrofluorometer consists of a Xenon arc lamp, a sample compartment, an excitation monochromator and an emission monochromator. The Xenon arc lamp provides light excitation with a quasi-constant intensity in the visible range. The excitation monochromator selects the excitation wavelength for sample illumination. In the sample compartment, a quartz cuvette is used to contain liquid samples, allowing transmission of the excitation light through the sample. The fluorescence emission derived from the sample is then collected and focused into the emission monochromator which is typically motorized to scan wavelengths automatically and is finally detected by a photomultiplier tube (PMT).

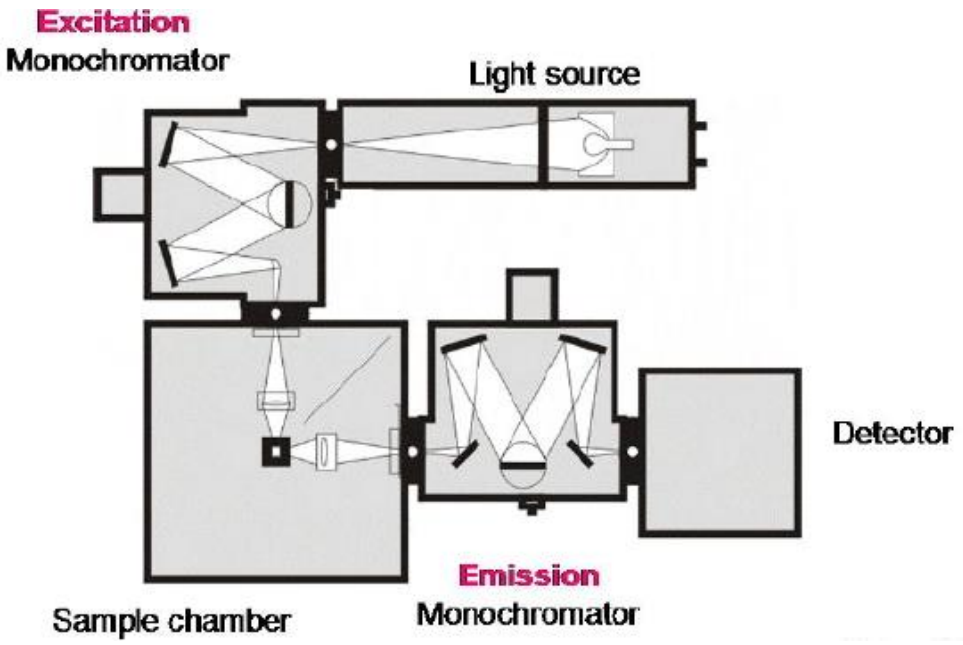

Figure 2-3 Schematic diagram of a typical spectrofluorometer [19].

2.1.3.2 Time-resolved Fluorescence

2.1.3.2.1 Overview

Although steady-state fluorescence measurements are much simpler than the complicated and expensive time-resolved fluorescence measurements, fluorescence lifetime could reveal much more molecular information that is lost during the averaging process involved in steady-state measurements [13]. Fluorescence lifetime is the average time a molecule resides in the excited state before returning to the ground state through fluorescence emission [20] and it is an intrinsic property of a fluorophore which is independent on conditions such as excitation light wavelength, duration of light exposure, fluorophore concentration and photobleaching [21]. However, the excited state fluorescence lifetime is highly sensitive to the microenvironment of the fluorescent molecules and valuable information about the molecular environment could be extracted by quantifying the fluorescence lifetime of the molecule. Thus, a number of research papers have been published regarding molecular effects measurements using fluorescence lifetime. Intracellular free calcium ion concentration (Ca^{2+}), which controls functions of cellular components, was measured by fluorescence lifetime [22]. Fluorescence lifetime changes were also used to explore local viscosity with molecular rotors [23], local refractive index derived structural information of biological specimen [24] and pH values [25]. In addition, fluorescence lifetime was found to vary on the binding of a fluorophore to a biological target such as proteins [26]. These features enable fluorescence lifetime measurement to be a powerful complementary method to the traditional steady-state technique. Fluorescence lifetime can generally be measured using the time domain (TD) [27, 28] or the frequency domain (FD) [29, 30] technique.

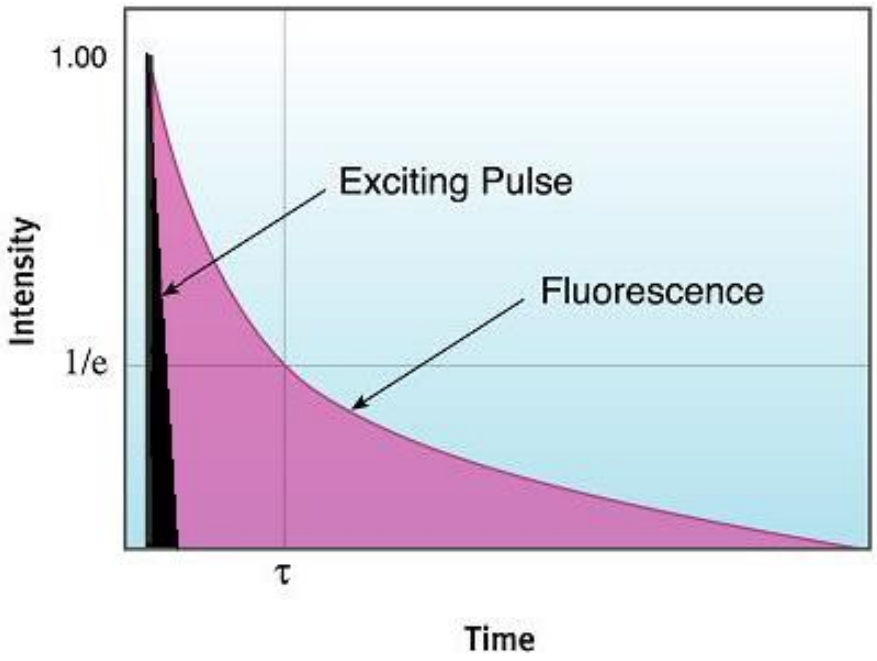

Figure 2-4 Single exponential decay of fluorescence intensity upon pulsed excitation.

In essence, the two methods are equivalent and can be converted to each other by a Fourier transform [31]. In the time-domain measurement (TD), a short light pulse is used to excite the sample and the impulse response of the fluorophore is recorded. The decay of the fluorescence intensity is recorded as a function of time. The pulse width is typically shorter than the sample decay time and high-speed electronic systems are required for detection. When a sample is excited by a short pulse of light, the resulting fluorescence intensity decays exponentially (as depicted in Figure 2-4). Lifetime τ is defined as the time when the intensity decreases to 1/*e* of its initial value.

For a fluorophore that exhibits a single exponential decay profile, the fluorescence intensity decay function *I (t)* is written as:

$$I(t) = I(0)\exp\left(-\frac{t}{\tau}\right) \quad (2\text{-}4)$$

where I (0) is the fluorescence intensity upon light pulse excitation (t=0), τ is the fluorescence lifetime.

At present, the Time-Correlated Single-Photon Counting (TCSPC) [32] is the most common time-domain measurement technique.

In FD measurements, the sample is typically excited with light intensity that is sinusoidally modulated. The modulation frequency is near 100 MHz so that its reciprocal frequency is comparable to the fluorescence decay time. The phase shift between the emission and excitation light is used to calculate the fluorescence lifetime.

Although the development of new, compact, cheap and less power-consuming laser diodes and light-emitting diodes (LEDs) have greatly reduced the complexity and cost of FD measurement instrumentation [33], the TCPSC technique achieves a better signal-to-noise (SNR) as compared to the FD measurement [34]. TCSPC is one of the most accurate methods of lifetime determination due to its short noise-limited detection, high photon economy, and low temporal jitter, high temporal precision and high dynamic range [35].

2.1.3.2.2 Time-Correlated Single Photon Counting

The first statistical study of TCSPC was introduced in 1968 [36]. In 1984, an extensive description of the TCSPC application in fluorescence lifetime was presented by

O'Connor and Philips [32]. In TCSPC, the sample is periodically excited by short light pulses and the subsequently emitted photons are observed. Pulse intensity is suitably adjusted so that less than 1 photon is detected for every 100 illumination light pulses. The emission photons are collected over multiple cycles of excitation and emission. In each emission event, the time difference between excitation and emission is recorded by electronics, which act like a stopwatch, as shown in Figure 2-5. The stopwatch readings are sorted into a histogram following a number of excitation pulses. The horizontal axis represents the time difference and the vertical axis shows the number of photons detected within this 'time bin'. From this histogram, the fluorescence intensity decay curve can be reconstructed.

The schematic diagram of a typical TCSPC collection system is illustrated in *Figure 2-6*. In the first channel, a light pulse from the laser excites the sample and goes through a constant function discriminator (CFD) to deliver a signal to the time-to-amplitude converter (TAC). The CFD measures the precise timing of the pulse reaching electronics while TAC is analogous to a fast stopwatch that measures the fluorescent photon arrival time. A voltage ramp starts to be generated which varies linearly with the time upon receiving the trigger signal from the laser pulse in the first channel. In the second channel, the pulse from the detected emission photon is fed to another CFD which sends a signal to the TAC to stop the voltage ramp. Therefore, the time delay between the excitation and emission signals is proportional to the voltage output from the TAC. The voltage is further amplified by a programmable gain amplifier (PGA) and converted to digital values by an analog-to-digital converter (ADC). The numerical values from the ADC are used to construct the histogram.

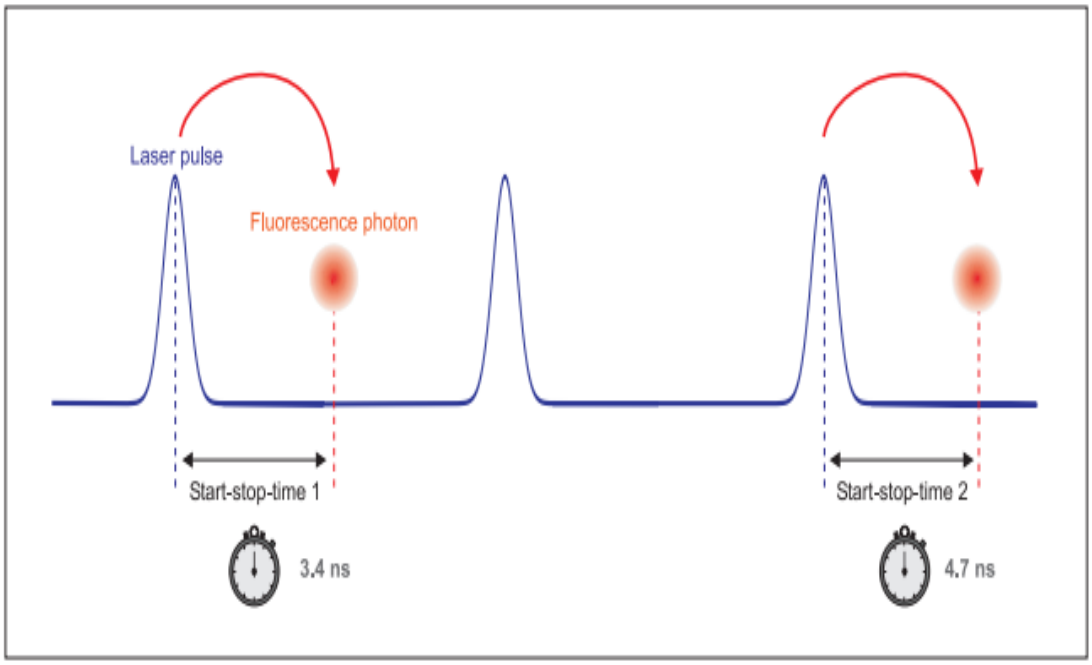

Figure 2-5 Fluorescence photon detection in time-resolved fluorescence measurement with TCSPC [37].

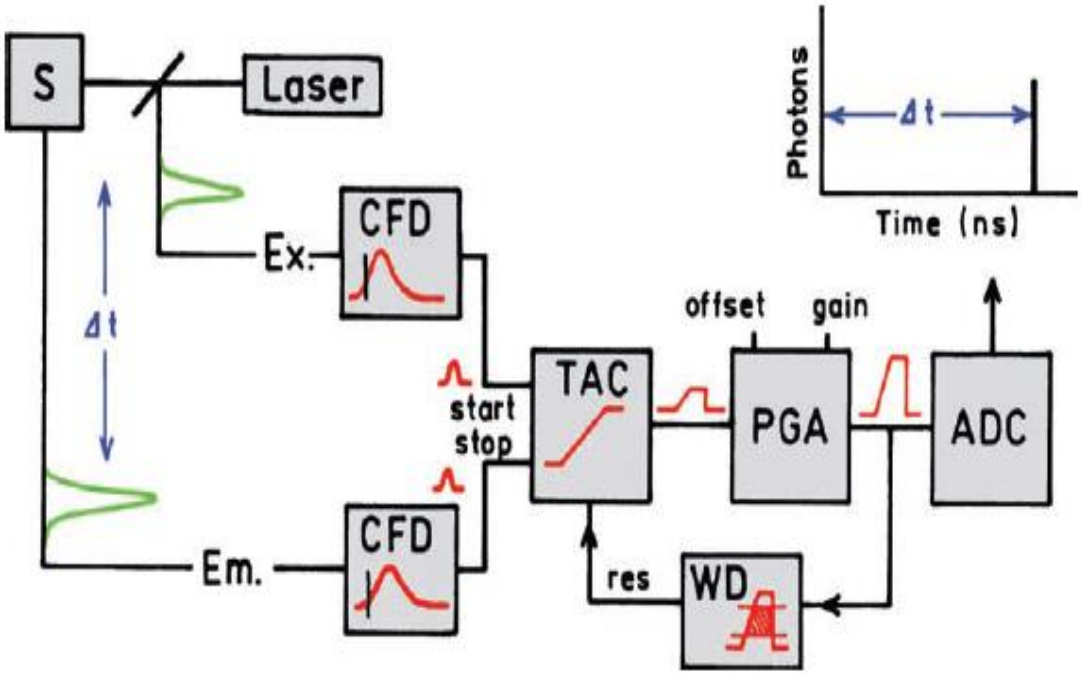

Figure 2-6 Schematic diagram of a TCSPC electronic system [13].

The window discriminator (WD) is applied to suppress voltages that are out of a given pre-defined voltage range which could minimize false readings.

The output of the TAC is subsequently digitized and sorted with respect to the time delay using a multichannel analyzer (MCA). A time histogram is constructed to represent the fluorescence decay profile after a large number of excitation and detection events are measured.

2.2 Cervical Cancer

2.2.1 Introduction

Cervical cancer is the second most common cancer among women which accounts for about 12% of all female cancers and causes approximately 250,000 deaths annually [1]. Nearly 78% of the mortality from the disease occurs in developing countries [38]. In the development of cervical cancer, sexually transmitted human papillomavirus (HPV) infections results in more than 90% of all cases [39]. The cervix is a cylindrical fibromuscular structure with variable length which measures 2.5 to 3.0 cm and approximately 2 to 2.5 cm in diameter [40]. It is part of the female reproductive system, which lies between the uterus and vagina. The central canal in the cervix has an external opening to the vagina and an internal opening to the uterus. These structures are also called the external os and internal os, as shown in Figure 2-7. The outer part of the cervix, which protrudes into the vagina, is known as the ectocervix and the part within the cervical canal is called the endocervix. The ectocervix is covered by stratified squamous epithelial cells while the endocervix is lined by tall columnar epithelial cells [19].

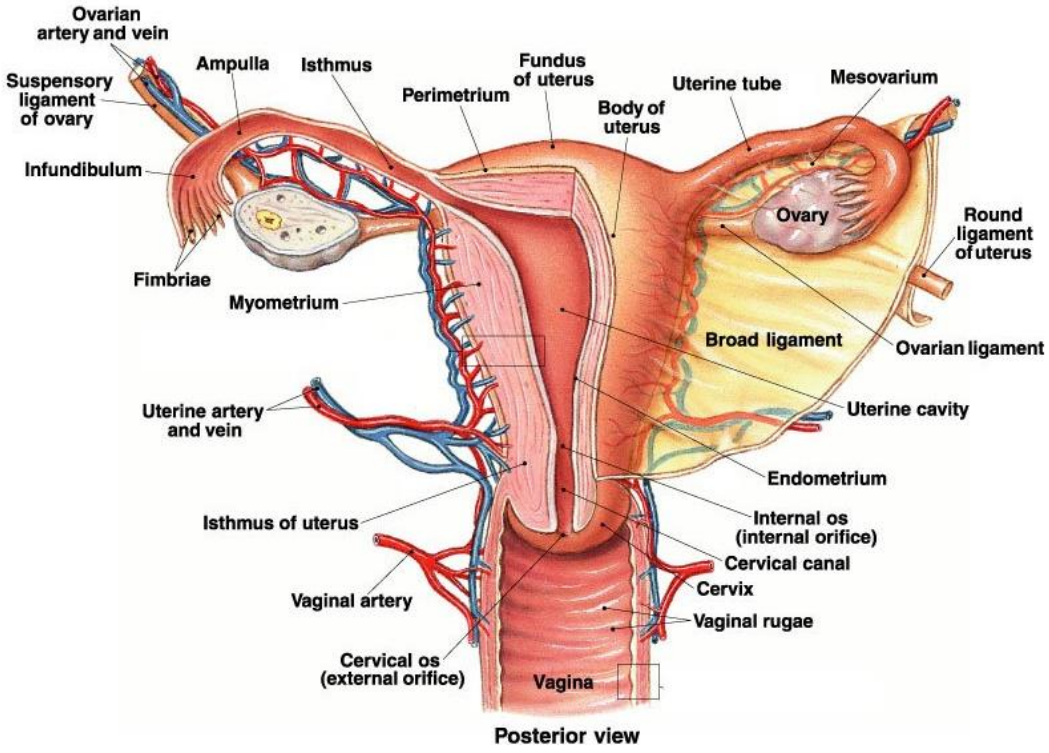

Figure 2-7 Anatomy of the female reproductive system [41].

The point of junction where the stratified squamous epithelium of the ectocervix and columnar lining of the endocervix meet is referred to as the squamocolumnar junction (see Figure 2-8). Metaplastic changes, which often happen in the squamocolumnar junction during reproductive life, are of crucial significance in cervical pathology. The term metaplasia refers to the process in which the squamous epithelium of the ectocervix replaces the columnar epithelium of the endocervix, which are normally replenished by reserve cell population. Metaplasia would cause movement of the squamocolumnar junction towards the internal os and constitutes the transformation zone which is defined as the area between the original and the new squamocolumnar junction. The appearance of metaplastic cells brings an increased risk of neoplastic changes in the transformation zone. The transformation zone is of particular interest to pathologists as most cervical cancers originate from this site [19].

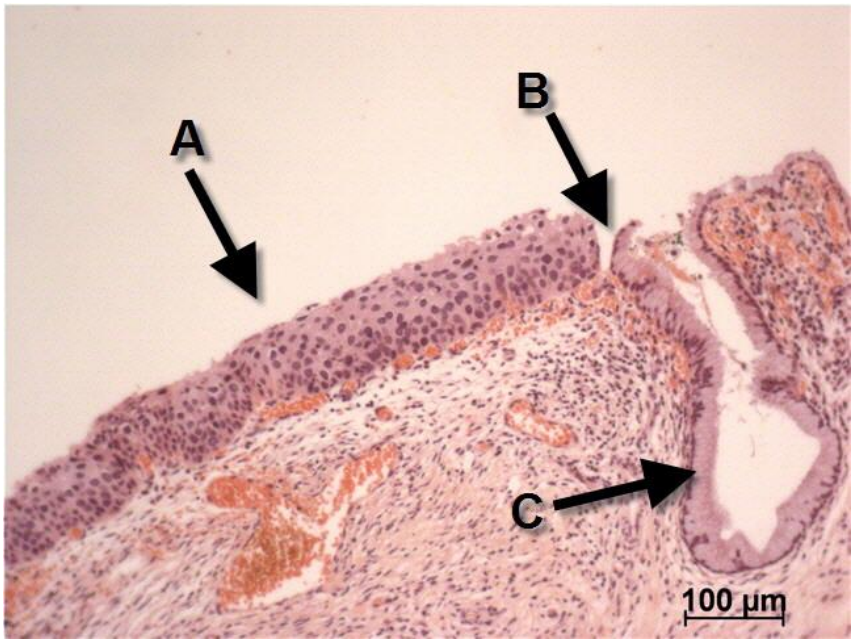

Figure 2-8 Histological image of a typical cervical squamocolumnar junction observed under 10× magnification. The squamous epithelium in the ectocervix, squamocolumnar junction and columnar epithelium in the endocervix are indicated by arrows at location A, B and C, respectively.

Squamous cell carcinoma (SCC) which arises from the squamous epithelial cells is the commonest histological type of cervical cancer, accounting for 85% of all invasive carcinoma cases. Adenocarcinoma, arising in glandular epithelial cells, is the second most common type which accounts for another 10%-15% of all cervical cancers [39]. Clinical invasive carcinoma usually presents with symptoms of abnormal vaginal bleeding, especially postcoital bleeding and vaginal discharge. Post-menopausal bleeding may be the main symptom after the menopause. Advanced disease is associated with signs of weight loss, debility and pain.

2.2.2 Histological Classification

The invasive carcinoma of the cervix is preceded by a long precancerous stage, a typical interval of 10-15 years, allowing early detection and treatment of cervical precancerous lesions possible. Precancerous changes in the epithelium of the ectocervix are usually described as cervical intraepithelial neoplasia (CIN) [41]. These preinvasive changes represent a continuous spectrum of morphology and are divided into three grades, CIN 1, CIN 2 and CIN 3, based on the proportion of the epithelium occupied by immature crowded cells with abnormal nuclei as shown in *Figure 2-9*. CIN 1 (mild dysplasia) refers to a lesion in which immature cells are confined to the lowest one third of the squamous epithelium. CIN 2 (moderate dysplasia) involves the middle third as well and in CIN 3 (severe dysplasia) the abnormal cells extend in to the upper third or replace the whole epithelium. When the immature abnormal cells occupy the full thickness of the epithelium without the invasion of tumor cells into the surrounding tissues, the lesion is called carcinoma *in situ* (CIS). Once the malignant cells penetrate through the underlying basement membrane and spread to the deeper tissue in the cervix or other parts of the body, the lesion is known as invasive cervical cancer [42].

Although squamous cell carcinoma (SCC) accounts for the majority of cervical cancer cases, adenocarcinoma, accounting for the minority of cervical cancers, is becoming more important in gynaecological oncology. The incidence of adenocarcinoma of the cervix has increased in recent decades as opposed to SCC, which has been declining. This is partially due to the difficulties in diagnosing adenocarcinoma which are probably because of a combination of cytology sampling obstacles and problems with cytological interpretations [43]. Most women diagnosed with cervical adenocarcinoma are in midlife and 20% of them are over the age of 65.

The endocervical canal is covered by the columnar epithelium which forms a single layer over the stroma. With the onset of dysplasia, cells in the layer are disrupted and pseudostratification starts to develop, which appears as overlapping crowding of nuclei in sheets of epithelial cells. The precursor lesions of endocervical adenocarcinoma are referred to as cervical glandular intraepithelial neoplasia (CGIN). Histological criteria for CGIN generally includes nuclear atypia such as nuclei enlargement, hyperchromasia, glandular chromatin and pseudostratification [44]. Unlike its squamous counterpart (CIN), CGIN is divided into low and high-grade lesions (L-CGIN, H-CGIN) as depicted in Figure 2-10. It generally takes 10 to 20 years for H-CGIN to develop into invasive carcinoma [45, 46].

2.2.3 Screening for the Prevention of Cervical Cancer

The early detection of precancerous lesions by cervical screening is one of the most effective ways to prevent cervical cancer. In the USA, cervical screening is usually conducted by using the Pap test [49] while in the UK the screening program was changed to liquid-based cytology (LBC) in 2008 [50]. In the conventional Pap smear, cervical cells were smeared by physicians to be mounted on a microscope slide and sent for laboratory examination. In LBC, collected cervical cells are placed into a vial containing a liquid medium to preserve the cells. The preserved cells are then processed to form a thin layer slide and stained for cytological evaluation. However, both cytological-based screening programs require sophisticated infrastructure, highly trained personnel and adequately equipped laboratories to be performed. Many women are barred from these screening programs especially those from the developing countries with poor-resource settings due to the intrinsic problems of cytological screenings [51].

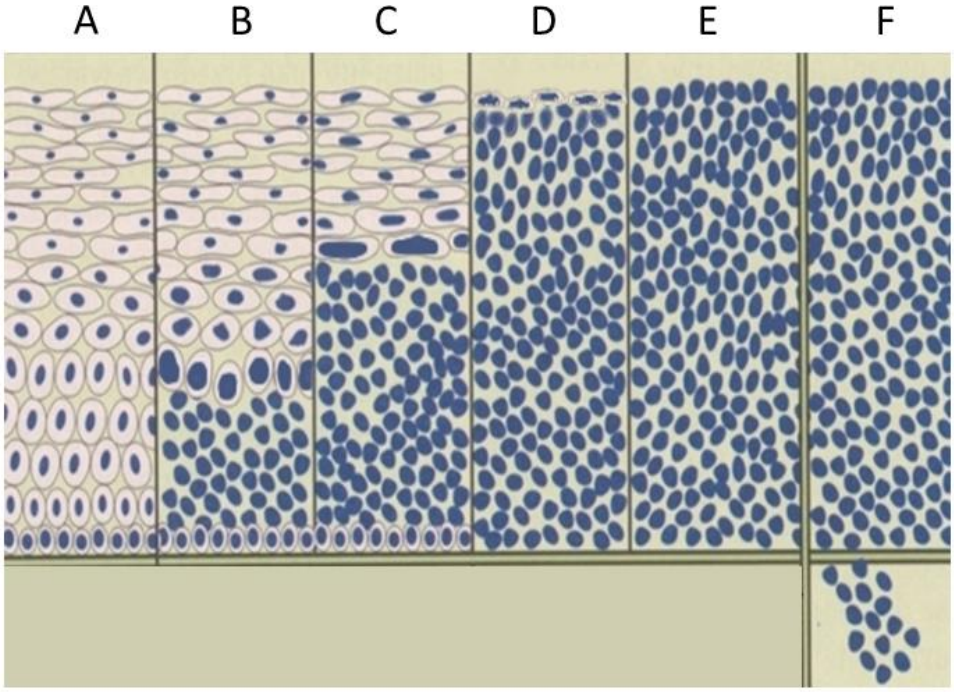

Figure 2-9 Illustrations depicting the histology of cervical tissues: (A) normal, (B) CIN1, (C) CIN 2, (D) CIN 3, (E) CIS, and (F) Invasive Cancer. Revised from [47].

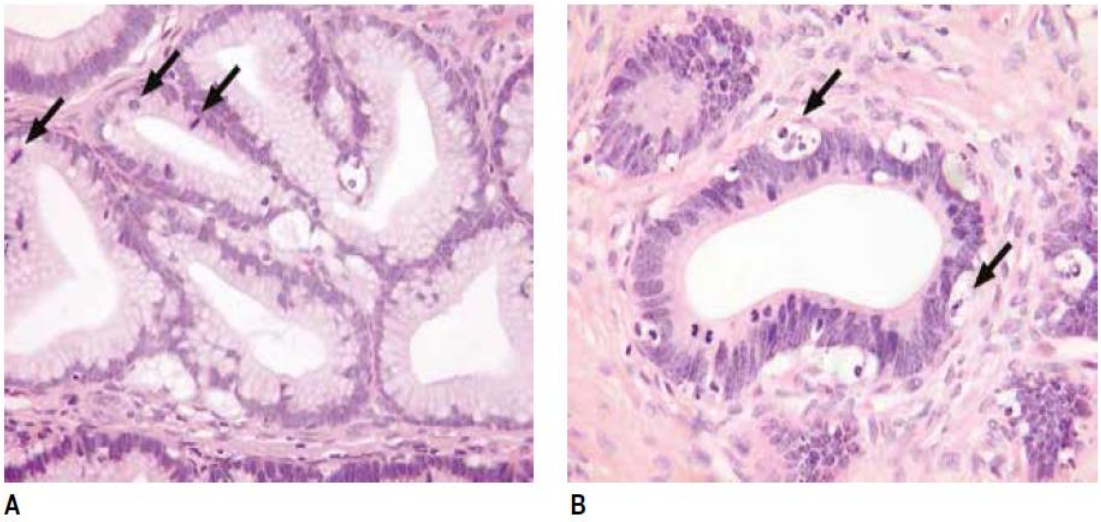

Figure 2-10 CGIN. (A) Low-grade CGIN. The endocervical glandular cells show mild nuclear atypia and hyperchromasia (arrows). (B) High-grade CGIN. The endocervical glandular cells show mucin depletion, nuclear stratification, atypia, hyperchromasia and loss of polarity with mitotic figures and apoptosis (arrows) [48].

Therefore, significant efforts have been made to develop alternative methods to support the existing screening methods such as the direct visual inspection (DVI) and human papillomavirus (HPV) DNA testing [52].

Colposcopy is subsequently conducted if the cytological screening result is positive. In colposcopy, the doctor would use a lighted magnifying device (colposcope) to look at the cervix. Acetic acid and sometimes iodine is applied on the cervix to improve the visual contrast of the problems areas. Once abnormal looking regions are identified, a small sample of the tissue (biopsy) is required to be taken from the cervix for further pathological examination. The main goal of colposcopy is to prevent carcinoma of the cervix by detecting precancerous lesions and treating them early [53].

2.3 Review of Lifetime Simulation in Tissues

2.3.1 Overview

To simulate the interactions between light and tissues and the resulting fluorescence lifetime, the most well-established method is the Monte Carlo simulation [54]. Monte Carlo simulation was regarded as the golden standard for modeling the light transport into the tissue, it used a simple photon propagation rule which is the probability distribution that describes the step size of photon movment and deflection angle in a photon's trajectory when scattering occurs. Photons are treated as particles and neither polarization nor wave phenomenons are considered in the simulation process. Monte Carlo simulations provides a flexible approach to calculate photon transportation in tissue provided physical variables in multiple tissue layers are given [54].

Macroscopic optical properties are assumed to extend uniformly over a small sample of tissue, lifetime difference among normal and cancerous tissues could be simulated by using the different scattering (μ_s) and absorption (μ_a) coefficients and the anisotropy factor (g). In the simulation, a narrow photon beam was typically used to simulate laser that transport perpendicularly on a multi-layered tissue. Each tissue is considered infinitely wide and characterized by thickness, refraction index, μ_a, μ_s, and g. Absorption coefficient μ_a is defined as the probability on photon absorption per unit infinitesimal path length whiel the scattering coefficient μ_s is defined as the probability of photon scattering per unit infinitesimal path length. The anisotropy factor is the average of cosine value of the deflection angle. In the simulation of fluorescence lifetime, the main concern is to calculate the time that a photon stay in the tissue before it is re-emitted or absorbed by the tissue.

2.3.2 Lifetime Simulation in H&E stained tissue sections

To simulate light transportation in tissue, a good knowledge of tissue properties is essential. Tissues are formed by a group of special cell types bounded together. These cell functions are coordinated to allow the tissue to perform its given task. There are many constituents of a tissue sucha as cell-adhesino molecules (CAM), extra-cellular matrix (ECM) and cell junctions [55]. These tissues might be composed of many cells types such as absorptive cells, mucosal cells, blood cells, etc. which makes tissue parameters complicated.

In addition, fluorescence lifetime is very sensitive to parameters of the tissue such as thickness, color, area where the tissue is taken. All these would change the absorption

and scattering coefficients of the tissue, and so far a comprehensive and consistent database that contains tissue parameters of various pathological tissue types is not available although there are values of tissue property from different resources [56]. Although Monte Carlo simulations on cervical autofluorescence have been conducted to compare spectra of tissues with different pathological states using these scattered parameters, no fluorophore and protein binding is involved in the simulations [57]. While in our case, we are dealing with H&E stained tissues, in which a more complicated biochemical interaction such as protein binding have occurred which would also change these parameters. Such data are presently not available in the literature. To be able to carry out the simulation work in this thesis, tissue parameters have to be measured under different conditions and the protein dye binding mechanism and the associated model have to be firstly investigated and established.

2.4 Extreme Learning Machine Classifier

2.4.1 Overview

Machine Learning, a branch of artificial intelligence (AI), has been widely studied by researchers to construct and study systems that can be learned from data [58-60]. Machine learning is a collection of algorithms developed to interpret and unveil the unknown relationship among the real world massive data. Machine learning is widely applied in areas such as regression analysis [61], classification and data processing [62].

One big challenge in machine learning is how to learn the complicated pattern or trend from the unknown training data. The artificial neural networks (ANNs), commonly referred to as 'neural network', is one of the most effective machine learning techniques that was designed by inspiration from the human brain [63]. ANNs mimic the biological neural network and its structure and operation principles attempt to emulate the human nervous system. The input data is processed in basic units referred to as ‘neurons’ by powerful computational functions. Subsequently, a network with complicated interconnections between the neurons is constructed to store the learning information for any specific application. There are different types of neural network structures such as feedforward neural network (FNNS) and recurrent neural network, depending on how these neurons are interconnected. Among those structures, feedforward neural networks are the mostly extensively studied. The single hidden layer feedforward neural network (SLFN) is the simplest form of FNN and is shown in *Figure 2-11*. There are generally three layers: the input layer, the hidden layer and the output layer. The input layer absorbs the input data and transfers them to the hidden layer where input data are processed and the output is then displayed though the output layer. The traditional learning process of a SLFN is conducted by iterative tuning of parameters in the hidden layer. However, the tuning process is tedious and time-consuming and it normally suffers from problems such as local minimum and slow convergence rate [64].

Extreme Learning machine (ELM), originally proposed as a learning algorithm for the single hidden layer feedforward neural networks, is able to solve all the above mentioned problems [65-67]. The most prominent feature of ELM is that its hidden nodes are randomly assigned while hidden nodes’ parameters in traditional SLFN were

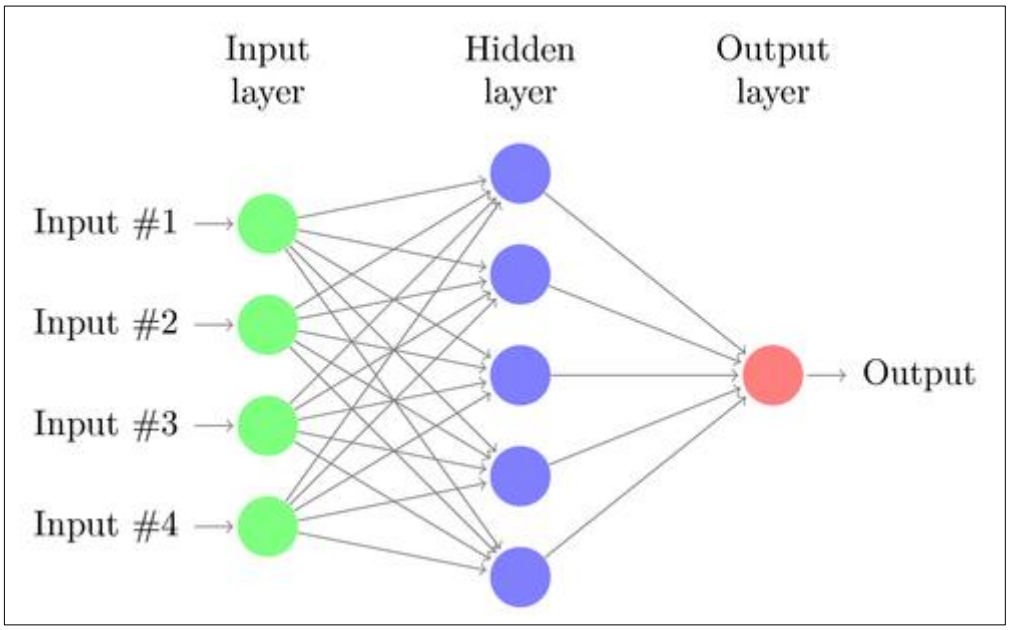

Figure 2-11 A typical structure of a single hidden layer feedforward neural network (SLFN)

iteratively tuned. ELM is a constructive method that allows SLFNs to approximate any type of continuous functions instead of a specific type of functions in [68].

ELM family have many algorithms such as I-ELM [68], CI-ELM [69], EI-ELM [70], etc. They all have been thoroughly tested on real world datasets and shown to achieve good training and validation errors.

In ELM, the output weight is analytically determined as the solution of a linear system and universal approximation is guaranteed. Therefore, an ELM could achieve extremely fast speed and phenomenal generalization performance.

However, in many applications, ELM produces better results than SVM and the calculation time can be thousands time faster [67, 70, 72]. For example, in one application, the performance of ELM, SVM and BP algorithms were compared in the evaluation of median house value in California based on 8 input parameters such as median income, population, total rooms, etc. All simulations were carried out in Matlab 6.5 environment running in a Pentium 4, 1.9 GHZ CPU. In this case, the learning speed of ELM is more than 1000 and 2000 times faster than BP and SVM [67].

2.4.2 ELM Algorithm

2.4.2.1 Single hidden layer feedforward networks

ELM was initially proposed to train single hidden layer feedforward neural networks (SLFNs) in which there is only one layer of hidden nodes [70]. The output of an SLFN with L hidden nodes and input **x** can be expressed as:

$$f_L(\mathbf{x}) = \sum_{i=1}^{L} \beta_i g_i(\mathbf{x}) = \sum_{i=1}^{L} \beta_i G(\mathbf{x}, \mathbf{a}_i, b_i) \qquad (2\text{-}5)$$

$$\mathbf{a}_i \in C^d, \mathbf{x}_i \in \c{C}^d, b_i \in C, \beta_i \in C$$

where β_i is the output weight of the *i*th hidden node, $g_i(\mathbf{x})$ or $G(\mathbf{x},\mathbf{a}_i,b_i)$ is the output function of the *i*th hidden node, $\mathbf{a}_i$ is the weight vector connecting the *i*th hidden node and the input nodes and b_i is the threshold of the *i*th hidden node. The output functions differ as the node type changes. There are various kinds of nodes, such as additive or radial basis function (RBF) type of nodes, multiplicative nodes, fuzzy nodes, fully

complex nodes, high-order nodes, wavelets and ridge polynomials. The activation functions of the three most common neuron nodes are:

Additive hidden nodes: $g_i(\mathbf{x}) = g(\mathbf{a}_i \cdot \mathbf{x} + b_i), \mathbf{a}_i \in R^d, \mathbf{x} \in R^d, b_i \in R,$

RBF hidden nodes: $g_i(\mathbf{x}) = g(b_i|\mathbf{x} - \mathbf{a}_i|), \mathbf{a}_i \in R^d, \mathbf{x} \in R^d, b_i \in R,$

Fully complex hidden nodes: $g_i(\mathbf{x}) = \prod_{i=1}^{S_i} g(\mathbf{a}_{ij} \cdot \mathbf{x} + b_i)), \mathbf{a}_{i,j} \in R^d, \mathbf{x} \in R^d, b_i \in R,$ (2-6)

where g is the activation function and s_i is an integer constant.

2.4.2.2 Extreme Learning Machine Operational Principle

The ELM operation is based on the theory that SLFNs with randomly generated hidden nodes are universal approximators [72]. The activation function for additive nodes can be any bounded non-constant piecewise continuous functions and the activation function for RBF nodes can be any integral piecewise continuous functions.

Suppose there are N distinct training samples ($\mathbf{x}_i$, t_i) in ELM; then the output with *L* hidden nodes is:

$$f(\mathbf{x}) = \sum_{j=1}^{L} \beta_j G(\mathbf{a}_j, b_j, \mathbf{x}) = \beta \cdot h(\mathbf{x}) \quad (2\text{-}7)$$

where $h(\mathbf{x}) = [G(\mathbf{a}_1, b_1, \mathbf{x}), \cdots G(\mathbf{a}_L, b_L, \mathbf{x})]^T$ is the output vector for the hidden layer and **x** is the input. Parameters in the hidden nodes $(\mathbf{a}_j, b_j, j = 1, \cdots, L)$ are randomly assigned and the output weight β_j is determined analytically by using the following formula:

$$\mathbf{H} \cdot \beta = \mathbf{T} \tag{2-8}$$

where

$$\mathbf{H}(\mathbf{a}_1, \cdots, \mathbf{a}_L; b_1, \cdots, b_L; \mathbf{x}_1, \cdots, \mathbf{x}_N) = \begin{bmatrix} G(\mathbf{a}_1, b_1, \mathbf{x}_1) & \cdots & G(\mathbf{a}_L, b_L, \mathbf{x}_1) \\ \vdots & \cdots & \vdots \\ G(\mathbf{a}_1, b_1, \mathbf{x}_N) & \cdots & G(\mathbf{a}_L, b_L, \mathbf{x}_N) \end{bmatrix}_{N \times L}$$

$$\beta = \begin{bmatrix} \beta_1^T \\ \vdots \\ \beta_L^T \end{bmatrix}_{L \times d} \qquad \mathbf{T} = \begin{bmatrix} \mathbf{t}_1^T \\ \vdots \\ \mathbf{t}_L^T \end{bmatrix}_{N \times d} \tag{2-9}$$

H is the hidden layer output matrix with the i^{th} row representing the output vector of hidden layer with respect to input $\mathbf{x}_i$ and the j^{th} column representing the output of the j^{th} hidden node with regard to all the inputs $(\mathbf{x}_1, \cdots \mathbf{x}_N)$. The least square solution $\hat{\beta}$ is calculated in ELM so that the training error is minimum.

$$\left| \mathbf{H} \cdot \hat{\beta} - \mathbf{T} \right| = \min_{\beta} \left| \mathbf{H} \cdot \beta - \mathbf{T} \right| \tag{2-10}$$

$\hat{\beta}$ is calculated using the following formula:

$$\hat{\beta} = \mathbf{H}^{\Theta} \mathbf{T} \tag{2-11}$$

where $\mathbf{H}^{\Theta}$ is the Moore-Penrose generalized inverse of hidden layer output matrix **H** which achieves the smallest norm of β and minimizes the training error at the same time. In theory, the least square solution of minimum norm β is unique [73, 74].

Accordingly, the training process of ELM involves three steps (as shown in *Figure 2-12*) once a training data ($\mathbf{x}_i$,t_i), i=1, ⋯;N is given:

1) Generate L hidden nodes with parameters (**a**,b) of each node randomly assigned;

2) Calculate the hidden layer output matrix **H**;

3) Calculate the output weight $\hat{\beta} = \mathbf{H}^{\Theta}\mathbf{T}$

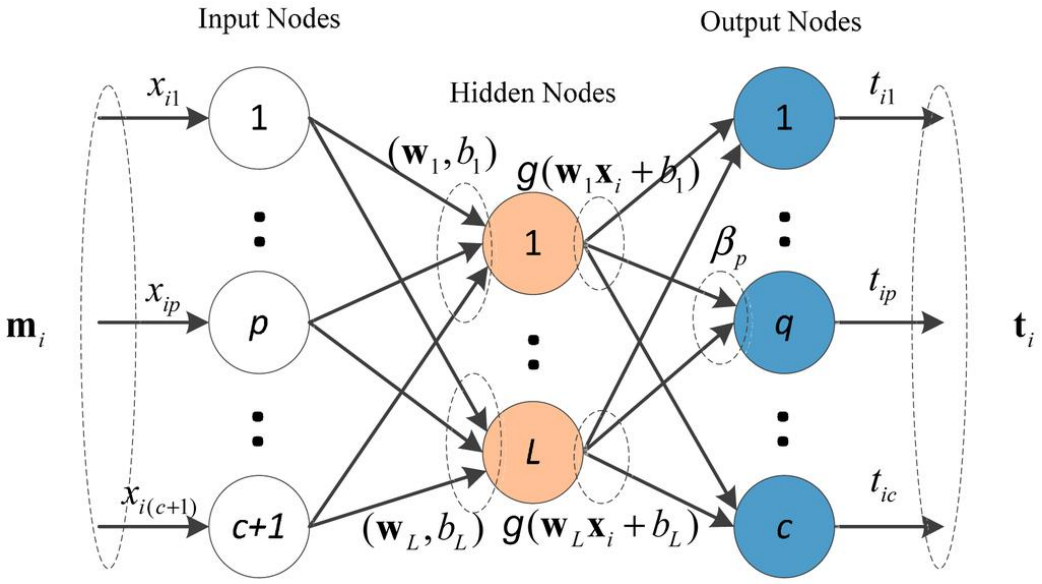

Figure 2-12 Decision making network of ELM.

The output weight $\hat{\beta}$ is then used to determine the output for the samples in the testing set. This output is compared to their known target output to calculate the corresponding classification accuracy.

2.4.2.3 ELM Applications in Biomedical Diagnostics

There have been many successful use of ELM algorithms in biomedical diagnostics and

many encouraging results have been obtained. For example, a kernel based extreme learning machine classifier (KELM) was used to improve the diagnostic accuracy of Parkinson's disease (PD) with a sensitivity of 100% and specificity of 99.39%. Results obtained significantly outperform those achieved in SVM method and other methods in the literature [75]. ELM was also utilized for diabetes diagnosis problem, ELM achieved a testing rate that is higher than results derived from many other popular algorithms such as bagging and boosting method, C4.5 and BP algorithm. In addition, the running time of ELM is significantly shorter which is 1000 times less than BP and 12 times less than SVM [67].

Chapter 3. QUANTITATIVE DIAGNOSIS OF CERVICAL NEOPLASIA USING FLUORESCENCE LIFETIME IMAGING ON HAEMATOXYLIN AND EOSIN STAINED TISSUE SECTIONS

3.1 Motivation

The use of conventional fluorescence microscopy for characterizing tissue pathological states is limited by overlapping spectra and the dependence on excitation power and fluorophore concentration. Fluorescence lifetime imaging microscopy (FLIM) can overcome these limitations due to its insensitivity to fluorophore concentration, excitation power and spectral similarity. This study investigates the diagnosis of early cervical cancer using FLIM and a neural network extreme learning machine classifier with the aim to develop an alternative method to supplement the traditional histopathological examination of early cervical cancer.

3.2 Introduction

3.2.1 Current Screening Methods for Cervical Cancer

Worldwide, cervical cancer is the second most common cancer among women which accounts for about 12% of all female cancers and causes approximately 250,000 deaths annually [1]. Fortunately, the carcinoma of the cervix is preceded by a long precancerous stage of 10 to 15 years, making early detection and treatment possible. A variety of

cervical screening methods has consequently been developed to detect the pre-malignant cervical changes.

The routine way for early cervical screening is the Papanicolaou (Pap) smear and diagnostic information is acquired from the exfoliated cells that were scraped from the cervix wall and morphologically evaluated under a microscope. However, because Pap smear shows a low averaged sensitivity of not more than 58% and a specificity of 69% [2], multiple periodic Pap tests are conducted to reduce the false-negatives. To overcome the low sensitivity, the detection of an abnormal Pap smear is followed by an in site colposcopic investigation where a mounted magnifying lens is used to inspect the cervix after rinsing with 3%-6% acetic acid to confirm the abnormality. Although colposcopy in expert hands exhibits excellent sensitivity (>90%), the specificity remains low (<50%), which eventually requires a directed biopsy for definitive diagnosis [5]. The colposcopy-directed biopsy is fixed in formalin, dehydrated, mounted onto wax blocks, sectioned and stained with haematoxylin and eosin (H&E) before a histopathologist evaluates these H&E stained tissue sections under a white light microscope. This is regarded as the gold standard for cervical cancer diagnosis in most hospitals [3, 4].

The two distinct dyes, haematoxylin and eosin, stain the cell nuclei blue-purple and the intracellular and extracellular protein pink, respectively. Morphological changes, such as nuclear shape, size of epithelial cells, cell density and epithelial thickness are the key indicators used by histopathologists to make a diagnosis [76, 77]. However, great variability in the diagnostic results exists since the diagnostic process is a labor-intensive procedure and relies very much upon subjective interpretation [78]. In addition, implementation of this approach requires extensive infrastructure, personnel and

economic resources. Many women especially those from developing countries are suffering from not having sufficient exposures to these screening facilities [79]. Consequently, many complementary screening protocols to overcome these limitations and to aid the traditional gold standard histopathological diagnosis were proposed.

3.2.2 Supplementary Cervical Screening Methods

Digital colposcopy with automated computer-assisted image analysis technique has been developed to facilitate cervical cancer examinations especially in developing countries where low-resource settings and poor financial conditions are commonly present [80-82]. Diagnostic features including vascular features, acetowhitening and mosaicism features from the colposcopic images were extracted for classifications. However, only morphological features such as vascular size, shape, arrangement and intercapillary distances were studied.

Significant advancement in photonic technology has seen various optical techniques being used in the screening and diagnosis applications [13, 83, 84]. Quantitative analysis, rather than the conventional qualitative examination, has proven to provide objective and accurate diagnosis of neoplasia even in the hands of nonexpert operators [5]. Minimally invasive spectroscopic methods, including light scattering spectroscopy, reflectance spectroscopy and fluorescence spectroscopy, have been investigated to detect cervical neoplastic lesions to resolve the long-standing problems in the gold standard diagnosis [5, 6, 85]. These approaches have shown great potential to support the traditional histopathological examination because they could identify not only tissue morphology but also the biochemical changes occurring in abnormal tissues.

Fluorescence spectroscopy is one of the most popular methods in biomedical research that offers high signal-to-noise ratio and it has been used to discriminate between histologically abnormal and normal cervical tissues with high sensitivity and specificity [10, 11, 85-87]. Endogenous fluorophores [10] and exogenous photo-sensitizers such as the haemato-porphyrin derivatives and 5-aminolevulinic acid [11] were studied for tissue diagnosis. However, the dependence on the excitation power and fluorophore concentration (due to staining artefacts) of the fluorescence emission restricts its application as a more widely used standard protocol.

3.2.3 Imaging the Cervix with Fluorescence Lifetime Imaging (FLIM)

Fluorescence lifetime imaging (FLIM) technique measures the decay time of a fluorescence emission from which micro-environmental parameters of the fluorophores, such as viscosity, pH and oxygen concentration, can be determined and potentially be correlated to tissue pathology [9]. Compared to conventional fluorescence spectroscopy which is based on spectral features and intensity, fluorescence lifetime is independent of the excitation power and fluorophore concentration [88].

The fluorescence lifetime has been investigated in many previous studies to evaluate its diagnostic feasibility [89-92]. Basal cell carcinomas (BCCs) were distinguished from uninvolved skin ex vivo through fluorescence lifetimes from autofluorescence generated from unstained excision biopsies [89]. Fixed and unstained breast cancer tissues were also examined with fluorescence lifetime imaging and a correlation to histopathological assessment was demonstrated [90]. In addition, autofluorescence in the fundus was measured for the early diagnosis of age-related macular degeneration [91]. Most of these

studies used unstained tissues and the detectable laser-induced autofluorescence was typically very weak due to the low intrinsic fluorophore concentration and the low excitation power limited by the maximum permissible exposure [93]. The diagnostic capability of FLIM can be greatly limited by biased lifetime values arising from the low fluorescence emission [94]. Several new approaches to lifetime analysis [95-97] were recently reported to alleviate this problem. Some studies have previously utilized the fluorescence intensity of H&E stained tissues for diagnosis [98-101], but the corresponding changes in the fluorescence lifetime of the staining compounds has not been investigated. Since eosin stains the intracellular proteins in the cytoplasm of cells, changes in the eosin fluorescence lifetime can potentially provide additional diagnostic information for disease detection.

In this work, the diagnostic value of the fluorescence emission from H&E stained cervical tissue sections was investigated using the FLIM technique. Cervical cancer detection based on the fluorescence lifetime of H&E stained samples were carried out using a quantitative analysis method to support the traditional histopathological diagnosis. More than 100 H&E stained cervical tissue sections classified into categories of normal, cervical intraepithelial neoplasia (CIN1, CIN2, CIN3), squamous cell carcinoma (SCC) and microinvasive were collected for imaging and analysis. Epithelial regions of these cervical tissue sections were imaged with a FLIM system and a neural network extreme learning machine (ELM) classifier [66] based on a feedforward neural network [102] was used for discrimination. The neural network ELM classifier was selected due to its ability to detect complex trends with good generalization performance at extremely fast learning speed. It is noteworthy that nearly 70% of CIN1 will revert to normal within one year, while 90% of CIN2 and CIN3 could progress to life-threatening

condition within two years if left untreated [103]. Thus, patients diagnosed with CIN2 and CIN3 are high-risk groups requiring immediate treatment. Consequently, the accuracy of the proposed technique in discriminating the high-risk group (CIN2, CIN3) from the low-risk group (Normal, CIN1) was evaluated. The results showed that the proposed fluorescence lifetime imaging technique with the quantitative neural network ELM discrimination method of H&E stained cervical tissue sections can achieve a high accuracy and can be used to aid and complement the traditional histopathological examinations.

3.3 Materials and Methods

3.3.1 Sample Set

A total of 117 H&E stained cervical tissue sections from 103 patients were collected from the KK Women's and Children's Hospital (KKH), Singapore in this study. The histopathological examination of the H&E stained cervical sections was performed by a senior pathologist from KKH and the corresponding region-of-interests (ROIs) in the epithelium were identified as normal, CIN1, CIN2, CIN3, SCC and microinvasive. The whole sample set comprises 27 normal, 23 CIN1, 23 CIN2, 21 CIN3, 11 SCC and 12 microinvasive cervical tissue sections. This study was reviewed and approved by the KKH ethics committee and Institutional Review Board (CIRB 2010/745/C).

3.3.2 Instrumentation and Image Acquisition

A time-resolved fluorescence measurement system incorporating a confocal laser scanning microscope (LSM 510, Carl Zeiss, Germany) and a time-correlated single

photon counting (TCSPC) system (SPC830, Becker & Hickl, GmbH) was used to image the H&E stained cervical tissue sections. The schematic configuration of the FLIM system is shown in Figure 3-1.

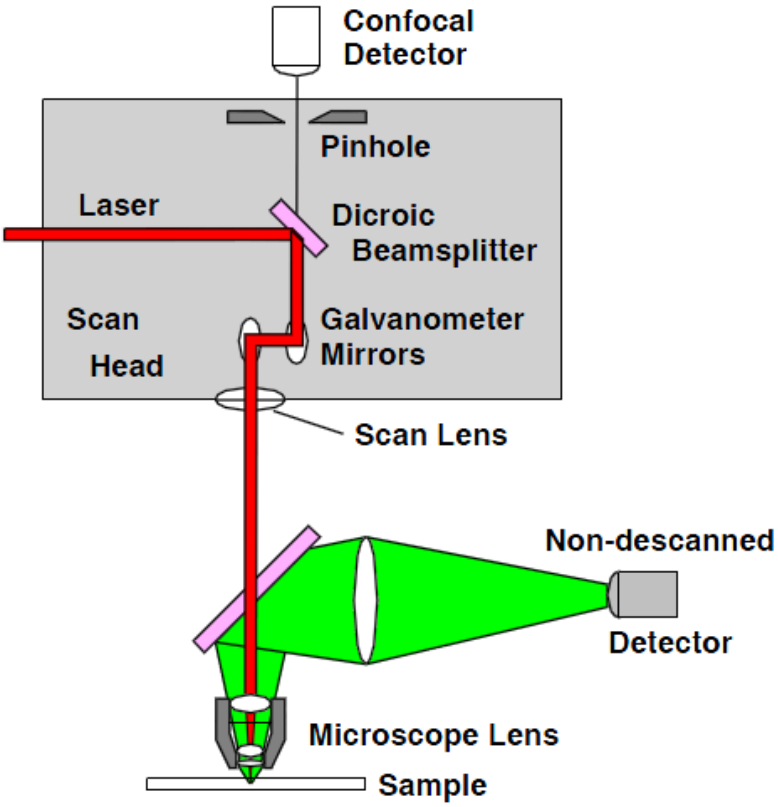

Figure 3-1 Schematic configuration of the FLIM system [104] used in this work.

The confocal microscope is equipped with mode-locked Titanium (Ti): Sapphire laser (Coherent Mira 900, 76 MHz, 200 fs) pumped by an 8 W solid state laser (Coherent, Verdi). Although simple and cheap pulsed single photon excitation source such as laser diodes (LD) and light-emitting diodes (LEDs) are often used in TCSPC and lifetime measurement, however, the pulse width of these lasers are in the range of picosecond to nanosecond. While for our measured fluorescence lifetime of eosin, which binds with tissue proteins, is not clear when we initiated the lifetime measurement. Therefore, Ti-Sapphire laser with 200 fs pulse width was used to achieve best accuracy of lifetime

measurement we could because it is desirable to have the laser pulse width much shorter than the sample lifetime. The femtosecond Ti: Sapphire laser was tuned to a wavelength of 760 nm for two-photon excitation (TPE). An excitation power corresponding to 10% of the maximum laser power was used to minimize photodamage to the samples while obtaining sufficient fluorescence emission photons. The continuous train of pulses from the laser source was diverted by a dichroic beamsplitter to the galvanometer mirrors before focusing on the sample via a scan lens and an objective (20× Fluar, Carl Zeiss, NA = 0.75). The fluorescence emission was collected using the same objective lens. Another dichroic mirror (KP685, Carl Zeiss) was used to direct the fluorescence emission (400–680 nm) to a fiber bundle which was connected to a PMC-100 detector. The output signal from the detector was processed by the TCSPC module. Each lifetime image was obtained with a scanning time of 60 s with spatial size of 256×256 pixels. The spatial resolution is approximately 1.8 μm per pixel and the fluorescence decay was recorded within a time window of 10 ns and a temporal resolution of ~39 ps. Prior to fluorescence lifetime imaging, white-light microscopy was first performed to locate the identified ROIs. Confocal fluorescence imaging was then performed and objective-slide distance was adjusted in order to obtain the best focus. This optimum objective-slide distance was maintained when conducting the lifetime measurement to obtain the maximum emission photons.

3.3.3 Data Processing

3.3.3.1 Lifetime Calculation and Feature Vectors

The fluorescence lifetime τ is defined as the characteristic time that a fluorophore stays

in the excited state. The lifetime calculations were performed using the commercial SPCImage software (Becker & Hickl, Germany). To improve the signal-to-noise ratio of the measured fluorescence decay profile, an averaged nine-pixel decay profile was used for lifetime calculations. To accelerate the calculation, the threshold value was set to 50 photons so that dark pixels were not processed for curve fitting. The instrument response function (IRF) was estimated from the rising edge of the decay curve and a double exponential model was used for the curve fitting. The double exponential model of the fluorescence decay is of the form:

$$I(t) = a_1 \exp(-\frac{t}{\tau_1}) + a_2 \exp(-\frac{t}{\tau_2}) \tag{3-1}$$

where τ_1 and τ_2 are the fluorescence lifetimes, and a_1 and a_2 are the fractional contribution of each lifetime component. Figure 3-2 gives a generic plot for a double exponential decay curve measured from TCSPC instrument.

Lifetime values, τ_1 and τ_2, were calculated using an iterative nonlinear least-squares (NLLS) algorithm [105]. A false-colored lifetime image for every sample comprising of 256×256 pixels was generated by assigning a color to the lifetime value of τ_2 at each pixel. For each lifetime image, a mask in the epithelium corresponding to the identified ROIs by our pathologist was manually drawn by visual inspection and the extracted lifetime values from the pixels in the mask were exported.

Feature vectors comprising the mean, μ, and standard deviation, σ, of the extracted lifetime components in the ROI were calculated and used for classification.

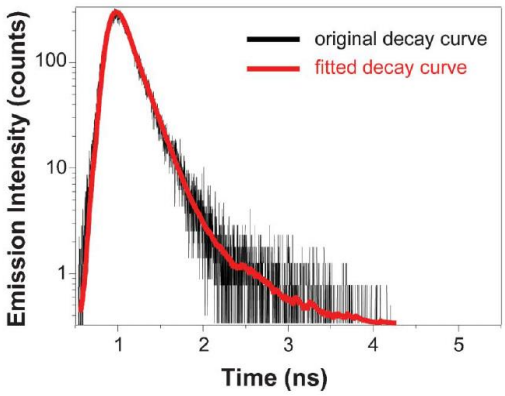

Figure 3-2 Measured fluorescence decay curve of PFBS30 Pdots (black line) and the fitted double exponential decay function (red line) [106]

3.3.3.2 Classification with Extreme Learning Machine (ELM)

Discrimination of normal vs. precancerous (CIN1, CIN2, CIN3), high-risk (CIN2, CIN3) vs. low-risk (normal, CIN1) and normal vs. abnormal (CIN1, CIN2, CIN3, SCC, microinvasive) samples were made using the neural network ELM classifier. Compared with other conventional computational intelligence classifiers based on neural networks, such as the support vector machines (SVMs) and back-propagation (BP) methods [107], the use of the ELM learning algorithm for a neural network provides a better generalization performance and a much faster learning speed because parameters in the network do not need to be iteratively tuned and all weights in the hidden nodes are randomly generated [108].

In this work, a single-hidden layer feedforward neural network with 20 hidden nodes is used. The ELM learning algorithm can be briefly described as follows [66]. Consider a training set $\Psi = \{(\boldsymbol{x}_i, \boldsymbol{t}_i) \mid \boldsymbol{x}_i = [x_{i1}, x_{i2}, \ldots, x_{in}]^T \in R^n, \boldsymbol{t}_i = [t_{i1}, t_{i2}, \ldots, t_{im}] \in R^m, i = 1, \ldots, N\}$ where $\boldsymbol{x}_i$ and $\boldsymbol{t}_i$ specify the input lifetime feature vector of a ROI and the associated output

target describing the pathological state, and N refers to the number of samples in the training set while i specifies the sample index. The hidden layer output matrix $\mathbf{H}$ and the output weight $\boldsymbol{\beta}$ of the neural network are calculated using the following steps:

1) Randomly assign input weight vectors $\mathbf{a}_i$ and hidden node bias b_i, $i = 1,\ldots, L$ where L is the number of hidden nodes. An L value of 20 was found to give maximum accuracy in this study.
2) Calculate the output function of each hidden node $g(\mathbf{a}_i, b_i, \boldsymbol{x})$, $i = 1, \ldots, N$ and the hidden layer output matrix $\mathbf{H} = [g(\mathbf{a}_1, b_1, \boldsymbol{x}), \ldots, g(\mathbf{a}_L, b_L, \boldsymbol{x})]$. Here, $g(\mathbf{a}_i, b_i, \boldsymbol{x}) = 1/(1+\exp[-(\mathbf{a}_i \cdot \boldsymbol{x} + b_i)])$, $\mathbf{a}_i$ and b_i are in the range of [-1,1].
3) Determine the output weight, $\boldsymbol{\beta} = \mathbf{H}^{+}\mathbf{T}$ where $\mathbf{H}^{+}$ is the Moore-Penrose generalized inverse of the hidden layer output matrix $\mathbf{H}$ [66] and $\mathbf{H}$ satisfies the equation $\mathbf{H}\boldsymbol{\beta} = \boldsymbol{t}$, where $\boldsymbol{\beta} = [\beta_1, \ldots, \beta_L]^T$.

In this work, n specifies the number of attributes in the feature vector (μ and σ) of a ROI used for classification and therefore has a value of 2. On the other hand, m denotes the two possible pathological states of a sample, e.g. normal or precancerous, and therefore a value of $m = 2$ is used.

The output weight $\boldsymbol{\beta}$ of the neural network is firstly calculated based on the feature vectors and their known target output in the training data set. This output weight $\boldsymbol{\beta}$ can then be used to determine the output for the feature vectors in the testing set and compared to their known target output to quantify the diagnostic accuracy of the neural network ELM classifier. Cross-validation technique was applied to achieve unbiased selection of training data and testing data. Basically, it randomly splits the whole dataset

into training dataset and testing dataset. Training and testing data sets of equal sizes are used to maximize the accuracy of ELM algorithm in this case. Hence, to discriminate histologically identified normal vs. precancerous and high-risk vs. low-risk samples, feature vectors from 47 randomly selected samples were chosen as training data while feature vectors from the remaining 47 samples were used for testing. For the discrimination of normal vs. abnormal tissues, 59 randomly selected feature vectors were chosen as the training data while the remaining 58 feature vectors were used for testing. A total of 1000 random sets of training and testing data were generated for computation to reduce classification bias. For each set of randomly selected training data and testing data, ELM is applied for classification. The diagnostic accuracy (sensitivity and specificity) for each set of training data and testing data is then calculated by comparing the ELM result with the histological identification.

The sensitivity and specificity are the two most important statistical measures to evaluate a clinical diagnosis. The sensitivity refers to the ability to correctly identify those patients with the disease and specificity refers to the ability to correctly identify those patients without the disease [109]. The ideal target values for sensitivity and specificity desirable in any test is 100% and 100%, respectively.

$$Sensitivity = \frac{True\ Positives}{True\ Positives + False\ Negatives} \quad (3\text{-}2)$$

$$Specificity = \frac{True\ Negatives}{True\ Negatives + False\ Positives} \quad (3\text{-}3)$$

True positive refers the patient has the disease and was diagnosed as positive while *false positive* refers to the patient does not have the disease but was diagnosed as positive. *True negative* refers to the patient does not have the disease and was diagnosed as negative while *false negative* refers to the patient has the disease but was diagnosed as negative.

Finally, the mean sensitivity and specificity from the 1000 sets of data were computed accordingly for comparison. The ELM algorithm was implemented in Matlab with open access code from the internet and minor changes were made to adapt to the case in our study.

3.4 Results and Discussion

3.4.1 Measured Lifetimes of H&E Stained Cervical Tissue Sections

Figure 3-3 shows the fluorescence lifetime image of a typical H&E stained normal cervical tissue and its corresponding fluorescence intensity image. Compared to the intensity image, the lifetime image may provide additional contrast and more information can potentially be extracted to study the tissue pathology. It is also observed that the cell-rich epithelium region is quite distinct from the stroma region which is composed of fibroblasts, smooth muscle cells and collagen [110]. The stroma and epithelium are clearly separated by a visible boundary, which can clearly be seen in Figure 3-3. The cell-rich epithelium region was studied to assess the feasibility of the proposed quantitative fluorescence lifetime technique since most cervical cancers are considered to originate from the epithelium [111].

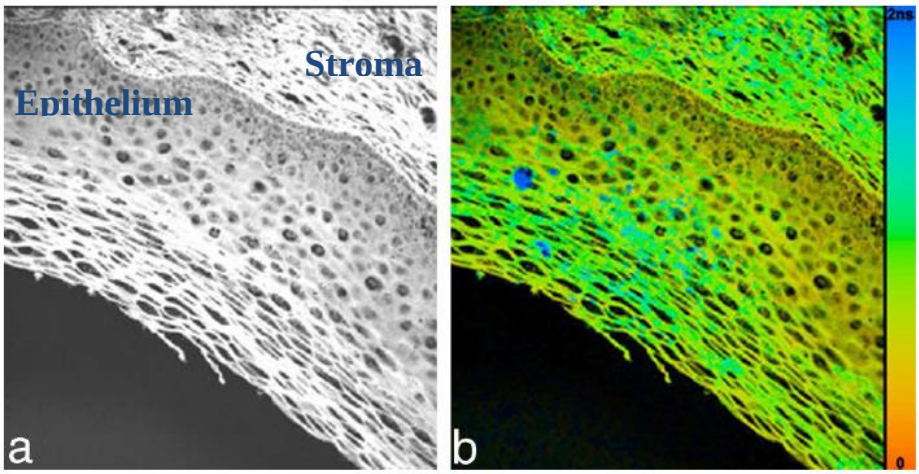

Figure 3-3 Fluorescence (a) intensity and (b) lifetime images of a typical H&E stained normal cervical tissue section. The region towards the upper right is the stroma while the region on the lower left is the cell-rich epithelium clearly separated by a visible boundary. The false color scale bar in (b) represents fluorescence lifetime on a scale of 0 (red) to 2 ns (blue).

It was found that feature vectors of the larger lifetime component τ_2 displayed significant difference while the smaller lifetime component τ_1 exhibited negligible distinction among different cervical disease stages. The smaller lifetime component τ_1 was found to have typical values of ~30 ps, which is within the response time of the measurement system. Therefore, τ_1 is attributed to the scattered excitation light reaching the detector during lifetime measurements.

To determine the origin of the larger lifetime component τ_2, the fluorescence spectra of unstained and H&E stained cervical tissue sections were measured. The fluorescence emission intensity from H&E stained tissue sections was found to be significantly higher than those obtained from unstained tissue sections. The fluorescence spectra of the eosin

solution was also measured and compared with that of H&E-stained tissue (result not shown). Their fluorescence emission spectra are essentially overlapping with an identical emission peak at ~554 nm, which is in good agreement with other reported findings [101]. It was therefore concluded that the larger lifetime component τ_2 is due to eosin. Since the lifetime component τ_1 did not exhibit any correlation to disease stages, only the mean and standard deviation of τ_2 values from ROIs in the epithelium were used for discriminations.

3.4.2 Normal vs. Precancerous and Low-Risk vs. High-Risk

Figure 3-4 shows the scatter plot of the feature vectors of the lifetime component τ_2 for all cervical tissue samples collected in this work. It can be seen that normal tissues generally have larger lifetimes ranging from 700 ps to 1300 ps while precancerous tissues have smaller lifetimes of 400 ps to 870 ps. The overlapping region (700 ps to 870 ps) is mostly attributed to the CIN1 samples. Although many feature vectors of CIN1 samples fall into this range, approximately half of them are located within the lifetime interval 750 ps~870 ps. It can also be seen that most feature vectors from normal tissues have larger mean lifetime values and are located in the lower right region of Figure 3-4. By contrast, precancerous tissues exhibit smaller lifetime values and the feature vectors are clustered in the upper left region of the figure.

The discrimination results for normal vs. precancerous and low-risk group vs. high-risk group are shown in *Table 3-1*. The neural network ELM classifier is found to give a concurrently high sensitivity of 92.8% and specificity of 80.2% when discriminating between normal and precancerous cervical tissues (Figure 3-5a). A sensitivity and

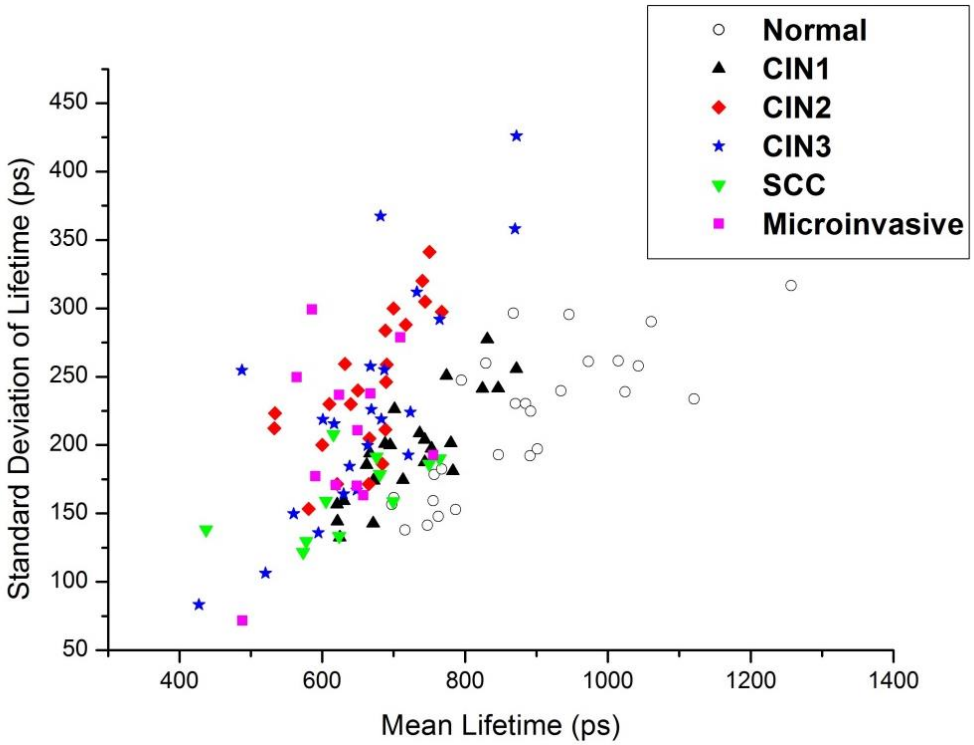

Figure 3-4 Scatter plot of feature vectors from epithelium lifetimes of histologically normal (open symbol) and abnormal (filled symbols) cervical tissues including CIN1 (up triangle), CIN2 (diamond), CIN3 (star), SCC (down triangle), Microinvasive (square). The horizontal axis represents the mean lifetime, μ, while the vertical axis represents the standard deviation, σ, of τ_2.

specificity of 85.0% and 87.6%, respectively, are achieved when differentiating low-risk vs. high-risk cervical tissues (Figure 3-5b).

3.4.3 Normal vs. Abnormal

In cancerous cervical tissues (SCC and microinvasive), the abnormal cells have penetrated through the basement membrane that separates the epithelium and the stroma. Consequently, cancerous cervical tissues could be morphologically distinguished from normal and precancerous cervical tissues.

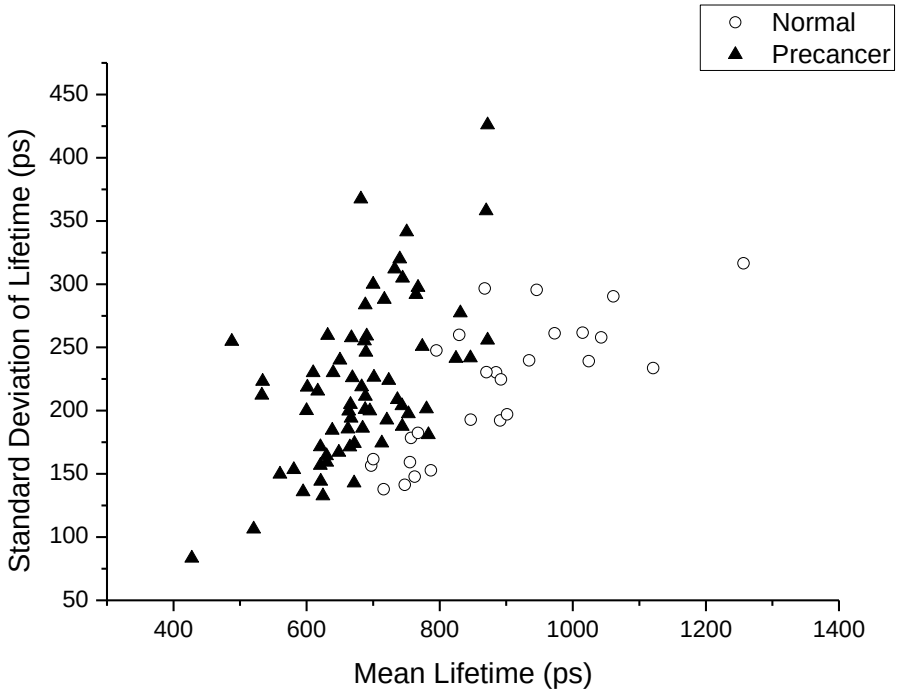

(a)

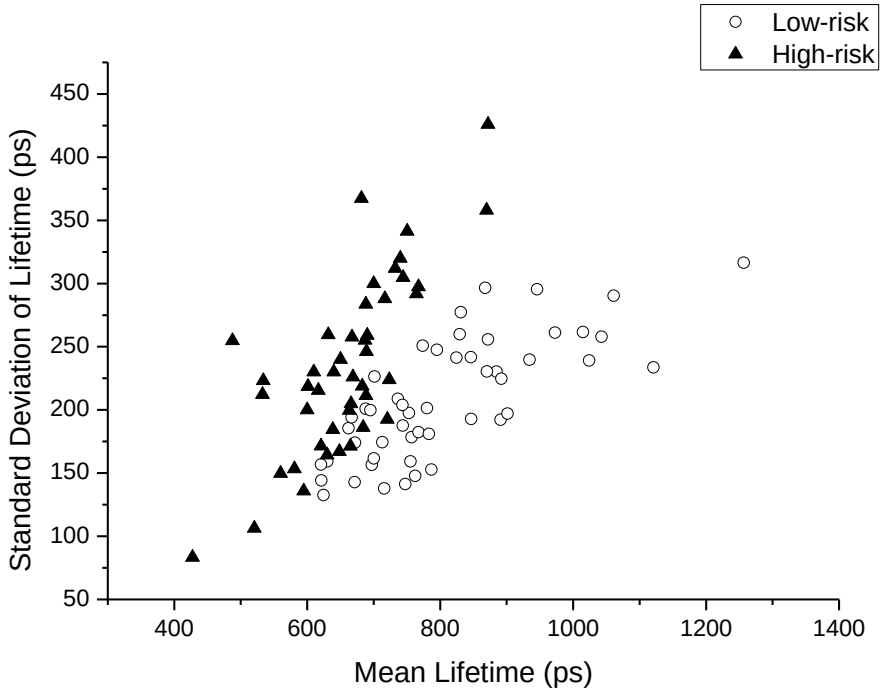

(b)

Figure 3-5 Scatter plot of feature vectors from epithelium lifetimes of (a) Histologically (a) normal (open circle) vs. precancerous cervical tissue (filled triangle) and, (b) low-risk group (open circle) vs. high-risk group (filled triangle). The horizontal axis represents the mean lifetime, μ, while the vertical axis represents the standard deviation, σ, of τ_2.

Table 3-1 Averaged sensitivity and specificity of discriminating normal vs. precancerous and low-risk vs. high-risk samples. The results were computed from 1000 randomly chosen training and testing data sets using the neural network ELM classifier.

Tissue Type	Normal vs. Precancerous	Low-Risk vs. High-Risk
Sensitivity	92.8%	85.0%
Specificity	80.2%	87.6%

Nevertheless, the fluorescence lifetimes of cancerous cervical tissues were also investigated and comparisons with normal and precancerous tissues were made for completeness. From Figure 3-4, it can be seen that the higher grade of dysplastic tissues including CIN2, CIN3, SCC and microinvasive have lifetimes values of 400 ps to 870 ps. However, feature vectors of cancerous tissues are mixed with those from precancerous tissues and they can hardly be distinguished from each other. Feature vectors of these abnormal tissues (cancerous and precancerous) are located in the left region while those of normal tissues occupied the right region of the plot. Consequently, only classifications of normal vs. abnormal tissues were performed and the results are illustrated in Table 3-2. It was found that the neural network ELM classifier achieved a concurrently high sensitivity and specificity of 88.3% and 89.2%, respectively.

3.4.4 Comparison with other Screening Methods

It is obvious from the above results that the proposed fluorescence lifetime imaging technique using the neural network ELM classifier can achieve good discriminations

Table 3-2 Averaged sensitivity and specificity of discriminating normal vs. abnormal samples. The results were computed from 1000 randomly chosen training and testing data sets using the neural network ELM classifier.

Tissue Type	Normal vs. Abnormal
Sensitivity	88.3%
Specificity	89.2%

among the different cervical disease stages. Table 3-3 compares the sensitivity and specificity of diagnosing normal vs. precancerous cervical tissues using the proposed lifetime technique as well as the other complementary diagnostic techniques reported in the literature. As compared to the scattering spectroscopy, lifetime technique can achieve a significantly higher sensitivity and specificity. Although the specificity of 81.1% for reflectance spectroscopy is comparable to that of lifetime technique (80.2%), its sensitivity of 72.0% is much lower than lifetime method (92.8%).

Table 3-3 Sensitivity and specificity of different supplementary screening methods in differentiating normal and precancerous cervical tissues.

Screening Method	Sensitivity	Specificity
Scattering Spectroscopy[9]	70.4%	66.7%
Reflectance Spectroscopy[3]	72.0%	81.1%
Lifetime method	92.8%	80.2%

3.4.5 Discussion

The study reveals that as the disease stage of cervical tissues progress from normal to precancerous to cancerous, the lifetime component τ_2 decreases in value. It is the change in this lifetime value that allows a discrimination decision to be made. The lifetime component τ_2 was attributed to fluorescence emission of eosin in the H&E stained sections. The value of τ_2 for all samples measured was found to range between 0.4 ns and 1.3 ns. By contrast, the fluorescence lifetime range of eosin in different solutions were reported to be between 1.4 ns to 3.7 ns [112], which is significantly larger than that measured in this work. The observed lifetime shortening can possibly be attributed to the binding of eosin molecules to tissue structures [83]. Since eosin stains the intracellular proteins in the cytoplasm of the cervical cells, the changes in the associated fluorescence lifetime as the cells progress from normal to abnormal appears to be related to the biochemical changes in the cytoplasm. Further investigation is conducted and demonstrated in chapter 6 to quantify the biochemical changes and the associated eosin lifetime changes as cervical cells become abnormal. Understanding the underlying mechanism to the biochemical changes in the cytoplasm may better aid the diagnosis and treatment of cervical cancer.

Discriminations between low-risk (Normal, CIN1) and high-risk (CIN2, CIN3) cervical samples are also conducted in this work due to its significant impact in clinical practice. In patient treatment management, this two-tier grading system has much more practical value as compared to the traditional normal and precancerous (CIN1, CIN2, CIN3) classification [48]. Although cancerous and CIN samples are not distinguishable by lifetime, they are easily distinguished from the normal and precancerous cervical tissues in morphology. In cancerous tissues, abnormal cells have penetrated beyond the

basement membrane into the underneath soft tissue and start to spread to other parts of the body [113].

3.5 Summary

A quantitative method based on the FLIM technique to aid the traditional gold standard histopathological diagnosis of cervical neoplasia was investigated. H&E stained cervical tissue sections were measured with a time-resolved two-photon excitation laser scanning fluorescence microscope and the corresponding lifetimes from the epithelium regions were extracted. Feature vectors comprising the mean and standard deviation of the eosin lifetime were used for discrimination with a neural network ELM classifier. Averaged sensitivity and specificity of 92.8% and 80.2%, respectively, were obtained when differentiating normal from precancerous (CIN1, CIN2, CIN3) tissues while a sensitivity and specificity of 85.0% and 87.6%, respectively, were achieved when distinguishing between low-risk (normal, CIN1) and high-risk (CIN2, CIN3) cervical tissues. A shortened lifetime was also observed for cancerous cervical tissues.

Comparison with other screening methods such as scattering spectroscopy and reflectance spectroscopy demonstrates that the proposed lifetime technique has the advantage of achieving a concurrently higher sensitivity and specificity. Therefore, the proposed method can provide an accurate and objective cervical diagnosis and can potentially supplement the traditional gold standard histopahtological examinations. Furthermore, the fast learning speed of ELM makes the classifier a potentially more efficient tool when optimizing the neutral network with a huge training data set containing multiple-component feature vectors in future applications.

Chapter 4. EPITHELIUM LAYER ANALYSIS OF FLUORESCENCE LIFETIME IMAGE FOR THE ENHANCEMENT OF EARLY CERVICAL CANCER DIAGNOSIS

4.1 Motivation

This work investigates the use of layer analysis method to study the fluorescence lifetime images of H&E stained cervical tissue sections. In the previous chapter, the mean and standard deviation of lifetimes in the region of interest (ROI) of cervical epithelium were shown to provide diagnostic information that can supplement the traditional histopathological examination of early cervical cancer. In this work, the previously defined ROI was evenly divided into layers and mean lifetimes in the top half epithelium were used as feature vectors for discriminations. It was found that the proposed layer analysis technique could enhance the diagnostic accuracy and shorten the calculation time.

4.2 Introduction

In Chapter 3, FLIM was used to image H&E stained cervical tissues sections and demonstrated its capability to supplement the traditional histopathological examination of early cervical cancer. Since the gold standard diagnosis of cervical precancer (CIN) is based on the proportion of epithelium affected by neoplasia, this suggests that diagnostic information might exist in the layered structures of cervical tissue sections.

In this work, the diagnostic value in the layered structures of H&E stained cervical tissue sections was investigated with FLIM. H&E stained cervical tissue sections classified into categories of normal and cervical intraepithelial neoplasia (CIN1, CIN2, CIN3) were used for fluorescence lifetime imaging and analysis. Lifetime values were first analyzed on a 3-layer model following the standard cervical intraepithelial neoplasia (CIN) diagnosis. Subsequently, epithelial regions of these cervical tissue sections were divided into 10 equal layers and analyzed. The 10-layer model is based on the finding that epithelium is generally composed of approximately 10 layers [42]. The basal layer, which adheres to the basement membrane, is one cell thick. Above this layer are the parabasal cells, which are two to three cells in thickness. These parabasal cells mature and form the upper intermediate and superficial layer. Feature vectors comprising lifetimes from different layers of the epithelial tissues were fed into the neural network extreme learning machine (ELM) classifier [66, 102] depicted in the last chapter for discriminations between normal and CIN.

It was shown in this work that there exist an optimal number of cervical epithelial layers to consider in the analysis, at which the diagnostic accuracy is maximized. Interestingly, the top half epithelium is identified as the effective zone for FLIM diagnosis with concurrently high sensitivity and specificity. The obtained averaged accuracy is about 1.5 times better than those in whole-epithelium and 3-layer epithelium models.

4.3 Materials and Methods

4.3.1 Sample and Measurement

Out of the 94 samples used in Chapter 3, 32 H&E stained cervical tissue sections were

selected and used for the analysis carried out in this chapter. Each chosen section has clear stratified layers that facilitate layer analysis to be made for this study. These tissue sections were pathologically examined by a senior consultant from the KKH and the identified regions in the epithelium were classified as normal, CIN1, CIN2 and CIN3. The sample set includes 10 normal, 8 CIN1, 6 CIN2 and 8 CIN3 cervical tissue sections. All the samples involved have regular layered structure since diagnostic information among these tissue layers is of interest in this study.

The FLIM measurement system used is the same as the one described in the previous chapter [114]. A time-resolved fluorescence measurement system incorporating a confocal laser-scanning microscope and a time-correlated single photon counting (TCSPC) system was used to image the H&E stained cervical tissue sections. Each image was captured with a spatial resolution of 256×256 pixels.

4.3.2 Cervical Epithelial Layer Definition and Feature Vectors

Epithelium regions in cervical lifetime images were divided into layers to analyze the characteristics of the lifetime component τ_2 along the epithelial growth direction. Cells in the epithelium grow and differentiate progressively in the direction towards the epithelial surface. The basement membrane, a thin and noncellular region between the epithelium and the neighboring stroma, forms a barrier to downward epithelial growth and is only breached if epithelium undergoes malignant transformation [115]. The structural difference in epithelium and stroma makes them clearly distinguished in white-light and fluorescence lifetime images as shown in Figure 4-1. The basement membrane is marked by a white dashed line L while the epithelial surface is outlined

with another white dashed line M (Figure 4-1b). Epithelial thickness is defined as the distance from a point on the epithelial surface to the basement membrane along the direction normal to the basement membrane. The epithelium is divided into 3 and 10 equal thickness layers, respectively along the direction of tissue growth [42] for lifetime analysis. The ROI in the epithelium for lifetime analysis is defined with equal width of each divided layer. Figure 4-1c shows a typical cervical tissue section epithelium divided into 10 layers. Layer 1 refers to the basal layer while layer 10 indicates the superficial layer. The 3-layer model analysis is of great interest for diagnostic comparison due to the classic definition of CIN, which is based on the thickness of epithelium covered by neoplastic cells. On the other hand, the 10-layer model is used to approximate the biological structure of a cervical epithelium, with its cellular maturity increasing towards the epithelial surface. Thus, the 10-layer analysis model has the advantage of evaluating the CIN cells as a function of their maturity level. Finally, the mean (μ) and standard deviation (σ) of lifetime in each divided layer is calculated for tissue classification.

4.3.3 Parameters in Extreme Learning Machine Classifier

Discriminations between normal and precancerous (CIN1, CIN2, CIN3) cervical tissues were performed using the neural network ELM classifier described in the previous chapter. In this work, the number of hidden node L was adjusted so that maximum discrimination accuracy is achieved in this study. The total number of feature components in each sample was specified by n. In the 3-layer analysis, μ and σ from layer 1 to layer 3 constitute a total of 6 feature components and thus n=6.

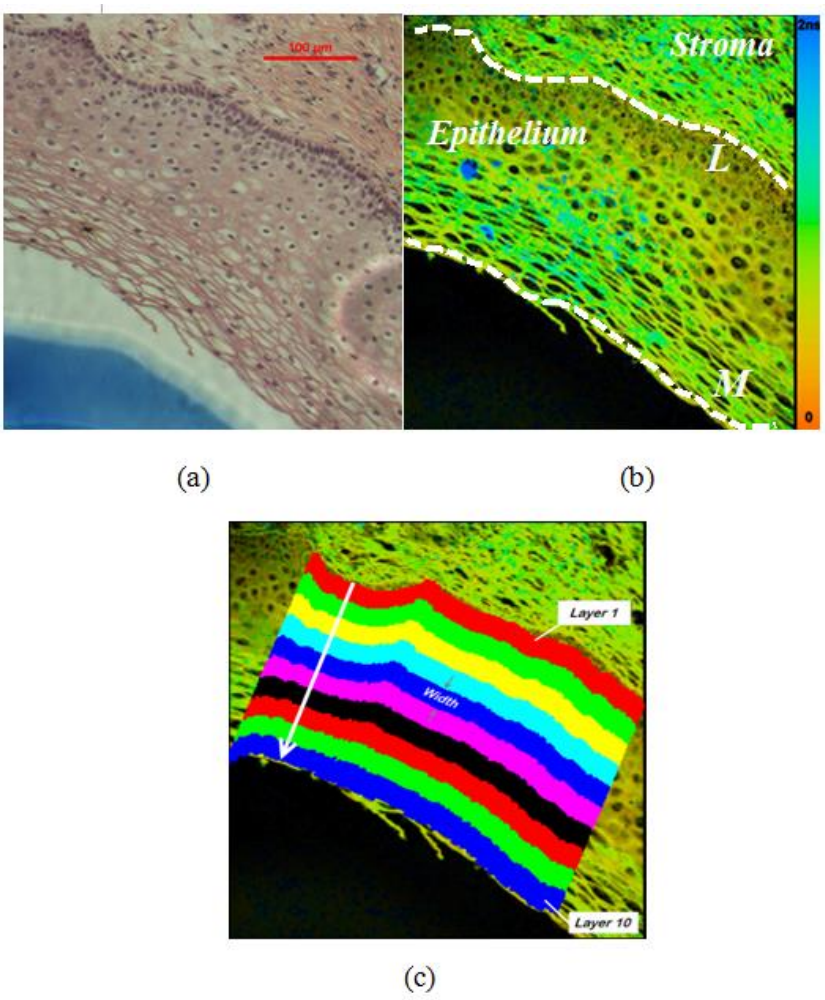

Figure 4-1 Division of a typical H&E stained cervical tissue section epithelium into 10 layers and the corresponding ROI defined in the fluorescence lifetime image. (a) White light image of the H&E stained tissue section (b) False color fluorescence lifetime image with scale bar from 0 to 2 ns. Basement membrane is marked out by white dashed line L and the epithelium surface is delineated by white dashed line M. (c) Pixels in each divided layer were obtained by moving basement membrane pixels in the direction perpendicular to the basement membrane towards the epithelial surface. Layers are numbered incrementally from 1 to 10. Pixels in each divided layer constitute the ROI.

The parameter *m* indicates the two possible pathological states of the cervical tissue sample, i.e. normal or precancerous, and takes a value of 2. In ELM, the output weight β of the neural network is first calculated based on the input feature vectors and their known target output from the training data set. This output weight β was then used to determine the output of the feature vectors in the testing data set and compared to their known target output to derive the diagnostic accuracy. The corresponding accuracy was evaluated in terms of sensitivity and specificity. To discriminate between histologically identified normal and precancerous samples, cross-validation was applied. Feature vectors from 16 randomly selected samples were chosen as training data while feature vectors from the remaining 16 samples were used for testing. A total of 1000 random sets of training and testing data were generated for computation. The resulting sensitivity and specificity for each set of training and testing data were calculated using the neural network ELM classifier. Finally, the mean sensitivity and specificity were computed accordingly for comparison. Distinctions between low-risk (Normal, CIN1) and high-risk (CIN2, CIN3) cervical samples were also conducted using the above described parameters.

4.4 Results and Discussion

4.4.1 Lifetime Distribution in Whole Cervical Epithelium

Figure 4-1a shows the white-light microscopic image of a typical H&E stained normal cervical tissue and Figure 4-1b shows the corresponding fluorescence lifetime image. The cell-rich epithelium region was specifically investigated and diagnosed with FLIM since cervical cancers mostly originate from the epithelium [111]. The diagnostic value of mean (μ) and standard deviation (σ) of τ_2 distribution in the whole epithelium is first

explored for comparison with layer analysis. Normal samples were found to have larger lifetimes in the range from 670 ps to 1000 ps while precancerous tissues have smaller lifetimes distributed from 450 ps to 850 ps. On the other hand, normal samples have lifetime σ values distributed between 150 ps and 200 ps while precancerous samples have lifetime σ values in the range of 170 ps to 280 ps. This allows a discrimination to be made between normal and precancerous cervical samples based on our previous work [114]. The diagnostic accuracy of whole-epithelium analysis was assessed with the ELM classifier, giving an averaged sensitivity of 62.2% and specificity of 52.3%. The sensitivity and specificity obtained here (62.2%, 52.3%) is lower than the result achieved in the previous chapter (92.8%, 80.2%). This is attributed to differences in sample size between the two calculations [116].

4.4.2 Sample Size versus Diagnostic Accuracy

A sample size study was conducted to verify the reason for the differences in the resulting diagnostic accuracy. Diagnostic accuracy was calculated by varying the number of samples used for ELM classification. The feature vectors were based on the mean and standard deviation of lifetimes from the manually selected ROI in epithelium of cervical tissues. Sample size was varied from 32 to 94 and the corresponding sensitivity and specificity were calculated and shown in Table 4-1. It can be seen from the table that the sensitivity and specificity increases as the sample size increases and finally reaches 92.8% and 80.2% respectively, as derived in the previous chapter. When the sample size is 32, the sensitivity (58.4%) and specificity (56.5%) is comparable to (62.2%, 52.3%) obtained in this work when μ and σ is from the lifetimes derived from the divided layers.

4.4.3 Three-Layer Analysis of Cervical Epithelium Lifetime

Each cervical epithelium was divided into 3 layers and the associated τ distribution profiles were extracted and compared against the pathological stages for each layer (as shown in Figure 4-2). A consistent trend of τ_2 shortening can be observed as cervical tissue progresses from normal to CIN3, except for layer 1, where τ_2 only shortens when the disease stage progresses from CIN2 to CIN3. The lifetime difference between normal and CIN 3 samples was estimated to be 50 ps at layer 1, 80 ps at layer 2 and 100 ps at layer 3. Mean lifetime of τ_2 in each divided layers was used to form a 3-dimensional feature vectors for ELM classification. The ELM classification result shows moderate improvement in diagnostic accuracy with sensitivity of 81.1% and specificity of 39.6% as compared to the results of whole-epithelium analysis. Standard deviation of the τ_2 distribution was also investigated, but its varying trends (Figure *4-3*) did not contribute to any significant improvement in diagnosis and are therefore considered uncorrelated to tissue pathology. The results indicate that feature vectors comprising only the mean τ_2 is sufficient to achieve the same diagnostic accuracy.

Table 4-1 Sensitivity and specificity obtained by the selection of different size of samples from 94 samples. Sample size was increased from 32 to 94 and corresponding sensitivity and specificity was calculated using ELM classifier.

Sample Size	Sensitivity	Specificity
32	58.4%	56.5%
50	77.1%	77.1%
64	85.4%	76.4%
80	90.6%	76.3%
94	92.8%	80.2%

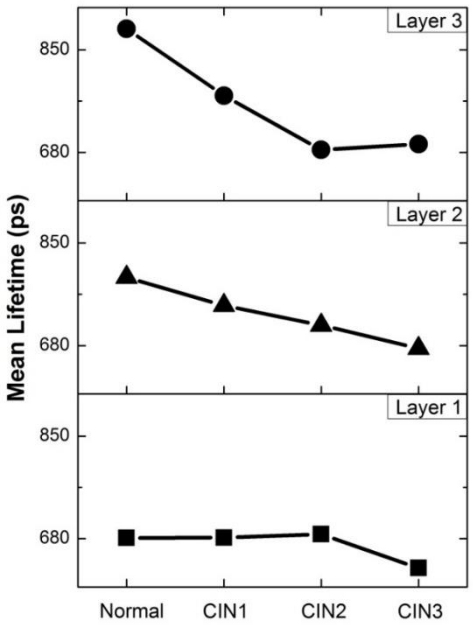

Figure 4-2 Distribution profiles of mean τ_2 in divided layer 1 (■), layer 2 (▲) and layer 3 (●) of epithelium against pathological states of Normal, CIN1, CIN2 and CIN3. Here, the mean τ_2 for each pathological state was calculated from the sample pool, which includes 10 normal, 8 CIN1, 6 CIN2 and 8 CIN3 cervical tissue sections.

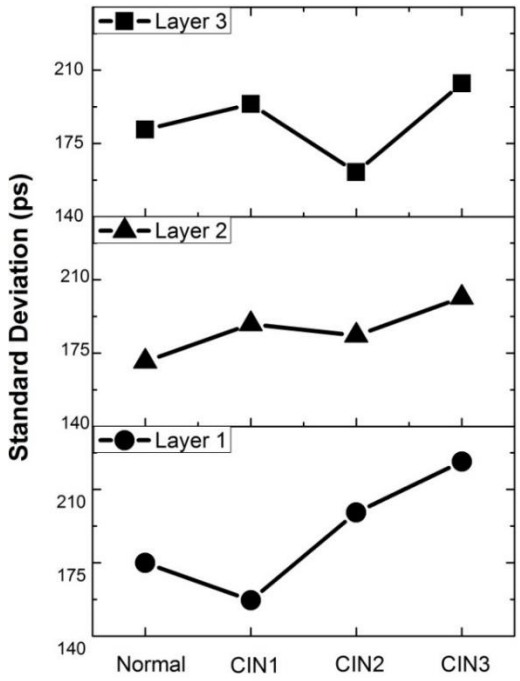

Figure 4-3 Distribution of τ_2 standard deviation σ in divided three layers among different pathological states of normal, CIN1, CIN2 and CIN3 tissues.

4.4.4 Ten-Layer Analysis of Cervical Epithelium Lifetime

The distribution of τ_2 in the 10 divided layers of each sample was analyzed for the various histological stages and presented in Figure 4-4 . Distributions of τ_2 in the first 5 layers (1-5) among normal and CIN samples were first compared.

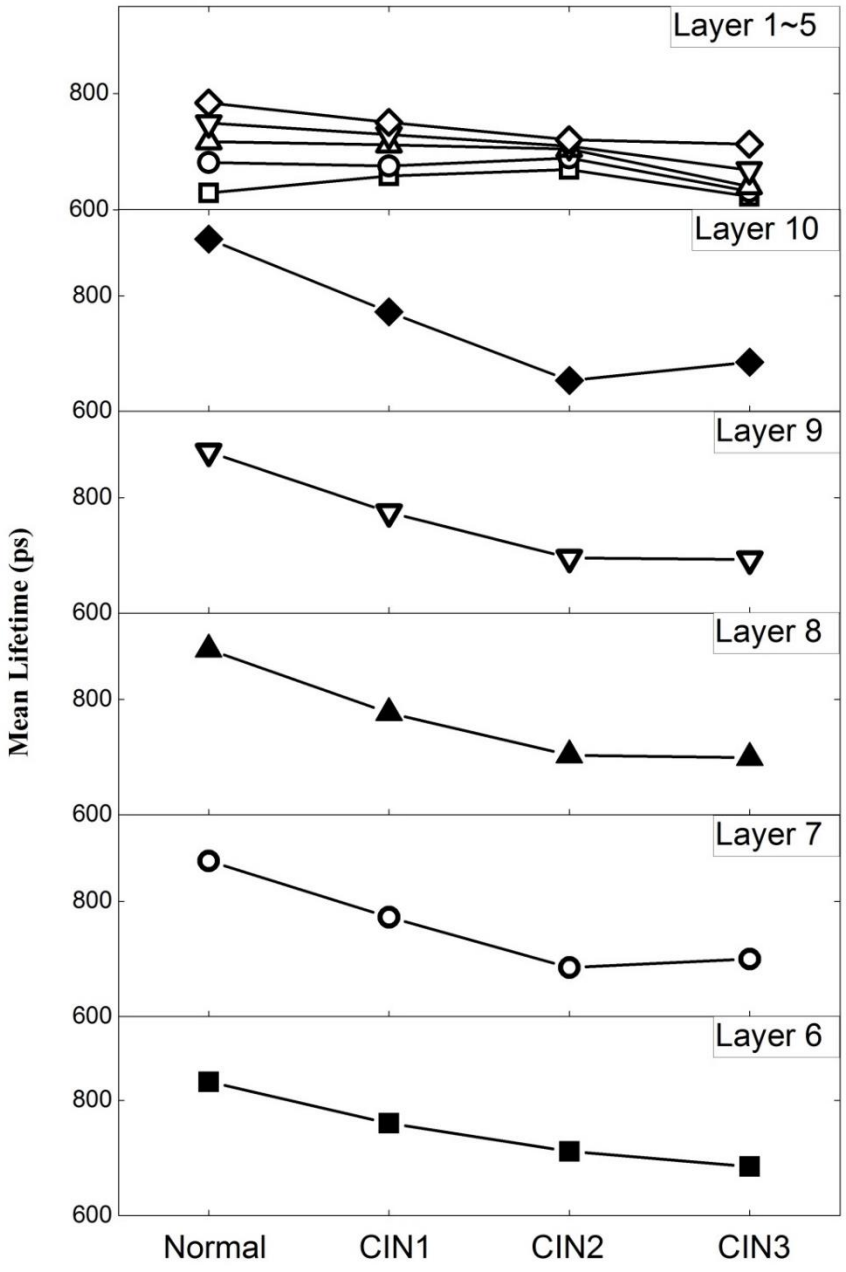

Figure 4-4 Distribution of mean lifetime τ2 in lower half layers (□-layer 1, ○-layer 2, △-layer 3, ▽-layer 4, ◇-layer 5) and top half layers (6-10) of epithelium as tissues progress from normal to various CIN grades.

Despite a consistent shortening of τ_2 in layers (3-5) as CIN progresses, the value of mean τ_2 change is below 70 ps when comparing normal epithelium with CIN 3 samples. By contrast, the mean τ_2 distribution from layer 6 to 10 shows greater variation across different pathological stages, with normal tissues exhibiting the longest lifetime. The mean τ_2 values in layer 6 to layer 10 were observed to consistently decrease as the tissues progress to the precancerous stages. When comparison is made from layer 6 to layer 10, the smallest lifetime variation of ~147ps is found at layer 6 while the largest change of ~245ps occurs in layer 10. Similar to the 3-layer epithelium analysis, the standard deviation σ of lifetime τ_2, with poor pathological correlation (Figure 4-5), was not included into the feature vectors for tissue classification.

The mean τ_2 values of normal and precancerous (CIN1, CIN2, CIN3) samples in each layer were also plotted in Figure 4-6 for comparison. Within each layer, certain amount of differences between normal and precancerous samples was observed, thereby providing differing degree of diagnostic information. It is desirable to have a suitable combination of mean τ_2 values to improve the classification performance [117].

To investigate the optimal number of layers to take into account for maximum accuracy, feature vectors comprising mean τ_2 values from successive layers, starting from layer 10, i.e. epithelial surface, to a lower layer (i.e layer 9) as the cut-off layer are studied. For instance, a typical set of feature vectors with cut-off at layer 9 is 2-dimensional containing mean τ_2 values from layer 10 and layer 9 while the cut-off layer is layer #6 results in a set of 5-dimensional feature vectors composed of mean τ_2 from layer 10 to layer 6. The ELM classifier was used to make classifications between normal and precancerous samples.

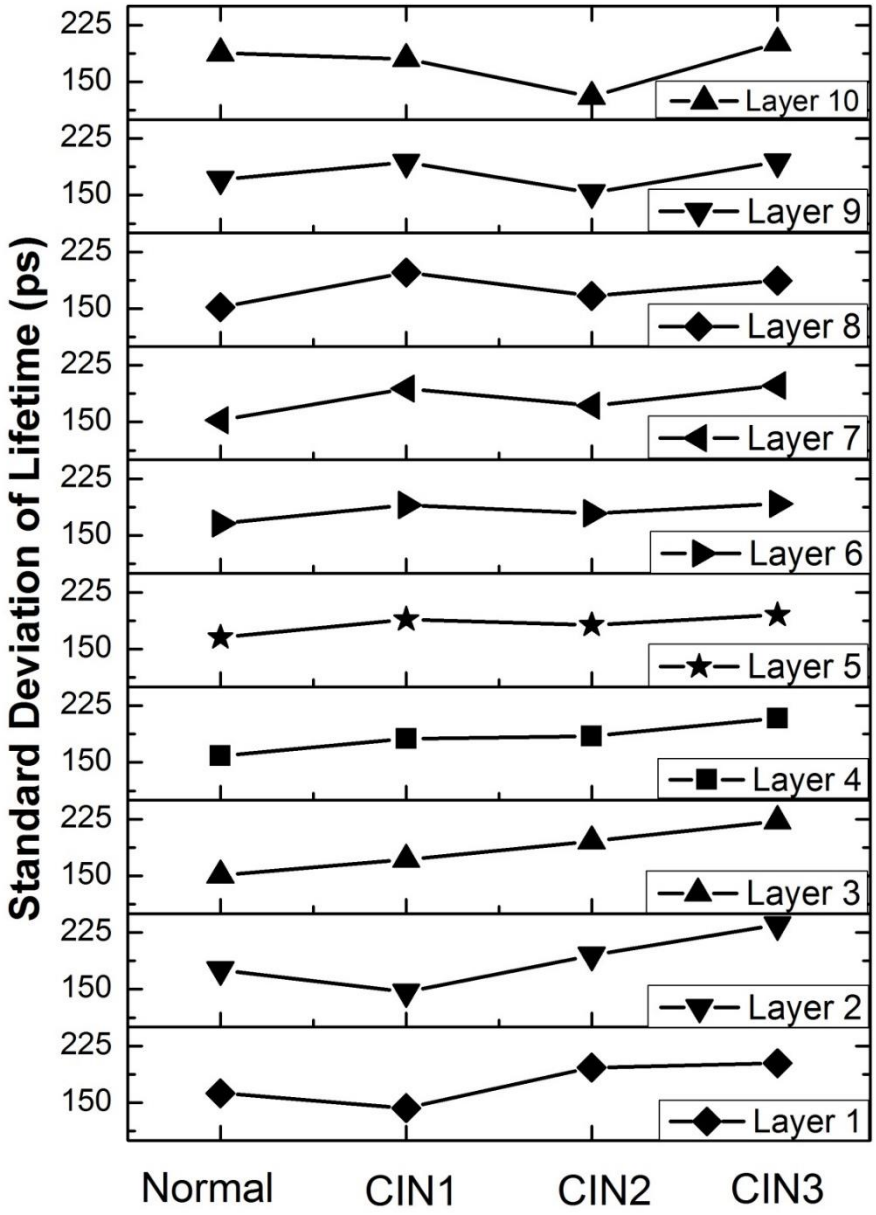

Figure 4-5 Distribution of τ_2 standard deviation in divided layers (from 1 to 10) among different pathological states of normal, CIN1, CIN2 and CIN3 tissues.

The corresponding sensitivity and specificity as a function of the cut-off layer were calculated and shown in Figure 4-7. It can be seen from the plot that when the cut-off layer decreases from 10 to 6, the sensitivity increases slightly from 92.8% to 94.6%

while the specificity rises sharply from 30.1% to 84.3%. Both the maximum sensitivity and specificity occur at the cut-off layer of 6. When the cut-off layer decreases from 5 to 1, both sensitivity and specificity decrease greatly and finally drops to a low value of 55.5% and 51.4%, respectively. The overall maximum sensitivity (94.6%) and specificity (84.3%) occurs when feature components τ_2 from layers (6-10) were used for ELM classification. The proposed epithelium layer analysis with neural network ELM classifier could achieve desirable discriminations between normal and precancerous cervical tissues when multiple feature vectors from mean τ_2 values of layers (6-10) were used. The optimum sensitivity and specificity obtained are 94.6% and 84.3%, respectively. When μ and σ of lifetime τ_2 in the whole epithelium were used to diagnose normal and precancerous cervical tissues, the resulting sensitivity and specificity is 62.2% and 52.3%. Three-layer analysis consistent with the generic definition of CIN achieves a sensitivity of 81.1% and specificity of 39.6%.

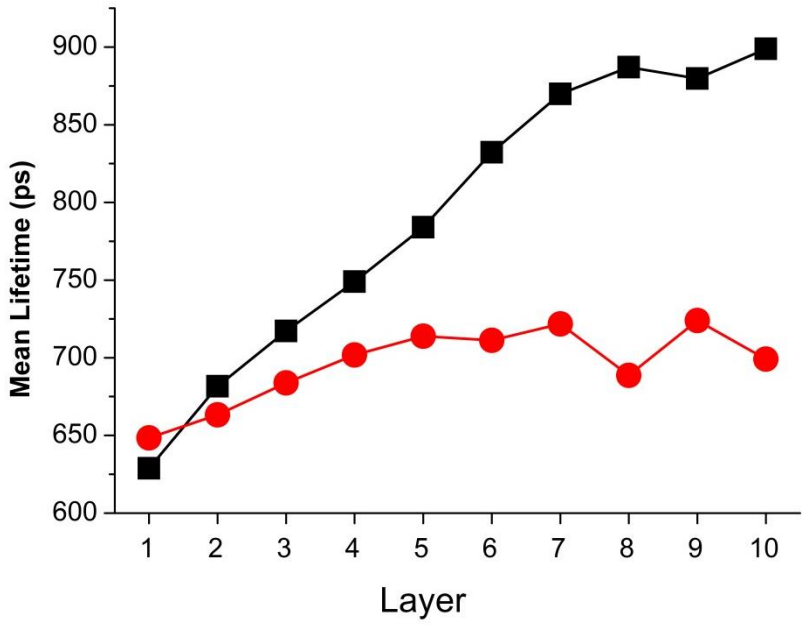

Figure 4-6 Distribution of mean τ_2 in all divided 10 layers for normal (■) and precancerous (●) samples

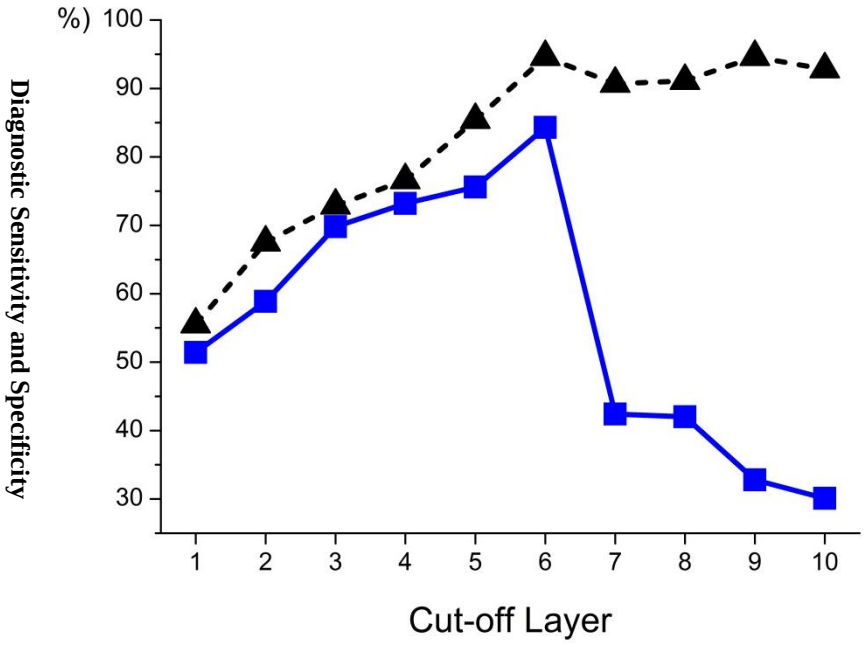

Figure 4-7 Variation in ELM diagnostic sensitivity (▲) and specificity (■) as feature vectors include mean τ_2 values successively from epithelial surface (layer 10) to a lower layer as the cut-off layer. Optimum sensitivity (94.6%) and specificity (84.3%) were concurrently found at the cut-off layer of 6.

Table 4-2 compares the diagnostic accuracies from the various analysis models used in this work. The 10-layer analysis suggests that the top half epithelium (layers 6~10) is the effective zone for FLIM diagnosis with concurrently high sensitivity and specificity. The ELM classification result shows great improvement in overall diagnostic accuracy with sensitivity of 94.6% and specificity of 84.3% in 10-layer analysis as compared to the results of whole-epithelium and 3-layer analysis. The overall accuracy here was calculated by taking the average of specificity and sensitivity and the overall accuracy is about 1.5 times those obtained from whole-epithelium and three-layer analysis. In addition, the computation time for data fitting and ELM classification was also halved as compared to the whole-epithelium analysis that involves data fitting for the whole

Table 4-2 ELM diagnostic sensitivity and specificity derived from various analysis models.

Analysis Model	Sensitivity	Specificity
Whole epithelium	62.2%	52.3%
Three-Layer	81.1%	39.6%
Top 5 layers in Ten-Layer model (layers 6-10)	94.6%	84.3%

epithelium. Lifetime data calculation by NLLS which is in the order of several minutes is computationally intensive and contributes most significantly in the overall processing time [118] while the ELM classification takes only tens of seconds with our system. All ELM computations were carried out in Matlab 6.5 environment running in a Pentium 4, 1.9 GHZ CPU. Since only the top half epithelium is needed to derive mean $\tau 2$ values, the total processing time to calculate the lifetime data was decreased by two fold. The layer analysis proposed in this work leads to a conclusion that FLIM diagnosis of top half epithelium can achieve high diagnostic accuracy with the least computational cost.

4.4.5 Discussion

A 3-layer epithelium model was first studied for comparison with the standard 3-tier histological grading system (CIN1, CIN2 and CIN3) which is based on the proportion of epithelial thickness affected by neoplasia. Lifetime diagnosis with a 10-layer epithelium model was also conducted and the resulting diagnostic accuracy was greatly improved when using only the first 6 layers. This model was investigated because it best represents the biological structure of cervical epithelium comprising 10 cellular layers with

increasing maturity towards its surface. The classification result shown in Figure 4-7 identified the top-half epithelium (layers 6-10) as the most effective region for cervical epithelium diagnosis. The improved diagnostic accuracy with the top-half epithelium can possibly be attributed to the prominent interplay between cellular maturity and eosin molecules. Normal cells are known to differ markedly from CIN cells in their ability to differentiate [119]. Normal cervical cells can differentiate to mature specialized cells as they grow upwards from the basement membrane to epithelial surface [120]. CIN cells, on the other hand, remain immature (undifferentiated) and proliferate vertically with increased abnormalities. It is evident in Figure 4-6 that mean τ_2 of normal cell rises steadily from layer 1 to layer 10 where the cells are fully matured. By contrast, CIN cells show gradual increase in mean τ_2 within the lower half epithelium and minimal change in the top-half layers. The significant difference in mean τ_2 between normal and CIN cells, driven by their differing maturity, therefore constitutes the prominent diagnostic contrast in the top-half epithelium.

The shortening of τ_2 is also observed in "normal" unaffected layers of CIN1 and CIN2, as defined by conventional grading system (Figure 4-4). For instance, while CIN1 cells are in principle confined to the lower one-third epithelial layer according to standard diagnosis, the shortening of τ_2 (indicating precancer development) is still observed in the top-half epithelium. Hence, the shortening of τ_2 is not solely attributed to the presence of immature CIN cells, but also to other possible abnormalities developed in the upper epithelial layers. First, while CIN cells are most prominent in the lower affected layers, abnormalities including increased mitotic activity and nuclear atypia can be present at all layers [121, 122]. Secondly, human papillomavirus (HPV) infection, a

main cause of CIN [123], can result in koilocytosis, a condition where squamous epithelial cells have undergone structural changes in the top-half epithelium [124, 125].

Koilocytosis affects the cytoplasm of cells resulting in cellular changes and can be seen by identifying nuclei surrounded by tiny halos under white light microscopy. Cellular changes including morphological and biochemical changes are involved in the process of cervical dysplasia or even malignancy [42]. Therefore, it is likely that early abnormalities occurring in top-half epithelium involve cellular changes that can contribute to lifetime change of eosin in the cytoplasm [114].

The incorporation of σ of τ_2 in the feature vectors did not improve and may even deteriorate the diagnostic performance, suggesting that σ is not an indicator of cellular abnormalities. This can be explained from the fact that σ illustrates the spread of the τ_2 values and thus the cellular homogeneity in each layer. In the 10-layer epithelium model, each layer would encompass cells of similar types and maturity [120], which is independent of pathological states.

Dimensionality reduction of the raw input variables to extract useful and relevant features is an essential preprocessing step in the classification process [126]. It is necessary to keep the input features concise to reduce computational cost [127] and avoid performance degradation due to redundant and irrelevant features [128]. In this work, σ and τ_2 of lower half epithelium were identified and omitted from analysis.

The origins of the biochemical changes and of the associated eosin lifetime changes as cervical cells become neoplastic warrant further investigation. Understanding the

underlying mechanism to the biochemical changes in the cytoplasm would lead to more effective diagnosis and treatment of cervical cancer. The identification of the more useful diagnostic information in the top-half epithelium suggests that efforts in understanding the underlying biochemical process of cervical cancer development should concentrate on the top-half epithelium.

4.5 Summary

Fluorescence lifetime images of cervical epithelium were divided evenly into multiple layers in the tissue growth direction, perpendicular to the basement membrane, to study the diagnostic value of each layer. In a 10-layer analysis, feature vectors comprising divided layer mean lifetime τ_2 in the top-half epithelium (layer 6 to 10) were used for discrimination by a neural network ELM classifier. Average values for the sensitivity and specificity of 94.6% and 84.3% were obtained when differentiating normal from precancerous (CIN1, CIN2, CIN3) tissues. On the other hand, the 3-layer analysis, which uses feature vectors derived from mean lifetime of τ_2 in each of the three divided layers, results in averag sensitivity of 81.1% and specificity of 39.6%.

The proposed technique has the advantage of achieving a concurrently higher sensitivity of 94.6% and specificity of 84.3% than the sensitivity of 92.8% and specificity of 80.2% obtained in whole epithelium analysis. In addition, analyzing only the top-half of the cervical epithelium is computationally fast with significantly reduced lifetime calculations as redundant feature components were eliminated. The proposed method can provide more accurate and faster cervical diagnosis, which can supplement traditional gold standard histopathological examinations. Furthermore, the reduction of

the feature vector size makes the ELM classifier a potentially more efficient tool when there is a need to analyze a large quantity of data in future applications.

Chapter 5. DIAGNOSIS OF HAEMATOXYLIN AND EOSIN STAINED CERVICAL LIQUID BASED CYTOLOGICAL SAMPLES USING FLUORESCENCE LIFETIME IMAGING

5.1 Motivation

Liquid based cytological (LBC) Papanicolaou test, or better known as Pap smear, is a common tool to screen for cervical intraepithelial neoplasia (CIN), a pre-invasive stage of cervical carcinomas, and its use has resulted in a marked decrease in cervical carcinoma mortality. However, the Pap smear screening has low sensitivity and specificity. In addition, it requires highly trained personnel to screen the slides, making it time-consuming, labor-intensive and expensive. In this work, a new screening modality to supplement the automated screening and improve the accuracy of LBC Pap smear diagnosis using FLIM technique is investigated.

5.2 Introduction

5.2.1 Liquid Based Cytological (LBC) Papanicolaou Test

Since the introduction of Papanicolaou (Pap) smear test in 1943 [129] to diagnose precancerous lesions, tremendous success has been witnessed in the prevention of cervical cancer. The underlying concept of the Pap test is to treat cervical cancer at its early stage through detecting early cervical cellular changes. In the Pap smear, a speculum is used to open the vaginal canal and cells are collected from the cervix for

microscopic examination. Cytological cells are multichromatically [130] stained which results in transparent cells for identification. Five dyes are involved in a classic Pap stain [131]: haematoxylin stains cell nuclei crisp blue to black, orange G stains keratinizing cells yellow, eosin Y stains superficial squamous cells orange to pink, light green SF yellowish stains the cytoplasm of all other cells turquoise green to blue and bismarch brown stains nothing and is often neglected. Morphological criteria are conventionally being used to detect the presence of precancerous cells from the smear samples [132].

Squamous cell carcinomas represent most cases of cervical carcinomas and are classified by a three-tier (CIN) or two-tier (Bethesda) cytological grading systems [133]. In the three-tier CIN grading system, CIN1 (moderate dysplasia) refers to cytological cells with disproportionate nuclear enlargement in which the nucleus usually occupies less than half of the cell area. In CIN2 (moderate dysplasia), the nucleus usually occupies one-half to two-thirds of the total cell area. In CIN3 (severe dysplasia), the nucleus would occupy at least two-thirds of the total cell area [42].

However, the conventional Pap test is not very accurate. A sensitivity of 47% and a specificity of 60% are typically achieved [121, 134]. Therefore, the liquid-based cytology (LBC) Pap test was introduced to improve the diagnostic accuracy. In LBC, a fluid transport medium was adopted to preserve the collected cervical cells [135]. The cell suspension is then processed, which results in a uniform, thin and even layer of cervical cells. The LBC Pap test slide is clear, easier to read and obscuring factors such as blood, mucus and debris are minimized. In addition, a larger number of representative cells are obtained from the sampling device. Therefore, LBC enhances the sample quality and increases microscopic readability that leads to an improved diagnostic

accuracy. Many publications have indicated that LBC has improved accuracy in diagnosing cervical neoplasia as compared to the conventional Pap smear [136]. A sensitivity of 78% and specificity of 73.3% were reported with LBC from in the clinical setup [137].

5.2.2 Drawbacks of LBC and Automated Screening Systems

In LBC diagnosis, cervical cell collection, staining and slide preparations are followed by slide reporting. In the final reporting stage, an experienced cytopathologist is required to examine the slide and make a decision if it is normal or neoplastic [135]. However, disease reporting is resource demanding. To deliver reliable and efficient diagnosis, highly educated and proficiently trained personnel are indispensable. A long training period of up to 24 months is required for cytopathologists and extensive theoretical and practical training are involved. In addition, the number of neoplastic cells is very small as compared to normal cells. A typical LBC slide could have nearly 100,000 cells and more than 90% of the cells are normal [133]. It is therefore a challenging task to search for the small number of precancerous cells for diagnosis. Under 10× magnification, approximately 1000 fields of view are scrutinized to accomplish one slide examination. An average of 5-10 minutes are required to inspect a single slide [138] and fatigue risks are always present [139]. All these drawbacks make LBC screening time-consuming, labor-intensive and inaccurate [140].

Many automated screening systems with image processing modules have been developed to overcome these challenges [141-145]. Cytological slides were

automatically fed into the screening system, automatically focused and imaged. Features such as nuclear size, optical density, nuclear density, nuclear shape, cytoplasmic area and nuclear/cytoplasmic ratio and even chromatin were extracted from cell images to make predictions. However, only morphological features were used to describe cytological cells. There are many issues existing in the image segmentation, which is a crucial stage in the image processing guided diagnosis. For example, thresholding value based grayscale segmentation could not solve the problem arising from staining intensity variation [146]. Although more complicated and refined approaches have been developed to address these problems [147-149], none of these techniques are as effective as human eyes. One important reason is attributed to the staining conditions, which can affect the accurate detection of the nucleus and cytoplasm.

5.2.3 FLIM Diagnosis of H&E Stained Cervical LBC Samples

Biochemical information, which is an important parameter to make accurate diagnostic assessment [150], is rarely studied to describe the different stages of Pap cells. The results obtained in Chapter 3 showed that FLIM is especially useful for characterizing the biochemical changes in cervical tissues. In addition, FLIM is independent of staining intensity artefacts, which makes it a potential tool for Pap cell imaging and automated screening. In this chapter, a new screening method to improve the accuracy of automated LBC Pap smear diagnosis using FLIM technique is investigated. Eosin lifetime from cellular regions was used as a feature vector and fed into a neural network ELM classifier for discrimination. A concurrently high sensitivity of 92.6% and specificity of 71.2% were achieved in diagnosing precancerous cervical cells. This preliminary study

suggests that the proposed method could supplement and improve the automated screening of cervical LBC samples.

5.3 Materials and Methods

5.3.1 Sample Set

A total of 46 H&E stained cervical liquid based cytological slides from KK Women's and Children's Hospital (KKH), Singapore were collected for the FLIM imaging and analysis conducted in this work. Slides for selected cases were processed from LBC vials according to the ThinPrep™ protocol and stained with only H&E. These cytological slides were pathologically examined by a senior consultant from KKH and the identified cervical cells on the slides were classified as normal, CIN1, CIN2 and CIN3. The sample set includes 20 normal, 12 CIN1, 6 CIN2 and 8 CIN3 cervical cytological slides. Each identified single cell or a cluster of non-overlapping cells was defined as a region-of-interest (ROI). A total of 74 ROIs were identified for investigation.

5.3.2 Imaging Protocol and Lifetime Calculation

The H&E stained cervical cytological slides were imaged with the FLIM system described in the previous chapter [114]. The excitation power was adjusted to 20% of its maximum output. Since cellular structures on cytological slides were studied, a 40× magnification objective lens was used to focus the scanning beam and to collect the emission light. Each lifetime image was obtained with a scanning time of 60 s and the three-dimensional image size (x, y, t) was fixed at 256×256×256 pixels. The spatial

resolution is approximately 1 μm per pixel and the fluorescence decay was recorded within a time window of 10 ns and a temporal resolution of ~39 ps.

A double exponential model of the fluorescence decay was used for curve fitting. Lifetime values, τ_1 and τ_2, were calculated using an iterative nonlinear least squares (NLLS) algorithm. The longer lifetime component τ_2 distribution was found to generate notable diagnostic contrast among various cervical cancer stages. On the other hand, the shorter lifetime component τ_1 with a typical value of ~30 ps and was attributed to instrumental response time and has no correlation to tissue cytopathology. A false-colored lifetime image consisting of 256×256 pixels was generated by mapping a specific color to the lifetime value of τ_2 at each pixel.

5.3.3 Cervical Whole Cell and Cytoplasm Analysis

Lifetimes from cervical cytological slides were analyzed in both whole cells and cytoplasmic regions. The cytoplasmic region lifetime was studied because lifetime in the nucleus region might contribute significantly to the overall whole cell lifetime and bias the overall lifetime. It has been determined in Chapter 3 that the lifetime τ_2 originates from eosin which stains the cytoplasmic region of a cell. In addition, the nucleus occupies half or even more than two thirds of the total cell area in neoplastic or dysplastic cells [42]. It is important to eliminate the impact of nucleus lifetime before discriminations are made since cellular level structure is specially investigated.

Figure 5-1 shows the regions identified for whole cell and cytoplasmic analysis. In whole cell analysis, mean (μ) and standard deviation (σ) of τ_2 were calculated from the

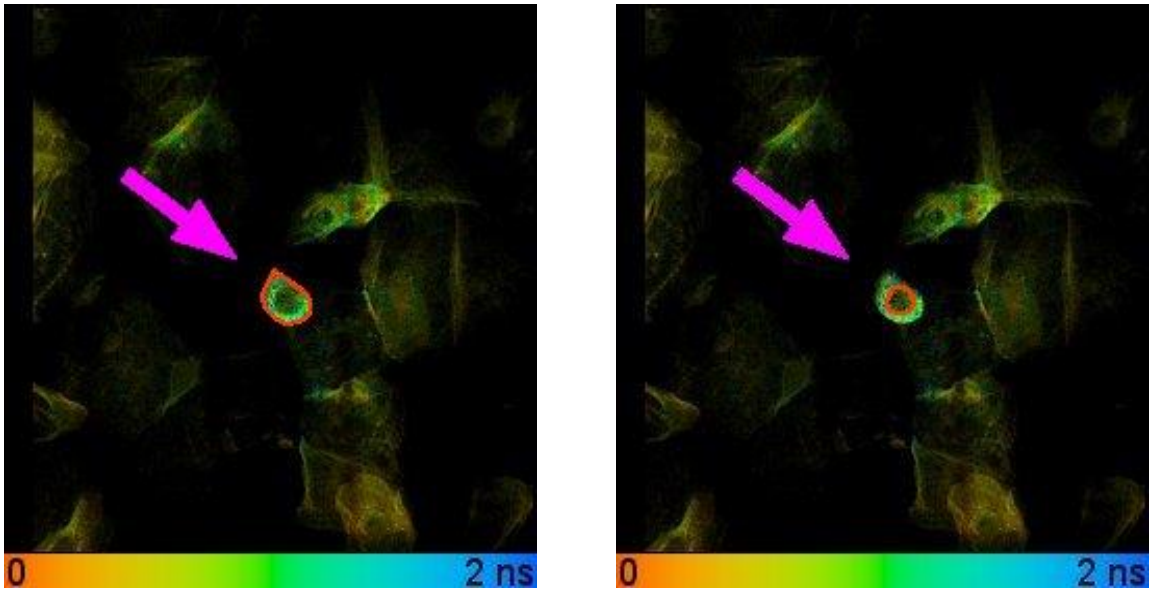

(a) (b)

Figure 5-1 A typical fluorescence lifetime image of H&E stained cervical cytological slide with a CIN1 ROI segmented. The pink arrow indicates the ROI. (a) Whole cellular region segmented, (b) nucleus region segmented.

lifetime values exported from the overall cellular region which include the nucleus and cytoplasm as depicted in Figure 5-1a. In the cytoplasm analysis, lifetimes determined from the nucleus (Figure 5-1b) were excluded from the whole cell lifetimes, and mean and standard deviation of of τ_2 were calculated from the remaining lifetimes in the cytoplasm.

5.3.4 Feature Vector and Parameters in Extreme Learning Machine Classifier

The mean τ_2 for a whole cell was used as a feature vector for classification. Discriminations between normal and precancerous (CIN1, CIN2, CIN3) cervical cytological samples were performed using the neural network ELM classifier described

in chapter 3. To achieve the maximum discrimination accuracy, the number L of hidden nodes was adjusted. The total number of feature components in each sample was specified by n. In this work, only mean τ_2 was used as a feature vector and thus n=1. The parameter m indicates the two possible pathological states of the cervical tissue sample, i.e. normal or precancerous, and takes a value of 2.

Cross-validation was applied to discriminate between histologically identified normal and precancerous samples. The feature vectors from 37 randomly selected samples were chosen as training data while the feature vectors from the remaining 37 samples were used for testing. 1000 random sets of training and testing data were generated for computation. The resulting sensitivity and specificity for each set of training and testing data were calculated using the neural network ELM classifier. Finally, the mean sensitivity and specificity were computed accordingly for comparison.

5.4 Results and Discussion

5.4.1 Measured Lifetimes of H&E Stained Cervical Cytological Slides

The fluorescence emission spectra of the five Pap stain dyes were measured and only eosin Y was found to give fluorescence (Figure *5-2*). Therefore, only haematoxylin and eosin were used for Pap cell staining. Figure 5-3a shows a white-light microscopic image of a typical H&E stained CIN2 cervical cytological slide and Figure 5-3b shows the corresponding fluorescence lifetime (τ_2) image. Besides the three CIN2 cells shown in the white-light image, the other larger cells are normal squamous epithelial cells. These normal cells have tiny dark nuclei and pinkish cytoplasm with low nuclear/cytoplasmic ratio. Endocervical cells are also present in the slide, which is proof

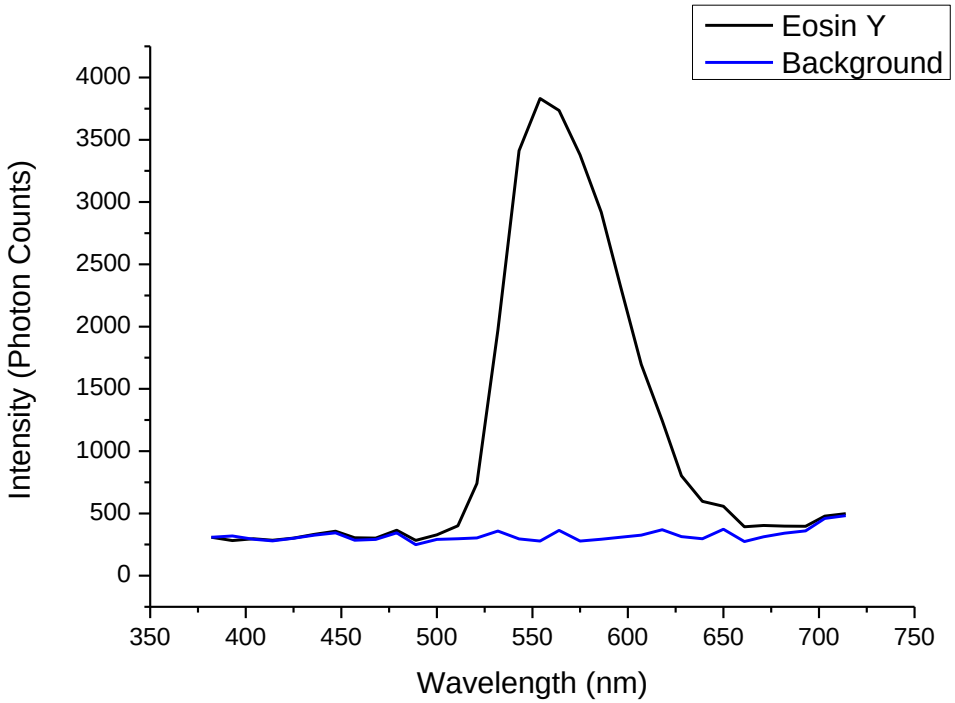

Figure 5-2 Emission spectrum of eosin Y (blue line shows the background dark photon counts) collected at the wavelength range of 380 nm to 715 nm. The excitation wavelength is 760 nm at two-photon excitation.

of a good quality sample collection. Endocervical cells are seen in sheets and groups or loosely associated. The cytoplasm is delicate and the nuclei are rounded. The chromatin pattern is fine with one or more small nucleoli. As compared to Figure 5-3a, it can be seen from Figure 5-3b that some cells have no fluorescence lifetime. This is due to the overlapping of cells so that they are out-of-focus during FLIM measurement. The negligible fluorescence collected from the out-of-focus regions was excluded from lifetime calculation since a threshold value of 50 photons was set. Mean of the lifetime τ_2 from the ROIs was used as a feature vector for discrimination. distribution of cytological whole cells from the cervical samples used in this work. It can be seen from the figure that normal cells generally have smaller mean lifetimes

5.4.2 Lifetime Distribution in Cervical Cytological Whole Cells

Figure 5-4 shows the scatter plot of mean and standard deviation of lifetime τ_2

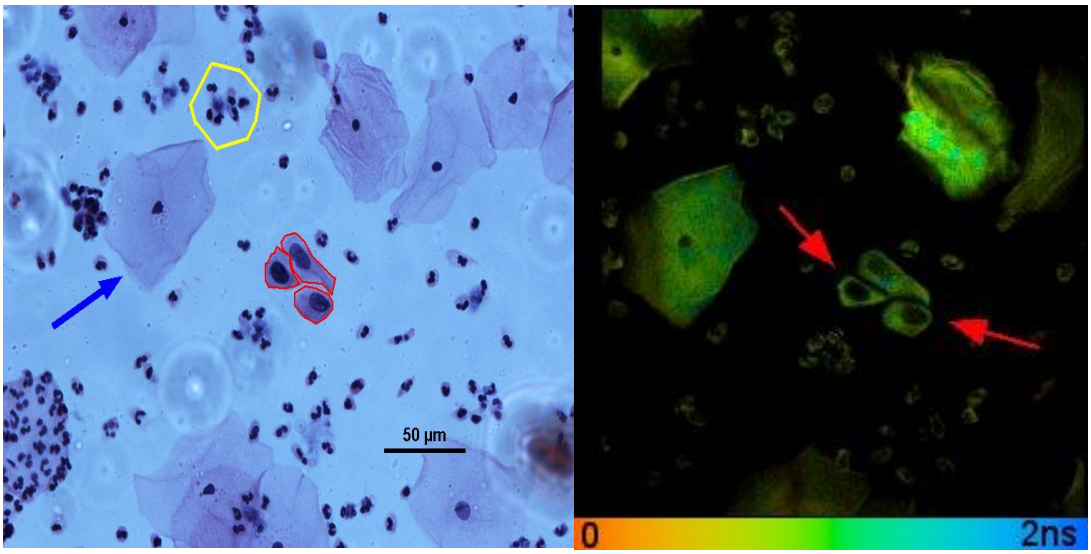

(a) (b)

Figure 5-3 A typical H&E stained CIN2 cervical cytological slide with three ROIs defined, each ROI containing one of the three cells outlined by red lines. (a) White light image of the H&E stained cytological slide. The Blue arrow points to a typical normal squamous epithelial cell and the yellow circle illustrates some endothelial cells (b) False color fluorescence lifetime image with scale bar from 0 to 2 ns.

ranging from 650 ps to 950 ps while precancerous cells have lifetimes of 800 ps to 1150 ps. It is also observed that standard deviation of lifetime τ_2 appears to be featureless. Both the normal and precancerous cells exhibit similar standard deviation ranging from 75 ps to 425 ps.

To better visualize the distribution of mean and standard deviation values of τ_2, their respective distribution profiles were plotted against the cytological stages and shown in

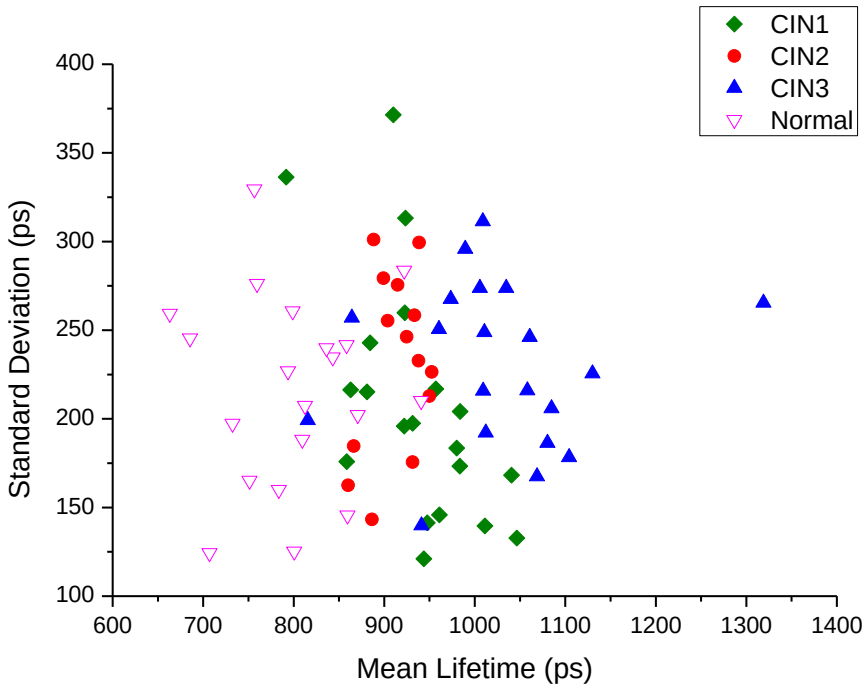

Figure 5-4 Scatter plot of feature vectors from whole cell lifetimes of cytopathologically normal (▽) and precancerous cervical samples including CIN 1 (◆), CIN 2 (●) and CIN 3 (▲).

Figure 5-5 and Figure *5-6*. In the mean τ_2 distribution profile (Figure 5-5), a consistent trend of lengthening was observed as cytological cells progress from normal to CIN3, except for CIN2, where τ_2 has a very slight decrease when disease stage transits from CIN1 to CIN2. The mean value of τ_2 of CIN (CIN1, CIN2 and CIN3) is on average ~150 ps larger than that of normal samples. The distribution for the standard deviation of τ_2 distribution was also investigated (Figure *5-6*), but it did not show any distinction between normal and CIN samples. The standard deviation of τ_2 generally has an averaged value of ~220 ps and the maximum difference of ~25 ps is observed between those of CIN1 and CIN3. Therefore, it was concluded that standard deviation of τ_2 is featureless and uncorrelated to cervical cytopathology.

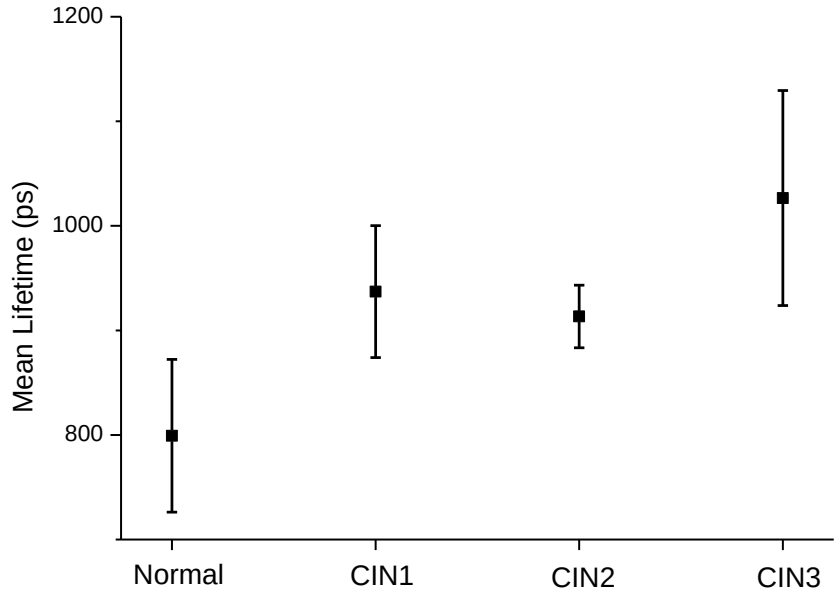

Figure 5-5 Distribution of mean τ_2 in cervical cytological whole cells among different cytological states of normal, CIN1, CIN2 and CIN3 slides with error bar. Here, the mean τ_2 for each cytological state was calculated from the 74 ROIs originated from 20 normal, 12 CIN1, 6 CIN2 and 8 CIN3 cytological slides.

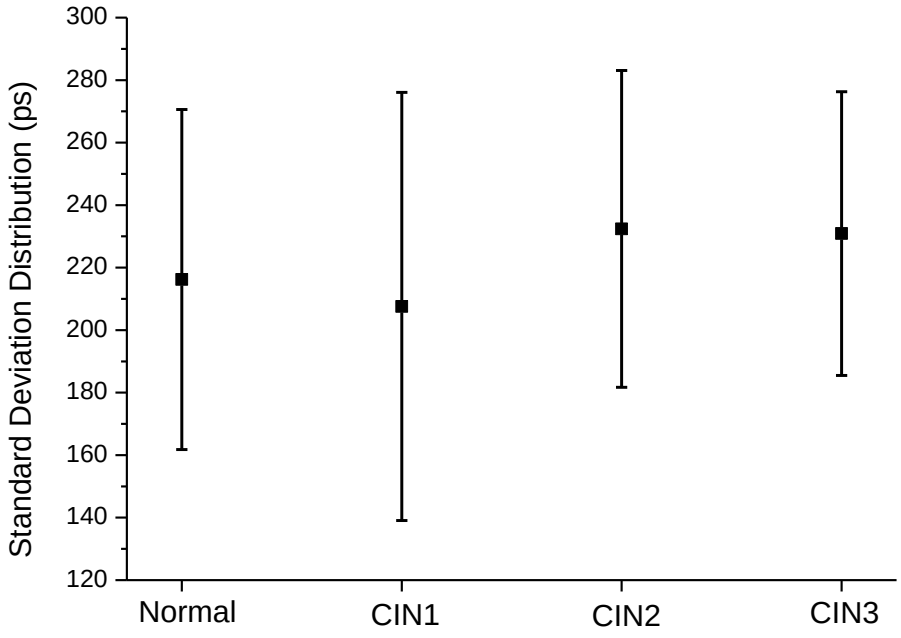

Figure 5-6 Distribution of σ of τ_2 in cervical whole cells among different cytological states of normal, CIN1, CIN2 and CIN3 slides with error bar.

The results indicate that feature vectors should not include the standard deviation of τ_2 for classification and therefore only mean τ_2 was used for discrimination in the subsequent analysis.

5.4.3 Lifetime Distribution in Cervical Cytological Cell Cytoplasm

Figure *5-7* shows the mean τ_2 distribution profile in cervical cell cytoplasmic regions against various cytological stages. It can be seen from the figure that the distribution profile is highly consistent with the profile derived in cytological whole cell regions (Figure 5-5). The biggest difference occurs in CIN2 where the mean τ_2 exhibits a ~13 ps decrease in the cytoplasmic analysis as compared to the whole cell analysis (Table 5-1). In addition, a similar shortening trend was observed as cytological cells progress from normal to higher grade of dysplasia.

The distribution of the standard deviation of τ_2 measured from the cytoplasm region was also investigated and a similar result was obtained. The standard deviation of τ_2 distribution in the cytoplasm shows a highly consistent result with those from the whole cell lifetime distribution. Since it does not carry any diagnostic information to distinguish normal and CIN samples, it is not included in the discrimination algorithm.

5.4.4 Discrimination Result Using Extreme Learning Machine Classifier

The discrimination results for normal vs. precancerous cervical cytological samples with the proposed method are shown in Table 5-2 and compared with the reported visual inspection of LBC in clinical situations.

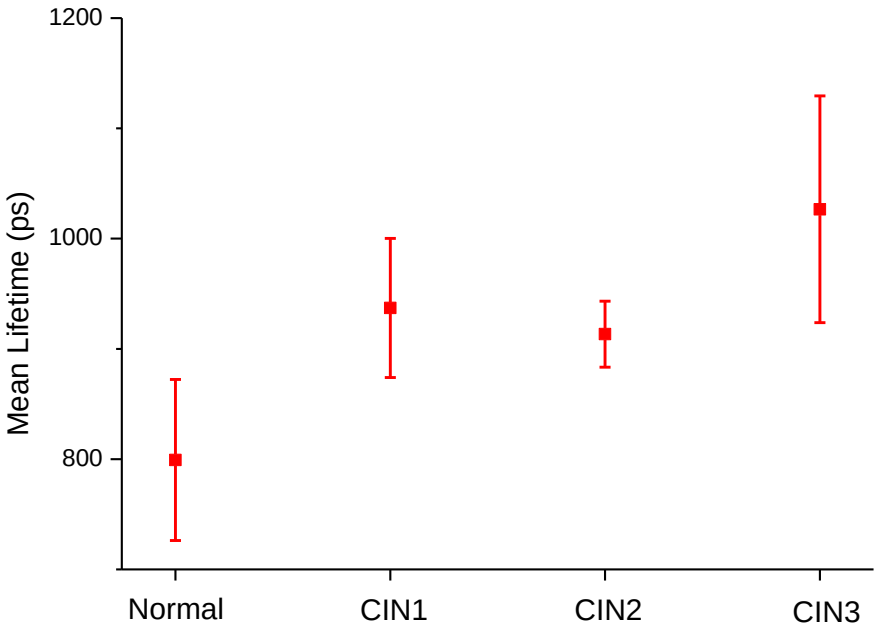

Figure 5-7 Distribution of mean τ_2 in cervical cytological cytoplasm among different cytological states of normal, CIN1, CIN2 and CIN3 slides with error bar.

Table 5-1 *Values of mean τ_2 calculated from cervical whole cell and cytoplasmic regions among different cytological stages of normal, CIN1, CIN2 and CIN3*

Analysis Method	Mean τ_2 (ps)			
	Normal	CIN1	CIN2	CIN3
Whole Cell	799.6	941.5	900.4	1025.6
Cytoplasmic	799.3	937.1	913.4	1026.6

The neural network ELM classifier achieved a concurrently high sensitivity of 92.6% and 71.2%, respectively. As compared to visual inspection in clinical LBC settings, a significant improvement of sensitivity (92.6%) could be achieved with the proposed FLIM technique used in this work and the specificity is not compromised.

Table 5-2 Averaged sensitivity and specificity of discriminating normal vs. precancerous cervical cytological samples derived from different screening methods.

	Screening Method	
	Proposed FLIM	Visual Inspection
Sensitivity	92.6%	78.0%
Specificity	71.2%	73.3%

5.4.5 Discussion

This work reveals that the fluorescence lifetime from H&E stained cervical LBC cells could be used to distinguish normal and precancerous cells. As the disease stage progresses from normal to CIN3, the mean of lifetime component τ_2 shows an increasing trend. This trend allows a discrimination to be made between normal and neoplastic cells. At first glance, the work presented in this chapter is similar to those carried in the previous chapters where lifetimes from H&E stained cervical tissue sections were used for discriminations. However, the scientific implication is significant. Cellular information rather than histological information was utilized to make the diagnosis. The Pap smear cytological diagnosis refers to an earlier identification of precancerous lesions as compared to histology, which is conducted following an abnormal Pap smear

diagnosis for a definitive diagnosis. Cytological diagnosis, however, helps determine the subsequent diagnostics steps and reduce the unnecessary biopsies [151]. In addition, the cytological smear test is less invasive and no pain is caused while histology is invasive and bleeding can be excessive [152].

Since only cervical cellular contents were studied in this chapter and the studied fluorescence lifetime component τ_2 originates from the eosin stained cytoplasmic region, whole cell and cell cytoplasmic lifetime were analyzed respectively, to explore the impact of the nucleus region on the measured lifetime τ_2. In general, there should not be any fluorescence from the nucleus since the eosin stains the cytoplasm and the haematoxylin stains the nucleus. Haematoxylin does not give any fluorescence while eosin is the fluorescing fluorophore. However, a small quantity of eosin can be present in the nucleus during the staining process [153] resulting in fluorescence emission from the nucleus. It is concluded from the results that the nucleus fluorescence lifetime presents only a negligible contribution to the overall whole cell fluorescence lifetime. Moreover, measuring only the cell's fluorescence lifetime supplements in a complementary way to the work conducted in the previous two chapters when fluorescence lifetimes from whole cell tissue sections were used for discriminations. The results obtained in this chapter support the conclusion that these lifetimes are representative of the cytoplasmic regions in which they originate.

The conventional Pap smear screening is conducted by cytotechnologists, who examine the cell samples for signs of malignancy under a light microscope. A typical of about one year of specialized training is required for a hospital laboratory cytotechnologist. In many hospitals, the Pap smear sample is examined by a cytopathologist and finally

confirmed by a medical doctor specializing in cellular pathology. The time required for the examination of a Pap slide is on average 5-10 minutes, although there might be variations on how difficult the sample is. However, due to the hazards of fatigue, a cytotechnologist should not work more than 7 hours a day and analyze no more than 70 samples [154]. While for our proposed new approach, once the sample is loaded, it could automatically image the whole slide, analyze the images and conduct classifications with the aid of computer aided algorithms. The technique is supposed to save time if it is successfully translated. In addition, highly trained personnel are replaced by standardized machines which could be easily replicated and promoted in developing countries where specialized personnel are not available.

It was also found that the fluorescence lifetime component τ_2 increases when cells progress from normal to CIN3, which is inconsistent with the trend observed in H&E stained tissue sections. In the tissue section analysis, a decreasing trend in mean τ_2 was obtained. This may be due to the sample preparation process and is further investigated in Chapter 6.

5.5 Summary

H&E stained cervical LBC cells were studied using fluorescence lifetime imaging. The resulting lifetime images were processed to extract the lifetime values for whole cell and cytoplasmic regions for analysis. The results show that the whole cell fluorescence lifetime distribution is highly similar to the cytoplasmic one. The mean lifetime component τ_2 in the whole cell region was used to differentiate between normal and precancerous cells. High sensitivity and specificity of 92.6% and 71.2%, respectively,

were achieved. This sensitivity is significantly higher than that of visual inspection of LBC samples while the specificity is comparable. In addition, biochemical information derived from the fluorescence lifetime is independent of staining intensity artefacts and could be used in automated LBC screening. This can overcome the segmentation problems introduced by staining intensity variations. The proposed method can supplement the automated screening and improve the accuracy of the LBC Pap smear diagnosis.

Chapter 6. INVESTIGATION OF THE BIOCHEMICAL ORIGINS OF EOSIN FLUORESCENCE LIFETIME DIFFERENCES IN CERVICAL PRECANCER

6.1 Motivation and Introduction

Fluorescence lifetime imaging microscopy (FLIM) has been demonstrated in the preceding chapters to be an effective methodology to characterize the H&E stained cervical tissue sections and liquid based cytological (LBC) Papanicolaou smears. The characteristic decay rate of the excited state fluorophore eosin, which stains the cytoplasm, was used to discriminate cervical precancer at different stages. However, the underlying biochemical mechanism that leads to the observed fluorescence lifetime differences is not elucidated. In this chapter, we aim to develop a hypothesis to relate cervical cancer progression to the associated fluorescence lifetime changes.

In previously reported study, commonly existing proteins, which include bovine serum albumin (BSA), poly-L-arginine, poly-L-histidine, poly-L-lysine and poly-L-tryptophan were used to simulate the proteins in cervical cytoplasm [155]. These proteins were mixed with eosin Y, which is the only fluorophore involved in the H&E staining of cell cytoplasm [156, 157] to form the protein-dye complex. The pH level in the protein-dye complex solutions was varied to simulate cellular biochemical environments associated with early cervical cancer since changes in the cellular pH value is often associated with cancer progression [158, 159]. Fluorescence lifetime originating from the protein-dye complex under different pH values were measured and

compared. It was found that as tissue pH value decreased, the fluorescence lifetimes of poly-L-arginine and poly-L-lysine also decreased compared to the value of their respective protein-dye complex. This could well explain the shortening lifetime obtained in FLIM diagnosis of H&E stained tissue sections.

By contrast, this is contradictory with the fluorescence lifetime lengthening trend acquired in FLIM diagnosis of LBC cells. The sample preparation protocols of both methods were scrutinized for both methods and xylene was found to be used in the LBC cells preparations but not used in tissue section preparations. Xylene was identified as a key chemical that might cause the different trend of lifetime changes in LBC samples. This is based on the conclusion that the presence of fluorophore solvent affects its excited state decay rate [160, 161]. Xylene was thus added to the protein-dye complex solutions and lifetimes were measured under different pH values. It was found that as tissue pH value decreased, offer the addition of xylenes, the lifetimes of poly-L-histidine and poly-L-lysine increased compared to the value of their respective protein-dye complex. The results are consistent with the lifetime lengthening trend obtained in FLIM diagnosis of H&E LBC cells.

6.2 Material and Methods

6.2.1 Reagents

Eosin Y powder was purchased from Merck (Germany) and BSA Powder was obtained from Sigma-Aldrich (USA). Poly-L-amino acids, which include arginine, histidine, lysine and tryptophan, were procured from Sigma-Aldrich (USA). Acids and all other reagents used in this work were of analytical grade and were acquired locally.

6.2.2 Preparation of Solutions

Eosin Y stock solution was prepared as follows: eosin Y powder was firstly dissolved into 100 ml water and 50 ml was taken out from the solution and mixed with 395 ml of 95% alcohol. Another 2 ml of acidic acid was subsequently added to make the color of eosin Y solution brighter for better staining effect [162]. 1 ml eosin Y stock solution was then diluted with 10 ml 95% alcohol so that the concentration of eosin Y solution in the test assay was set to 0.1% (0.1 g/100ml). BSA was dissolved in 0.15 M NaCl and poly-L-tryptophan was dissolved in dimethyl sulfoxide (DMSO). Poly-L-arginine, ploy-L-histidine and ploy-L-lysine were dissolved in distilled water. The working concentration of BSA and all poly-L-amino acids was 1 mg/ml.

6.2.3 Absorption Spectrum of Protein-Dye Complex Solution

Since eosin Y and protein binds electrostatically [163], the amount of protein-dye complex is proportional to the amount of proteins involved in dye bindings. To ensure that every measured lifetime originated only from the individual protein-dye complex formed, the absorbance spectrum of the complex was measured. In chemistry, absorbance is defined as: $= log_{10} \frac{I_0}{I_1}$. A is the absorbance, I_0 refers to the incident light intensity while I_1 refers to the output light intensity.1 ml of eosin Y solution was firstly added to a disposable cuvette and varying amounts of protein were added for dye binding. The absorbance spectrum was measured with a spectrofluorometer (Fluorolog-3, Jobin Yvon) in the wavelength range from 400 nm to 650 nm. The reagent blank solvent is 95% alcohol.

6.2.4 Fluorescence Lifetime Measurement

BSA and individual polyamino acids were first pipetted into disposable centrifuge tubes. 1 ml eosin Y solution was then added to each of these centrifuge tubes and mixed for more than 2 minutes to form stable water-soluble protein-dye complex [164]. These mixed solutions were then transferred to a concave glass slide by a pipette and mounted with a coverslip for lifetime measurement (Figure 6-1). The same fluorescence lifetime measurement system was used and the parameter configurations are the same as those described in chapter 3 [114]. Lifetimes from three different regions on a slide were measured to ensure consistency of results. Since the protein-dye complex is less stable after 60 minutes of formation [164], all measurements were completed within 1 hour after complex formation.

To measure the effect of pH on the lifetime of protein-dye complex in the mixed solution, 0.13 M HCL, 1 g/ml NaOH and 10 g/ml NaOH were used to vary the pH values. Corresponding lifetimes were measured at a wide range of pH values. When neither was added, the pH value was measured to be 6. A pH=2.06 was achieved by adding 13.34 µl HCL and 13.34 µl 1 g/ml NaOH was then added to increase the pH value to 3.96. While another 13.34 µl 10 g/ml NaOH was added to increase the pH value to a value of 8.35.

To determine the interference of solvent to protein-dye complex lifetime, 3.33 µl of xylene was added and lifetime values were measured under various pH values. The pH of xylene is neutral (pH=7.04) and does not affect the overall pH value of the mixed solution. The same amount of HCL and NaOH were added to adjust the pH values to the corresponding values.

Fluorescence lifetime calculations were conducted using SPCImage software (Becker & Hickl, Germany). The measurements were then fitted to extract the lifetime values to a fluorescence decay model with NLLS algorithm.

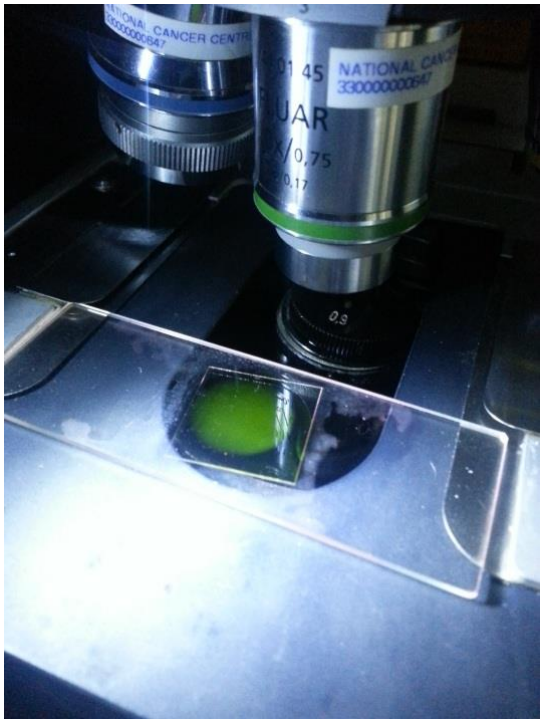

Figure 6-1 Fluorescence lifetime measurement of a typical BSA and Eosin Y mixed solution. The solution is stored in the cavity of the glass slide and a cover slip was mounted on top of the cavity.

6.3 Results and Discussion

6.3.1 Absorbance Spectrum of Dye Protein Complex

Figure 6-2 shows the absorbance spectrum of eosin Y and poly-L-arginine complex measured at pH=2.06. Before arginine was added, eosin Y exists in the neutral form [163] with absorbance maximum at ~485 nm. As arginine was added, a new absorbance

maximum starts to appear. The absorbance maximum was found at 530 ± 2 nm and the peak value of the absorbance maximum increased as arginine volume increases. The increase of absorbance maximum is attributed to the formation of a new protein dye complex [163]. Similar spectra of BSA and other poly-L-amino acids were obtained. Except for tryptophan, the absorbance of the protein-dye complex increases with the volume of BSA or poly-L-amino acids. When the same volume of protein was added, BSA showed the highest protein-dye complex amount while lysine had a much lower amount. For tryptophan, the absorbance value remained constant when the protein amount was increased from 50 µl to 400 µl, suggesting that there was minimal complex formation.

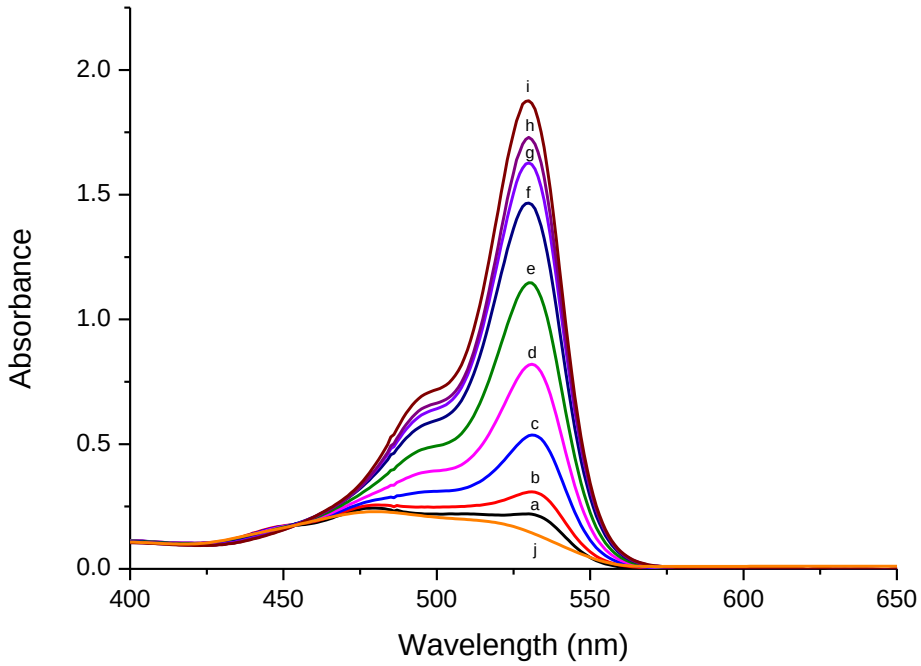

Figure 6-2 Absorbance spectrum of dye-protein complex obtained at various poly-L-arginine volumes with a concentration of 1 mg/ml at pH 2.06. (a) 25 µl (b) 50 µl (c) 100 µl (d) 150 µl (e) 200 µl (f) 250 µl (g) 300 µl (h)350 µl (i) 400 µl (j) 0 µl. All spectrums were recorded against 95% alcohol.

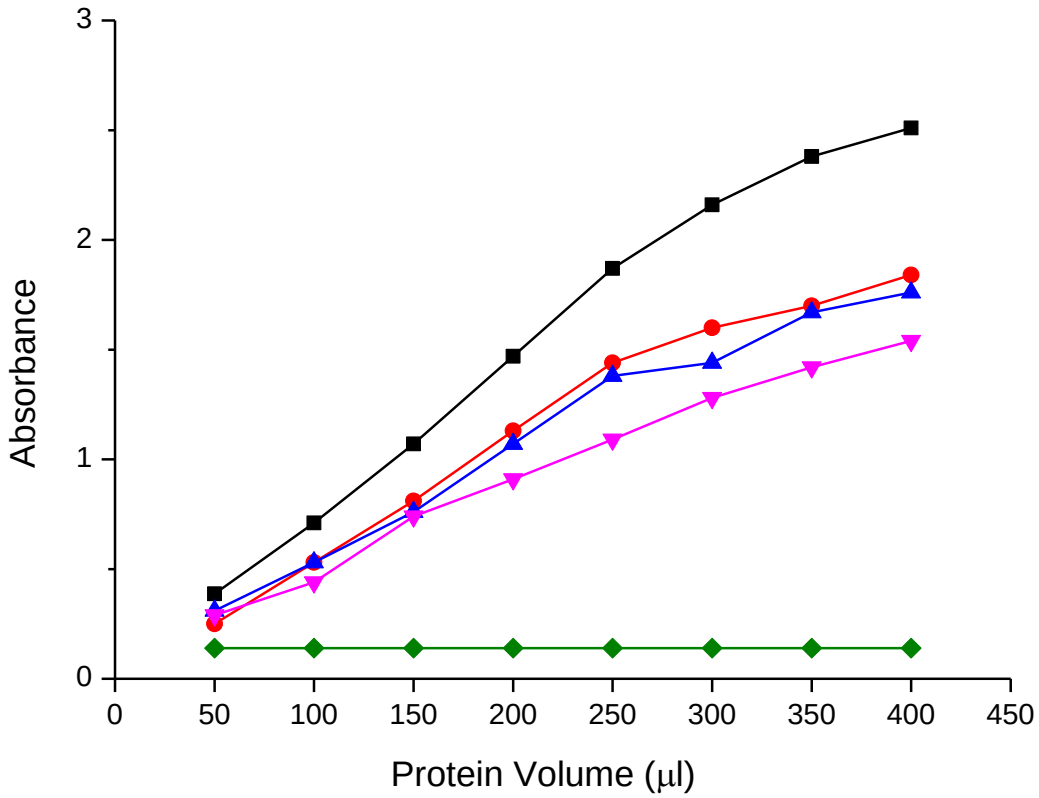

Figure 6-3 Absorbance of the dye-protein complex produced by increasing the volume of BSA (■), poly-L-arginine (●), poly-L-histidine (▲), poly-L-lysine (▼) and poly-L-tryptophan (◆) with a concentration of 1 mg/ml at pH 2.06. The absorbance was recorded at 532 nm.

From *Figure 6-3* a horizontal line with a constant absorbance value of 1 was randomly selected to intersect with the complex absorbance curves and the corresponding protein volume (Table 6-1) was calculated. A volume of 200 µl of poly-L-tryptophan was used for protein binding and the corresponding lifetime was measured for comparison

6.3.2 Fluorescence Lifetime Values at Different Solution pH values

Fluorescence lifetime measurements were obtained for various protein-dye complex solutions under pH values of 2.06, 3.96, 6 and 8.35.

Table 6-1 Binding proteins and their corresponding volumes at pH 2.06

Binding Proteins	**Volume (μL)**
BSA	140.6
Poly-L-Arginine	181.1
Poly-L-Histidine	188.3
Poly-L-Lysine	223.2
Poly-L-Tryptophan	200

It can be seen from Figure 6-4 that the protein-dye complex of arginine and lysine are sensitive to solution pH values. Take poly-L-arginine as an example, eosin-arginine complex solution appears light orange under pH=2.06 and moderate pink under pH=8.35. This suggests that some functional groups of the protein-dye complex might have changed with the solution pH values.

The corresponding lifetimes of protein-dye complex under different pH values are shown in Table 6-2 . It is observed that when BSA, histidine and tryptophan bind with eosin Y the resulting lifetimes have lesser changes when pH values vary. Generally, the lifetime changes in these three proteins are between 100 ps to 300 ps. On the other hand, when arginine and lysine bind with eosin their lifetimes change significantly with pH values. When the pH value changes from 2.06 to 3.96, the lifetime changes of arginine and lysine are 546 ps and 976 ps, respectively. As the pH value increases from 2.06 to 6, BSA, histidine and tryptophan exhibit an increasing trend in lifetime values and then decrease when pH increases from 6 to 8.35.

(a) (b)

Figure 6-4 Protein-dye complex solutions obtained under different pH values (a) pH=2.06 (b) pH=8.35. Dye complex produced from BSA, poly-L-arginine, ploy-L-histidine, poly-L-lysine and poly-L-tryptophan are stored in centrifuge tubes (from left to right) shown in both images.

Table 6-2 Fluorescence lifetime of protein-dye complex solutions with pH varying from 2.06 to 8.35. The proteins include BSA, poly-L-arginine, poly-L-histidine, poly-L-lysine and poly-L-tryptophan. Every lifetime is calculated from an average of three randomly chosen regions on an imaging slide. Error is calculated to be within ±20 ps.

pH	Fluorescence Lifetime (ps)				
	BSA	Arginine	Histidine	Lysine	Tryptophan
2.06	1728	1638	1652	1701	1743
3.96	1856	1093	1716	724	1648
6	1926	1187	1971	784	1929
8.35	1813	1357	1745	1176	1853

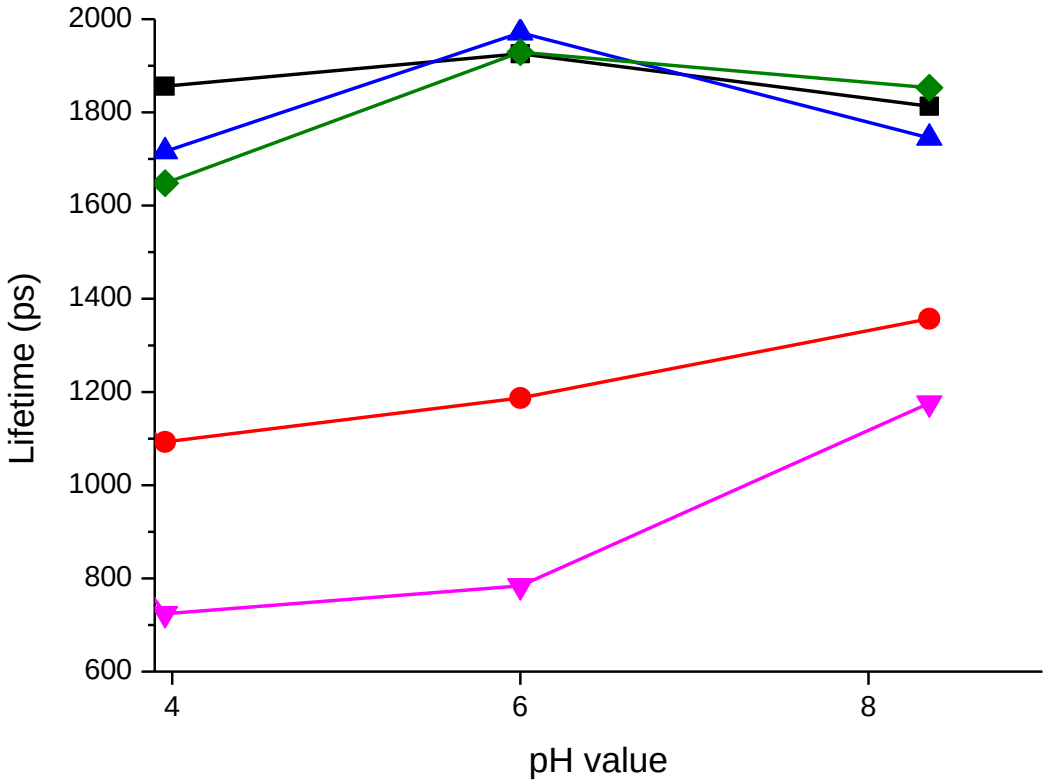

Figure 6-5 Scatter plot of fluorescence lifetime of protein-dye complex solutions with pH varying from 3.96 to 8.35. The proteins include BSA (■), poly-L-arginine (●), poly-L-histidine (▲), poly-L-lysine (▼) and poly-L-tryptophan (◆).

For arginine and lysine, however, the corresponding lifetime values undergo a sharp decrease (up to 1000 ps) when pH increases from 2.06 to 3.96 and then continues to increase as pH increases from 3.96 to 8.35. To better visualize and analyze the lifetime change trend, fluorescence lifetime of protein-dye complex solutions under pH values from 3.96 to 8.35 were plotted in Figure 6-5 for comparison.

6.3.3 Fluorescence Lifetime Values in solutions with added Xylene at Different pH values

Xylene was added to the protein-dye complex solution and the resulting fluorescence

lifetimes for the pH values of 3.96, 6 and 8.35, respectively, were obtained and are listed in Table 6-3 and illustrated in Figure 6-6. It can be seen that, the protein-dye complex lifetimes change significantly for all proteins except poly-L-arginine, which has only a slight decrease of ~100 ps as compared to the case where xylene was not added. For poly-L-histidine, poly-L-lysine and poly-L-tryptophan, an average of ~500 ps decrease in lifetime was observed when xylene was added. The trend of lifetime change against pH value can clearly be seen in Figure 6-6. As pH increases from 3.96 to 8.35, the lifetimes of poly-L-histidine and poly-L-tryptophan complexes with added xylene have only a slight decreasing trend whereas that of poly-L-lysine has a much stronger, and apparently nonlinear decrease. For poly-L-arginine, the lifetime seems to be nonlinear as well, with an apparent local minimum in the middle of the pH range.

Table 6-3 Fluorescence lifetimes of xylene added protein-dye complex solutions with pH varying from 3.96 to 8.35. The proteins include poly-L-arginine, poly-L-histidine, poly-L-lysine and poly-L-tryptophan. Every lifetime is calculated from an average of three randomly chosen regions on an imaging slide. Error is within ±20 ps.

pH	Fluorescence Lifetime (ps)			
	Arginine	Histidine	Lysine	Tryptophan
3.96	1093	1240	1138	1193
6	1002	1198	624	1206
8.35	1271	1112	531	1101

6.3.4 Discussion

To investigate the effect of pH and environment solvent to the lifetimes of protein-dye complex, five proteins including BSA, poly-L-arginine, poly-L-histidine, poly-L-lysine and poly-L-tryptophan were used to bind with the eosin Y dye. To ensure that lifetime only originates from the protein-dye complex, the amount of protein added should ideally reach a saturation point because of the electrostatic binding properties of protein and eosin Y [163]. However, due to the limited amount of proteins available in our experimental solution, no saturation point was achieved.

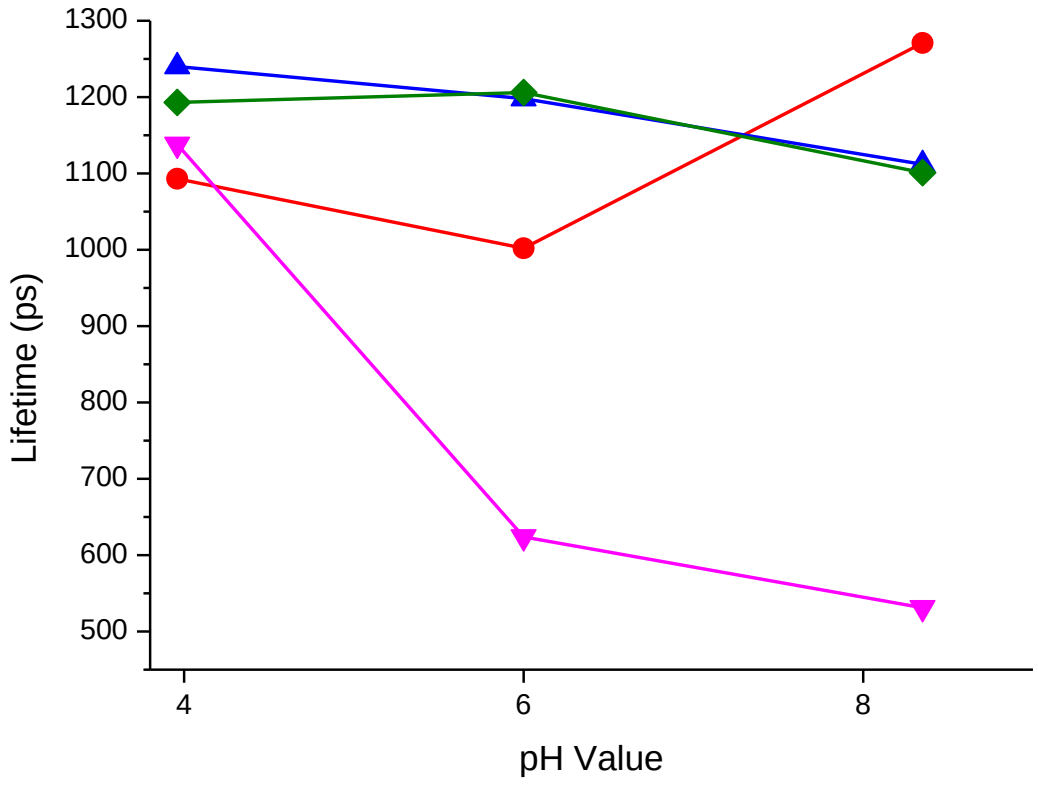

Figure 6-6 Scatter plot of fluorescence lifetimes of xylene-added protein-dye complex solutions with pH varying from 2.06 to 8.35. The proteins include poly-L-arginine (●), poly-L-histidine (▲), poly-L-lysine (▼) and poly-L-tryptophan (◆).

To overcome this problem, the absorbance of each dye-protein complex against protein volume curve was measured and the protein amount was capped at 400 μg (400-μl solution with a concentration of 1 mg/ml). According to the absorbance curve, the absorbance for the 5 protein-dye complexes was randomly selected to be 1 and the corresponding protein amount was calculated for solution preparations. At a pH of 2.06, eosin Y did not produce any fluorescence and a single exponential model was found to best fit the emission fluorescence decay curve. Therefore, at pH=2.06, only the fluorescence lifetime is from the protein-dye complex is measured. At other pH values of 3.96, 6 and 8.35, the same amount of proteins were used for protein-dye complex formation. Since the binding coefficients increase with the pH [163], it is likely that eosin Y would be fully bound by proteins at large pH values, and as a result there might be protein surplus in the final solution. It is also possible that eosin Y is not fully consumed and there is eosin Y residue since the saturation point is unknown in our experiment. Interestingly, a single exponential model was found to give a best fit of the decay curve while a bi-exponential model produce a much poorer fitting result.

Proteins generally absorb in the UV region and fluoresce in the range 300-425 nm [165]. Since the observed fluorescence was in the wavelength range of 500-550 nm, surplus protein could not have contributed to the measured lifetime.

The lifetime values of eosin Y were measured to be 1848 ps, 2010 ps and 1809 ps at pH values of 3.96, 6 and 8.35, respectively. These values are largely different from the lifetime values obtained for poly-L-arginine and ploy-L-lysine, which suggests that the protein-dye complex is the major contributing fluorophore to the measured lifetime and no surplus of eosin Y is present. For BSA, poly-L-histidine and poly-L-tryptophan, the

eosin Y lifetime among various pH values is similar to the protein-complex solution lifetime, indicating that the possibility of lifetime contribution from eosin Y could not be eliminated.

The absorbance spectrum of the poly-L-tryptophan and eosin Y complex shows a constant absorbance value regardless of the increase in poly-L-tryptophan amount. This is because the saturation point for eosin Y occurs when less than 50 µl poly-L-tryptophan was added [163].

It has been concluded from the previous chapters that the eosin lifetime could be used to diagnose H&E stained cervical tissue sections and LBC cells. As the disease stage progresses from normal to higher grades of dysplasia, the lifetime component τ_2 decreases in tissue sections and increases in LBC cells. The effect of environmental pH value, which is one of the key parameters that affect fluorescence lifetime [25, 166-168] of fluorophores, was investigated in the biochemical mechanism study. Since eosin was found to bind with the intracellular proteins in the cytoplasm of cervical cells, 5 common proteins comprising BSA, poly-L-arginine, poly-L-histidine, poly-L-lysine and poly-L-tryptophan were used to simulate the bindings in the cellular cytoplasm involved during the H&E staining protocol. Protein-dye complexes of the five proteins were formed and the corresponding fluorescence lifetimes were measured. According to the obtained lifetime values, the lifetimes of poly-L-arginine and poly-L-lysine decreased as pH values decreased from 8.35 to 3.96. This could explain the decreasing trend of τ_2 obtained from H&E stained cervical tissue sections. As tissue becomes more neoplastic, both the intracellular and extracellular components become more acidic [158]. The lowering pH value accompanied with more acidity in turn causes the reduction in

protein-dye complex lifetime. The pH range from 8.35 to 3.96 selected in this study is well consistent with cellular pH values as they transit from normal to neoplastic [158]. However, sufficiently low pH values could lead to cell death [169, 170], and therefore the discussion on biochemical mechanism did not consider lifetimes values measured at pH=2 .

In the preparation of H&E stained cervical tissue sections and LBC slides, xylene is one of the few chemicals involved in LBC slides processing but not involved in tissue sections for the samples collected from KKH. Besides the pH, other environmental factors may play an important role in influencing the lifetime of an excited fluorophore [160, 161]. Therefore, xylene was added into the protein-dye complex solution and lifetimes under different pH values were measured and compared. It was found that as pH decreases from 8.35 to 3.96, the lifetimes of poly-L-histidine and poly-L-lysine increased. These two proteins could explain the lifetime increase in H&E stained LBC cells.

To conclude, poly-L-lysine and poly-L-arginine show a decrease in lifetime as pH changes from 8.35 to 3.96. Poly-L-histidine and poly-L-lysine exhibit an increase in lifetime when xylene was added to solvent. Since polyamino acids are major proteins in cervical cell cytoplasm [171, 172], lifetime derived from eosin Y and polyamino acids bound complexes could be used to explain different trend in lifetime diagnosis of cervical tissue sections and LBC cells.

6.4 Summary

Fluorescence lifetimes of protein-dye complex solutions under different pH values and different solvents were measured. Five proteins, namely BSA, poly-L-arginine, poly-L-histidine, poly-L-lysine, poly-L-tryptophan, were used together with and eosin Y dye to form different protein-dye complexes. The pH values of the solutions were adjusted by adding HCL and NaOH, and the environmental solvent was changed by adding xylene. It was found that as pH value decreased from 8.35 to 3.96, poly-L-arginine and poly-L-lysine-dye complex exhibited a decreasing trend in lifetimes when xylene was not added to solvent. Lifetimes from poly-L-histidine and poly-L-lysine show an increasing trend when xylene was added. The results obtained are in good agreement with the lifetime shortening observed in H&E stained tissue sections and the lifetime lengthening found in LBC cells.

Chapter 7. CONCLUSION AND RECOMMENDATIONS

7.1 Conclusion

Fluorescence lifetime imaging was used to characterize H&E stained cervical tissue sections. More than 100 H&E stained cervical samples including categories of normal, cervical intraepithelial neoplasia (CIN1, CIN2, CIN3), squamous cell carcinoma (SCC) and microinvasive carcinoma were collected, imaged and analyzed. Epithelial regions were specifically investigated because most cervical cancers originate from the epithelium. The decay of emission fluorescence was fitted with a bi-exponential model and the longer lifetime component τ_2 was found to correlate with tissue pathology. Mean and standard deviation values of the lifetime τ_2 from the epithelium were used as feature vectors to feed into a neural network extreme learning machine (ELM) classifier for discrimination. An averaged sensitivity and specificity of 92.8% and 80.2%, respectively, were achieved when differentiating normal from precancerous (CIN1, CIN2, CIN3) samples. Discriminations between low-risk group (normal, CIN1) and high-risk group (CIN2, CIN3) were also conducted due to the clinical importance for treatment and a sensitivity of 85.0% and specificity of 87.6% were obtained. The results suggest that the proposed fluorescence lifetime imaging of H&E stained cervical tissue sections with the quantitative neural network ELM could be used to aid and supplement the traditional histopathological examinations.

The diagnosis of H&E stained cervical tissue sections using fluorescence lifetime imaging was further investigated using epithelial layer analysis. Cervical epithelium

regions were divided into 10 even layers in the tissue growth direction and diagnostic value in every of the 10 divided layers was investigated. It was found that feature vectors including a combination of mean τ_2 from the top-half epithelium (layers 6 to 10) gave the maximum diagnostic accuracy while the standard deviation of τ_2 does not carry any useful diagnostic information. Neural network ELM classifier was used for discrimination and an averaged sensitivity of 94.6% and specificity of 84.3% were obtained when differentiating normal from precancerous cervical tissues. The proposed layer analysis technique has the advantage of achieving a concurrently higher sensitivity and specificity. In addition, analyzing only the top-half of the cervical epithelium is computationally fast with significantly reduced lifetime calculations as redundant feature components were eliminated. The proposed method can provide more accurate and faster cervical diagnosis, which can better supplement traditional gold standard histopathological examination.

Fluorescence lifetime imaging was applied to study cells isolated in H&E stained liquid based cytological (LBC) Papanicolaou smear samples. The resulting lifetime images were processed to extract the whole cell and cytoplasmic regions for analysis. The results show that the whole cell lifetime distribution is highly similar to the lifetime distribution of the cytoplasmic region. The mean lifetime component τ_2 in the whole cell region was used to differentiate between normal and precancerous cells. A concurrently high sensitivity and specificity of 92.6% and 71.2% were achieved, respectively. This preliminary study suggests that the proposed method could supplement and improve the automated screening of cervical LBC samples.

Biochemical mechanisms were studied to investigate the correlation between lifetime

changes and the associated cervical pathological states. Five proteins, namely BSA, poly-L-arginine, poly-L-histidine, poly-L-lysine and poly-L-tryptophan, were used to simulate the proteins in cervical cytoplasm. Eosin Y, which is the only fluorophore involved in H&E staining, was used to bind with those proteins. Fluorescence lifetimes from those bound protein-dye complexes were measured and compared. It was found that lifetime varied with the solution pH value and environment solvent. The results obtained could explain the lifetime shortening trend in H&E stained cervical tissue sections and the lifetime lengthening behavior in LBC cells.

7.2 Recommendations for Future Work

1. **Fluorescence lifetime characterization of preinvasive H&E stained cervical tissue stroma**

Fluorescence lifetime has been used to characterize cervical precancer in H&E stained tissue sections. Invasive cervical carcinoma [173] is easily identified since it is often present with symptoms such as postcoital bleed, vaginal discharge or lower abdominal pain. However, the preinvasive cervical cancer is not easily found because it does not generate obvious clinical features and symptoms [174]. At different stages of preinvasive cervical cancer, the neoplastic cells invade different thicknesses into the cervical stroma under the epithelium. Therefore, fluorescence lifetime imaging could be used to investigate the biochemical changes involved in stroma regions of H&E stained cervical tissues.

2. **Combination of morphological features and biochemical information to diagnose cervical LBC smears**

Fluorescence lifetime diagnosis of H&E stained LBC smears have been demonstrated to be effective in supplementing the automated screening with higher accuracy. Morphological features such as nuclear size, nuclear shape, cytoplasmic area and nuclear/cytoplasmic ratio have been applied in the image processing involved in automated LBC screening [141-145]. The combination of morphological features and biochemical features could potentially improve the diagnostic accuracy since more relevant features could improve classification result [175].

3. **Advanced epithelium division method for the layer analysis of cervical fluorescence lifetime images**

Layer analysis was conducted on H&E stained cervical tissue sections with regular layered structure in the epithelium. However, irregular structures might be present due to the variation in tissue growth and sampling protocol. Therefore, new image processing techniques, which can divide cervical epithelium with irregular structures into even layers, can be explored.

4. **Development of compact and integrated FLIM diagnostic system**

Laboratory FLIM system has been demonstrated to diagnose cervical early cancer with high sensitivity and specificity in our preliminary study. It implies great potential to be developed into a compact and integrated commercial product for automated cervical slide screening. Now with the understanding of eosin lifetime, some portable and cheap lasers such as laser diodes and LEDs with 50 ps to 200 ps could be used as light source in FLIM system. This cheap and automated screening modalities could be replicated and promoted in developing countries where specially trained personnel are not available.

AUTHOR'S PUBLICATIONS

1 **Gu J**, Fu CY, Ng BK, Gulam Razul S, Lim SK., Quantitative Diagnosis of Cervical Neoplasia Using Fluorescence Lifetime Imaging on Haematoxylin and Eosin Stained Tissue Sections, J Biophotonics, 2012, IMF=3.1

2 **Gu Jun**, Ng Beng Koon, Fu Chit Yaw, Razul, S.G., Lim Soo Kim, Fluorescence Lifetime Diagnosis of Cervical Cancer based on Extreme Learning Machine, Photonic Global Conference, 2010 Dec

3 **Gu Jun**, Ng Beng Koon, Fu Chit Yaw, Razul, S.G., Lim Soo Kim, Quantitative Diagnosis of Cervical Precancer Using Fluorescence Intensity and Lifetime Imaging from the Stroma, Photonic Global Conference, 2012 Dec

4 **Jun GU**, Chit Yaw Fu, Beng Koon NG, LinBo LIU, Soo Kim LIM, Caroline GL LEE, Enhancement of early cervical cancer diagnosis with epithelial layer analysis of fluorescence lifetime images'. Plos One, March 2015, IMF=3.7

5 Cui DongYao, Yu Xiaojun, **Gu Jun**, Ding Sun, Luo Yue Mei, Liu Linbo, In vivo 1-micron resolution optical coherence tomography using NIR continuous wave sources. Accepted with Minor Revision, Optical Letter, IMF=3.385

6 Ebrahim, Wu Bing, **Gu Jun**, gravity-driven membrane filtration as Pretreatment for Seawater Reverse Osmosis: Linking biofilm Morphology and Community with Flux'. In preparation to submit to Journal of Desalination, IMF=3.17

7 Xiaojun Yu, Xinyu Liu, **Gu Jun**, Junying Wu, Liu Linbo, Depth Extension and Sidelobe Suppression in Optical Coherence Tomography using Pupil Filters, Submitted to Optical Express August 2014, IMF=3.55

8 Xinyu Liu, Xiaojun Yu, Hongying Tang, Dongyao Cui, Meghna R. Beotra, Michael J. A. Girard, Ding Sun, **Jun Gu**, and Linbo Liu, Spectrally Extended Source Optical Coherence Tomography, Submitted to Optical Letter September 2014, IMF=3.385

REFERENCES

[1] D. M. Parkin, F. Bray, J. Ferlay, and P. Pisani, "Estimating the world cancer burden: Globocan 2000," *International journal of cancer,* vol. 94, pp. 153-156, 2001.

[2] R. A. Drezek, R. Richards‐Kortum, M. A. Brewer, M. S. Feld, C. Pitris, A. Ferenczy, *et al.*, "Optical imaging of the cervix," *Cancer,* vol. 98, pp. 2015-2027, 2003.

[3] T. E. Rohan and K. V. Shah, "Cercival Cancer: From Etiology to Prevention," 2004.

[4] R. G. Pretorius, Y. P. Bao, J. L. Belinson, R. J. Burchette, J. S. Smith, and Y. L. Qiao, "Inappropriate gold standard bias in cervical cancer screening studies," *International Journal of Cancer,* vol. 121, pp. 2218-2224, 2007.

[5] Y. N. Mirabal, S. K. Chang, E. N. Atkinson, A. Malpica, M. Follen, and R. Richards-Kortum, "Reflectance spectroscopy for in vivo detection of cervical precancer," *Journal of biomedical optics,* vol. 7, pp. 587-594, 2002.

[6] T. Denk çeken, T. Simsek, G. Erdogan, E. Pestereli, S. Karaveli, D. Ozel, *et al.*, "Elastic light single-scattering spectroscopy for the detection of cervical precancerous ex vivo," *Biomedical Engineering, IEEE Transactions on,* vol. 60, pp. 123-127, 2013.

[7] K. Suhling, P. M. French, and D. Phillips, "Time-resolved fluorescence microscopy," *Photochemical & Photobiological Sciences,* vol. 4, pp. 13-22, 2005.

[8] J. R. Lakowicz and C. D. Geddes, *Topics in fluorescence spectroscopy* vol. 1: Springer, 1991.

[9] A. Pradhan, P. Pal, G. Durocher, L. Villeneuve, A. Balassy, F. Babai, *et al.*, "Steady state and time-resolved fluorescence properties of metastatic and non-metastatic malignant cells from different species," *Journal of Photochemistry and Photobiology B: Biology,* vol. 31, pp. 101-112, 1995.

[10] W. Lohmann, J. Muβmann, C. Lohmann, and W. Künzel, "Native fluorescence of the cervix uteri as a marker for dysplasia and invasive carcinoma," *European Journal of Obstetrics & Gynecology and Reproductive Biology,* vol. 31, pp. 249-253, 1989.

[11] S. Andersson-Engels, C. af Klinteberg, K. Svanberg, and S. Svanberg, "In vivo fluorescence imaging for tissue diagnostics," *Physics in medicine and biology,* vol. 42, p. 815, 1997.

[12] L. Marcu, "Fluorescence lifetime techniques in medical applications," *Annals of biomedical engineering,* vol. 40, pp. 304-331, 2012.

[13] J. R. Lakowicz, *Principles of fluorescence spectroscopy*: Springer, 2007.

[14] D. A. Skoog, F. J. Holler, and T. A. Nieman, *Principles of Instrumental Analysis*: Harcourt Brace Collge Publishers, 1998.

[15] R. P. Haugland, *Handbook of Fluorescent Probes and Research Products*, ninth ed.: Molecular Probes, Inc.

[16] D. Rendell, *Fluorescence and Phosphorescence Spectroscopy*. New York: John Wiley & Sons, 1987.

[17] P. T. So, C. Y. Dong, B. R. Masters, and K. M. Berland, "Two-photon excitation fluorescence microscopy," *Annual review of biomedical engineering*, vol. 2, pp. 399-429, 2000.
[18] W. Kaiser and C. Garrett, "Two-Photon Excitation in Ca F 2: Eu 2+," *Physical review letters*, vol. 7, p. 229, 1961.
[19] C. V. Santi Nonell, *Basic Spectroscopy*, Available at http://www.photobiology.info/Nonell_Viappiani.html.
[20] M. Y. Berezin and S. Achilefu, "Fluorescence lifetime measurements and biological imaging," *Chemical reviews*, vol. 110, pp. 2641-2684, 2010.
[21] Y. Chen and A. Periasamy, "Characterization of two ‐ photon excitation fluorescence lifetime imaging microscopy for protein localization," *Microscopy research and technique*, vol. 63, pp. 72-80, 2004.
[22] W. Inami, N. H. Viet, A. Miyakawa, and Y. Kawata, "Intracellular Calcium Ion Concentration Measurement Using a Phase-modulation Fluorescence Lifetime Method with Compensation for Phase Shift due to the Presence of Proteins," *Analytical Sciences*, vol. 29, pp. 199-203, 2013.
[23] M. K. Kuimova, G. Yahioglu, J. A. Levitt, and K. Suhling, "Molecular rotor measures viscosity of live cells via fluorescence lifetime imaging," *Journal of the American Chemical Society*, vol. 130, pp. 6672-6673, 2008.
[24] C. Tregidgo, J. A. Levitt, and K. Suhling, "Effect of refractive index on the fluorescence lifetime of green fluorescent protein," *Journal of biomedical optics*, vol. 13, pp. 031218-031218-8, 2008.
[25] R. Sanders, A. Draaijer, H. C. Gerritsen, P. M. Houpt, and Y. K. Levine, "Quantitative pH imaging in cells using confocal fluorescence lifetime imaging microscopy," *Analytical biochemistry*, vol. 227, pp. 302-308, 1995.
[26] J.-P. Knemeyer, D.-P. Herten, and M. Sauer, "Detection and identification of single molecules in living cells using spectrally resolved fluorescence lifetime imaging microscopy," *Analytical chemistry*, vol. 75, pp. 2147-2153, 2003.
[27] M. J. Cole, J. Siegel, S. E. D. Webb, R. Jones, K. Dowling, P. M. W. French, *et al.*, "Whole-field optically sectioned fluorescence lifetime imaging," *Optics Letters*, vol. 25, pp. 1361-1363, 2000.
[28] K. Dowling, S. C. W. Hyde, J. C. Dainty, P. M. W. French, and J. D. Hares, "2-D fluorescence lifetime imaging using a time-gated image intensifier," *Optics Communications*, vol. 135, pp. 27-31, 1997.
[29] J. R. Alcala, E. Gratton, and D. M. Jameson, "A multifrequency phase fluorometer using the harmonic content of a mode-locked laser," *Analytical Instrumentation*, vol. 14, pp. 225-250, 1985.
[30] J. R. Lakowicz and B. Maliwal, "Optical sensing of glucose using phase-modulation fluorimetry," *Analytica Chimica Acta*, vol. 271, pp. 155-164, 1993.
[31] R. Cubeddu, D. Comelli, C. D'Andrea, P. Taroni, and G. Valentini, "Time-resolved fluorescence imaging in biology and medicine," *Journal of Physics D: Applied Physics*, vol. 35, pp. R61-R76, 2002.
[32] O'Connor and Phillips, *Time-correlated single photon counting*. New York: Acadeic Press, 1984.
[33] H. Szmacinski and Q. Chang, "Micro- and sub-nanosecond lifetime measurements using a UV light-emitting diode," *Applied Spectroscopy*, vol. 54, pp. 106-109, 2000.

[34] E. Gratton, S. Breusegem, J. Sutin, Q. Ruan, and N. Barry, "Fluorescence lifetime imaging for the two-photon microscope: Time-domain and frequency-domain methods," *Journal of Biomedical Optics,* vol. 8, pp. 381-390, 2003.
[35] V. V. Tuchin, *Handbook of photonics for biomedical science*: CRC Press, 2010.
[36] G. A. Morton, "Photon Counting," *Appl. Opt.,* vol. 7, pp. 1-10, 1968.
[37] M. Wahl, "Time-Correlated Single Photon Counting," *Technical Note*.
[38] P. Pisani, D. M. Parkin, F. Bray, and J. Ferlay, "Estimates of the worldwide mortality from 25 cancers in 1990," *International journal of cancer,* vol. 83, pp. 18-29, 1999.
[39] V. Kumar, A. Abbas, N. Fausto, and R. N. Mitchell, "Robbins Basic Pathology (2007)," *Saunders Elsevier,* pp. 516-22.
[40] T. E.Rohan and K. V.Shah, *Cervical Cancer: From Etiology to Prevention*: Kluwer Academic Publishers, 2003.
[41] R. M. RICHART, "Natural history of cervical intraepithelial neoplasia," *Clinical Obstetrics and Gynecology,* vol. 10, pp. 748-784, 1967.
[42] W. Gray and G. Kocjan, *Diagnostic cytopathology*: Elsevier Health Sciences, 2010.
[43] R. Dunleavey, *Cervical cancer: a guide for nurses*: John Wiley & Sons, 2008.
[44] K. Kurian and A. Al-Nafussi, "Relation of cervical glandular intraepithelial neoplasia to microinvasive and invasive adenocarcinoma of the uterine cervix: a study of 121 cases," *Journal of clinical pathology,* vol. 52, pp. 112-117, 1999.
[45] M. E. Boon, J. Baak, P. Kurver, S. Overdiep, and G. Verdonk, "Adenocarcinoma in situ of the cervix: an underdiagnosed lesion," *Cancer,* vol. 48, pp. 768-773, 1981.
[46] E. Gloor and J. Ruzicka, "Morphology of adenocarcinoma in situ of the uterine cervix: a study of 14 cases," *Cancer,* vol. 49, pp. 294-302, 1982.
[47] J. L. H. Evers and M. J. Heineman, *Gynecology: A Clinical Atlas*: Mosby, 1990.
[48] N. C. S. Programmes, "Histopathology Reporting in Cervical Screening-An Integrated Approach," 2012.
[49] V. A. Moyer, "Screening for cervical cancer: US Preventive Services Task Force recommendation statement," *Annals of internal medicine,* vol. 156, pp. 880-891, 2012.
[50] J. Karnon, J. Peters, J. Platt, J. Chilcott, E. McGoogan, and N. Brewer, "Liquid-based cytology in cervical screening: an updated rapid and systematic review and economic analysis," 2004.
[51] A. B. Miller and W. H. Organization, "Cervical cancer screening programmes: managerial guidelines/AB Miller," 1992.
[52] L. Denny, L. Kuhn, A. Pollack, H. Wainwright, and T. C. Wright, "Evaluation of alternative methods of cervical cancer screening for resource‐poor settings," *Cancer,* vol. 89, pp. 826-833, 2000.
[53] D. M. Chase, M. Kalouyan, and P. J. DiSaia, "Colposcopy to evaluate abnormal cervical cytology in 2008," *American journal of obstetrics and gynecology,* vol. 200, pp. 472-480, 2009.
[54] L. Wang, S. L. Jacques, and L. Zheng, "MCML—Monte Carlo modeling of light transport in multi-layered tissues," *Computer methods and programs in biomedicine,* vol. 47, pp. 131-146, 1995.
[55] P. N. Prasad, *Introduction to biophotonics*: John Wiley & Sons, 2004.
[56] D. Arifler, C. MacAulay, M. Follen, and R. Richards-Kortum, "Spatially resolved reflectance spectroscopy for diagnosis of cervical precancer: Monte

Carlo modeling and comparison to clinical measurements," *Journal of biomedical optics*, vol. 11, pp. 064027-064027-16, 2006.
[57] S. C. Chu and H. K. Chiang, "Monte Carlo simulation of fluorescence spectra of normal and dysplastic cervical tissues for optimizing excitation/receiving arrangements," *Applied spectroscopy*, vol. 64, pp. 708-713, 2010.
[58] D. E. Goldberg, *Genetic algorithms in search, optimization, and machine learning* vol. 412: Addison-wesley Reading Menlo Park, 1989.
[59] C. M. Bishop, *Pattern recognition and machine learning* vol. 1: springer New York, 2006.
[60] J. R. Anderson, R. S. Michalski, R. S. Michalski, J. G. Carbonell, and T. M. Mitchell, *Machine learning: An artificial intelligence approach* vol. 2: Morgan Kaufmann, 1986.
[61] D. Kleinbaum, L. Kupper, A. Nizam, and E. Rosenberg, *Applied regression analysis and other multivariable methods*: Cengage Learning, 2013.
[62] D. Michie, D. J. Spiegelhalter, and C. C. Taylor, "Machine learning, neural and statistical classification," 1994.
[63] B. Yegnanarayana, *Artificial neural networks*: PHI Learning Pvt. Ltd., 2009.
[64] G. Huang, S. Song, J. N. Gupta, and C. Wu, "Semi-supervised and unsupervised extreme learning machines," 2014.
[65] G.-B. Huang, X. Ding, and H. Zhou, "Optimization method based extreme learning machine for classification," *Neurocomputing*, vol. 74, pp. 155-163, 2010.
[66] G.-B. Huang, Q.-Y. Zhu, and C.-K. Siew, "Extreme learning machine: theory and applications," *Neurocomputing*, vol. 70, pp. 489-501, 2006.
[67] G.-B. Huang, Q.-Y. Zhu, and C.-K. Siew, "Extreme learning machine: a new learning scheme of feedforward neural networks," in *Neural Networks, 2004. Proceedings. 2004 IEEE International Joint Conference on*, 2004, pp. 985-990.
[68] F. Scarselli and A. C. Tsoi, "Universal approximation using feedforward neural networks: A survey of some existing methods, and some new results," *Neural networks*, vol. 11, pp. 15-37, 1998.
[69] G.-B. Huang and L. Chen, "Convex incremental extreme learning machine," *Neurocomputing*, vol. 70, pp. 3056-3062, 2007.
[70] G.-B. Huang and L. Chen, "Enhanced random search based incremental extreme learning machine," *Neurocomputing*, vol. 71, pp. 3460-3468, 2008.
[71] C. Cortes and V. Vapnik, "Support-vector networks," *Machine learning*, vol. 20, pp. 273-297, 1995.
[72] G.-B. Huang, L. Chen, and C.-K. Siew, "Universal approximation using incremental constructive feedforward networks with random hidden nodes," *Neural Networks, IEEE Transactions on*, vol. 17, pp. 879-892, 2006.
[73] C. R. Rao and S. K. Mitra, *Generalized inverse of matrices and its applications* vol. 7: Wiley New York, 1971.
[74] D. Serre, "Matrices. Theory and Applications, translated from the 2001 French original," *Grad. Texts in Math*, vol. 216.
[75] C. Ma, J. Ouyang, H.-L. Chen, and X.-H. Zhao, "An Efficient Diagnosis System for Parkinson's Disease Using Kernel-Based Extreme Learning Machine with Subtractive Clustering Features Weighting Approach," *Computational and mathematical methods in medicine*, vol. 2014, 2014.
[76] C. W. Boone, J. W. Bacus, J. V. Bacus, V. E. Steele, and G. J. Kelloff, "Properties of intraepithelial neoplasia relevant to the development of cancer

chemopreventive agents," *Journal of Cellular Biochemistry,* vol. 67, pp. 1-20, 1997.

[77] G. I. Evan and K. H. Vousden, "Proliferation, cell cycle and apoptosis in cancer," *Nature,* vol. 411, pp. 342-348, 2001.

[78] D. G. Ferris, R. A. Lawhead, E. D. Dickman, N. Holtzapple, J. A. Miller, S. Grogan, *et al.*, "Multimodal hyperspectral imaging for the noninvasive diagnosis of cervical neoplasia," *Journal of Lower Genital Tract Disease,* vol. 5, pp. 65-72, 2001.

[79] N. Thekkek and R. Richards-Kortum, "Optical imaging for cervical cancer detection: solutions for a continuing global problem," *Nature Reviews Cancer,* vol. 8, pp. 725-731, 2008.

[80] W. Li, V. Van Raad, J. Gu, U. Hansson, J. Hakansson, H. Lange, *et al.*, "Computer-aided Diagnosis (CAD) for cervical cancer screening and diagnosis: a new system design in medical image processing," in *Computer Vision for Biomedical Image Applications*, ed: Springer, 2005, pp. 240-250.

[81] S. Y. Park, M. Follen, A. Milbourne, A. Malpica, N. MacKinnon, M. K. Markey, *et al.*, "Automated image analysis of digital colposcopy for the detection of cervical neoplasia," *Journal of biomedical optics,* vol. 13, pp. 014029-014029-10, 2008.

[82] K. L. Blair, "Apparatus and method for digital photography useful in cervical cancer detection," ed: Google Patents, 1999.

[83] K. W. Eliceiri, G. E. Lyons, J. G. White, and C.-H. Fan, "Analysis of histology specimens using lifetime multiphoton microscopy," *Journal of biomedical optics,* vol. 8, pp. 376-380, 2003.

[84] D. J. Hawrysz and E. M. Sevick-Muraca, "Developments toward diagnostic breast cancer imaging using near-infrared optical measurements and fluorescent contrast agents," *Neoplasia (New York, NY),* vol. 2, p. 388, 2000.

[85] N. Ramanujam, M. F. Mitchell, A. Mahadevan, S. Thomsen, E. Silva, and R. Richards-Kortum, "Fluorescence spectroscopy: a diagnostic tool for cervical intraepithelial neoplasia (CIN)," *Gynecologic Oncology,* vol. 52, pp. 31-38, 1994.

[86] J. H. Tan and C. D. H. Wrede, "New technologies and advances in colposcopic assessment," *Best Practice & Research Clinical Obstetrics & Gynaecology,* vol. 25, pp. 667-677, 2011.

[87] P. Hillemanns, H. Weingandt, R. Baumgartner, J. Diebold, W. Xiang, and H. Stepp, "Photodetection of cervical intraepithelial neoplasia using 5 ‐ aminolevulinic acid ‐ induced porphyrin fluorescence," *Cancer,* vol. 88, pp. 2275-2282, 2000.

[88] K. Licha and C. Olbrich, "Optical imaging in drug discovery and diagnostic applications," *Advanced drug delivery reviews,* vol. 57, pp. 1087-1108, 2005.

[89] N. Galletly, J. McGinty, C. Dunsby, F. Teixeira, J. Requejo ‐ Isidro, I. Munro, *et al.*, "Fluorescence lifetime imaging distinguishes basal cell carcinoma from surrounding uninvolved skin," *British Journal of Dermatology,* vol. 159, pp. 152-161, 2008.

[90] P. J. Tadrous, J. Siegel, P. M. French, S. Shousha, E. N. Lalani, and G. W. Stamp, "Fluorescence lifetime imaging of unstained tissues: early results in human breast cancer," *The Journal of pathology,* vol. 199, pp. 309-317, 2003.

[91] D. Schweitzer, A. Kolb, and M. Hammer, "Autofluorescence lifetime measurements in images of the human ocular fundus," in *European Conference on Biomedical Optics*, 2001, pp. 29-39.
[92] E. Dimitrow, I. Riemann, A. Ehlers, M. J. Koehler, J. Norgauer, P. Elsner, *et al.*, "Spectral fluorescence lifetime detection and selective melanin imaging by multiphoton laser tomography for melanoma diagnosis," *Experimental dermatology,* vol. 18, pp. 509-515, 2009.
[93] American National Standard for the Safe Use of Lasers and A.-Z. 136.1, "American National Standard Institute,
New York," 1993.
[94] C. T. Kelley, *Iterative methods for optimization* vol. 18: Siam, 1999.
[95] M. I. Rowley, P. R. Barber, A. C. Coolen, and B. Vojnovic, "Bayesian analysis of fluorescence lifetime imaging data," in *SPIE BiOS*, 2011, pp. 790325-790325-12.
[96] P. Barber, S. Ameer-Beg, S. Pathmananthan, M. Rowley, and A. Coolen, "A Bayesian method for single molecule, fluorescence burst analysis," *Biomedical optics express*, vol. 1, pp. 1148-1158, 2010.
[97] C. Y. Fu, S. G. Razul, and B. K. Ng, "Fluorescence lifetime discrimination using expectation-maximization algorithm with joint deconvolution," *Journal of biomedical optics*, vol. 14, pp. 064009-064009-10, 2009.
[98] H. F. de Carvalho and S. R. Taboga, "Fluorescence and confocal laser scanning microscopy imaging of elastic fibers in hematoxylin-eosin stained sections," *Histochemistry and cell biology*, vol. 106, pp. 587-592, 1996.
[99] Y. S. Heo and H. J. Song, "Characterizing cutaneous elastic fibers by eosin fluorescence detected by fluorescence microscopy," *Annals of dermatology*, vol. 23, pp. 44-52, 2011.
[100] J. Jakubovský, L. Guller, M. Černá, K. Balážová, Š. Polák, V. Jakubovská, *et al.*, "Fluorescence of hematoxylin and eosin-stained histological sections of the human spleen," *Acta histochemica,* vol. 104, pp. 353-356, 2002.
[101] M. W. Conklin, P. P. Provenzano, K. W. Eliceiri, R. Sullivan, and P. J. Keely, "Fluorescence lifetime imaging of endogenous fluorophores in histopathology sections reveals differences between normal and tumor epithelium in carcinoma in situ of the breast," *Cell biochemistry and biophysics,* vol. 53, pp. 145-157, 2009.
[102] L. Fausett, *Fundamentals of neural networks: architectures, algorithms, and applications*: Prentice-Hall, Inc., 1994.
[103] F. X. Bosch, A. N. Burchell, M. Schiffman, A. R. Giuliano, S. de Sanjose, L. Bruni, *et al.*, "Epidemiology and natural history of human papillomavirus infections and type-specific implications in cervical neoplasia," *Vaccine*, vol. 26, pp. K1-K16, 2008.
[104] B. H. GmbH, "Application note of Non-Descanned FLIM Detection in Multiphoton Microscopes."
[105] W. Becker, *Advanced time-correlated single photon counting techniques* vol. 81: Springer, 2005.
[106] C.-P. Chen, P.-J. Wu, S.-Y. Liou, and Y.-H. Chan, "Ultrabright benzoselenadiazole-based semiconducting polymer dots for specific cellular imaging," *RSC Advances*, vol. 3, pp. 17507-17514, 2013.
[107] P. Domingos and M. Pazzani, "On the optimality of the simple Bayesian classifier under zero-one loss," *Machine learning*, vol. 29, pp. 103-130, 1997.

[108] G.-B. Huang, D. H. Wang, and Y. Lan, "Extreme learning machines: a survey," *International Journal of Machine Learning and Cybernetics,* vol. 2, pp. 107-122, 2011.
[109] R. Parikh, A. Mathai, S. Parikh, G. C. Sekhar, and R. Thomas, "Understanding and using sensitivity, specificity and predictive values," *Indian journal of ophthalmology,* vol. 56, p. 45, 2008.
[110] K. Myers, S. Socrate, D. Tzeranis, and M. House, "Changes in the biochemical constituents and morphologic appearance of the human cervical stroma during pregnancy," *European Journal of Obstetrics & Gynecology and Reproductive Biology,* vol. 144, pp. S82-S89, 2009.
[111] M.-A. Mycek and B. W. Pogue, *Handbook of biomedical fluorescence*: CRC Press, 2003.
[112] G. Fleming, A. W. E. Knight, J. Morris, R. Morrison, and G. Robinson, "Picosecond fluorescence studies of xanthene dyes," *Journal of the American Chemical Society,* vol. 99, pp. 4306-4311, 1977.
[113] S. E. Waggoner, "Cervical cancer," *The Lancet,* vol. 361, pp. 2217-2225, 2003.
[114] J. Gu, C. Y. Fu, B. K. Ng, S. Gulam Razul, and S. K. Lim, "Quantitative diagnosis of cervical neoplasia using fluorescence lifetime imaging on haematoxylin and eosin stained tissue sections," *Journal of biophotonics,* 2013.
[115] B. Young, P. Woodford, and G. O'Dowd, *Wheater's functional histology: a text and colour atlas*: Elsevier Health Sciences, 2013.
[116] V. Popovici, W. Chen, B. G. Gallas, C. Hatzis, W. Shi, F. W. Samuelson, *et al.*, "Effect of training-sample size and classification difficulty on the accuracy of genomic predictors," *Breast Cancer Res,* vol. 12, p. R5, 2010.
[117] R. Abdel-Aal, "GMDH-based feature ranking and selection for improved classification of medical data," *Journal of Biomedical Informatics,* vol. 38, pp. 456-468, 2005.
[118] W. Becker, "The bh TCSPC Handbook, 5th Edition, (Becker & Hickl GmbH)," 2012.
[119] S. Sell, "On the stem cell origin of cancer," *The American journal of pathology,* vol. 176, pp. 2584-2594, 2010.
[120] B. Shambayati, *Cytopathology*: Oxford University Press, 2011.
[121] M. T. Fahey, L. Irwig, and P. Macaskill, "Meta-analysis of Pap test accuracy," *American journal of epidemiology,* vol. 141, pp. 680-689, 1995.
[122] A. N. Kalof and K. Cooper, "Our approach to squamous intraepithelial lesions of the uterine cervix," *Journal of clinical pathology,* vol. 60, pp. 449-455, 2007.
[123] J.-J. Wei, "Pathology of Cervical Carcinoma," *Glob.libr.women's med,* 2009.
[124] M. R. Nucci and E. Oliva, *Gynecologic pathology*: Elsevier Health Sciences, 2009.
[125] R. A. Reichert, *Diagnostic Gynecologic and Obstetric Pathology: An Atlas and Text*: Lippincott Williams & Wilkins, 2012.
[126] J. M. Leiva-Murillo and A. Artés-Rodríguez, "Maximization of mutual information for supervised linear feature extraction," *Neural Networks, IEEE Transactions on,* vol. 18, pp. 1433-1441, 2007.
[127] T. W. Chow and D. Huang, "Estimating optimal feature subsets using efficient estimation of high-dimensional mutual information," *Neural Networks, IEEE Transactions on,* vol. 16, pp. 213-224, 2005.

[128] K. E. Hild, D. Erdogmus, K. Torkkola, and J. C. Principe, "Feature extraction using information-theoretic learning," *Pattern Analysis and Machine Intelligence, IEEE Transactions on,* vol. 28, pp. 1385-1392, 2006.
[129] G. N. Papanicolaou, "A new procedure for staining vaginal smears," *Science,* vol. 95, pp. 438-439, 1942.
[130] A. Fortuño-Mar, "Cytology," in *Skin Cancer*, ed: Springer, 2014, pp. 213-219.
[131] E. Heyderman, "Histotechnology. A self‐instructional text," *Histopathology,* vol. 20, pp. 91-91, 1992.
[132] T. Wright, R. Kurman, and A. Ferenczy, "Blaustein's pathology of the female genital tract," *Blaustein's Pathology of the Female Genital Tract*, 1994.
[133] R. Narayanswamy, J. P. Sharpe, H. J. Duke, R. J. Stewart, and K. M. Johnson, "Morphological feature detection for cervical cancer screening," in *IS&T/SPIE's Symposium on Electronic Imaging: Science & Technology*, 1995, pp. 265-275.
[134] K. Nanda, D. C. McCrory, E. R. Myers, L. A. Bastian, V. Hasselblad, J. D. Hickey, *et al.*, "Accuracy of the Papanicolaou Test in Screening for and Follow-up of Cervical Cytologic AbnormalitiesA Systematic Review," *Annals of internal medicine,* vol. 132, pp. 810-819, 2000.
[135] R. Sankaranarayanan, L. Gaffikin, M. Jacob, J. Sellors, and S. Robles, "A critical assessment of screening methods for cervical neoplasia," *International Journal of Gynecology & Obstetrics,* vol. 89, pp. S4-S12, 2005.
[136] P. J. Klinkhamer, W. J. Meerding, P. F. Rosier, and A. G. Hanselaar, "Liquid‐based cervical cytology," *Cancer Cytopathology,* vol. 99, pp. 263-271, 2003.
[137] A. Ferenczy, J. Robitaille, E. Franco, J. Arseneau, R. M. Richart, and T. C. Wright, "Conventional Cervical Cytologic Smears vs. ThinPrep Smears," *Acta cytologica,* vol. 40, pp. 1136-1142, 1996.
[138] E. Bengtsson and P. Malm, "Screening for Cervical Cancer Using Automated Analysis of PAP-Smears," *Computational and mathematical methods in medicine,* vol. 2014, 2014.
[139] T. Elsheikh, R. Austin, D. Chhieng, F. Miller, A. Moriarty, and A. Renshaw, "American Society of Cytopathology. American Society of Cytopathology workload recommendations for automated Pap test screening: developed by the productivity and quality assurance in the era of automated screening task force," *Diagn Cytopathol,* vol. 41, pp. 174-8, 2013.
[140] N. H. S. C. S. Program, "Laboratory organization: a guide for laboratories participating in the NHS cervical Screening Programme," 2003.
[141] R. C. Mellors and R. Silver, "A microfluorometric scanner for the differential detection of cells: Application to exfoliative cytology," *Science,* vol. 114, pp. 356-360, 1951.
[142] W. E. Tolles and R. Bostrom, "Automatic screening of cytological smears for cancer: the instrumentation," *Annals of the New York Academy of Sciences,* vol. 63, pp. 1211-1218, 1956.
[143] C. C. Spencer and R. C. Bostrom, "Performance of the cytoanalyzer in recent clinical trials," *Journal of the National Cancer Institute,* vol. 29, pp. 267-276, 1962.
[144] A. Spriggs, R. Diamond, and E. Meyer, "Automated screening for cervical smears?," *The Lancet,* vol. 291, pp. 359-360, 1968.
[145] S. Watanabe, "An automated apparatus for cancer prescreening: CYBEST," *Computer Graphics and Image Processing,* vol. 3, pp. 350-358, 1974.

[146] J. Prewitt and M. L. Mendelsohn, "The analysis of cell images*," *Annals of the New York Academy of Sciences,* vol. 128, pp. 1035-1053, 1966.
[147] C. Bergmeir, M. G. Silvente, J. E. López-Cuervo, and J. Benítez, "Segmentation of cervical cell images using mean-shift filtering and morphological operators," in *SPIE Medical Imaging*, 2010, pp. 76234C-76234C-9.
[148] C. Bergmeir, M. García Silvente, and J. M. Benítez, "Segmentation of cervical cell nuclei in high-resolution microscopic images: A new algorithm and a web-based software framework," *Computer methods and programs in biomedicine,* vol. 107, pp. 497-512, 2012.
[149] P. Bamford and B. Lovell, "Unsupervised cell nucleus segmentation with active contours," *Signal Processing,* vol. 71, pp. 203-213, 1998.
[150] H. Abramczyk and B. Brozek-Pluska, "Raman imaging in biochemical and biomedical applications. Diagnosis and treatment of breast cancer," *Chemical reviews*, vol. 113, pp. 5766-5781, 2013.
[151] A. Böcking, J. Stockhausen, and D. Meyer-Ebrecht, "Towards a single cell cancer diagnosis. Multimodal and Monocellular Measurements of Markers and Morphology (5M)," *Analytical Cellular Pathology,* vol. 26, pp. 73-79, 2004.
[152] O. B. Ourselves, "Excerpts from changing bodies, changing lives," 2013-07-02.
[153] S. Brown, "The Science and Application of Hematoxylin and Eosin Staining," *Application Note*.
[154] T. M. Elsheikh, R. M. Austin, D. F. Chhieng, F. S. Miller, A. T. Moriarty, and A. A. Renshaw, "American society of cytopathology workload recommendations for automated pap test screening: developed by the productivity and quality assurance in the era of automated screening task force," *Diagnostic cytopathology,* vol. 41, pp. 174-178, 2013.
[155] R. Aloia, *General Principles* vol. 2: Elsevier, 1983.
[156] J. A. Kiernan, "Histological and histochemical methods: theory and practice," *Shock*, vol. 12, p. 479, 1999.
[157] A. H. Fischer, K. A. Jacobson, J. Rose, and R. Zeller, "Hematoxylin and eosin staining of tissue and cell sections," *Cold Spring Harbor Protocols,* vol. 2008, p. pdb. prot4986, 2008.
[158] L. E. Gerweck and K. Seetharaman, "Cellular pH gradient in tumor versus normal tissue: potential exploitation for the treatment of cancer," *Cancer research*, vol. 56, pp. 1194-1198, 1996.
[159] A. Walker, B. Walker, and A. Walker, "Faecal pH, dietary fibre intake, and proneness to colon cancer in four South African populations," *British journal of cancer*, vol. 53, p. 489, 1986.
[160] Y.-H. Li, L.-M. Chan, L. Tyer, R. T. Moody, C. M. Himel, and D. M. Hercules, "Solvent effects on the fluorescence of 1-(dimethylamino)-5-naphthalenesulfonic acid and related compounds," *Journal of the American Chemical Society*, vol. 97, pp. 3118-3126, 1975.
[161] D. Magde, G. E. Rojas, and P. G. Seybold, "Solvent dependence of the fluorescence lifetimes of xanthene dyes," *Photochemistry and Photobiology*, vol. 70, pp. 737-744, 1999.
[162] J. D. Bancroft and M. Gamble, *Theory and practice of histological techniques*: Elsevier Health Sciences, 2008.
[163] A. Waheed, K. S. Rao, and P. Gupta, "Mechanism of dye binding in the protein assay using eosin dyes," *Analytical biochemistry,* vol. 287, pp. 73-79, 2000.

[164] A. Waheed and P. Gupta, "Estimation of submicrogram quantities of protein using the dye eosin Y," *Journal of biochemical and biophysical methods*, vol. 42, pp. 125-132, 2000.
[165] H. H. Danielle M. Corgliano, Oliver Hofstetter, "Investigation of the stereoselectivity of an anti-amino acid antibody utilizing tryptophan fluorescence."
[166] K. M. Hanson, M. J. Behne, N. P. Barry, T. M. Mauro, E. Gratton, and R. M. Clegg, "Two-photon fluorescence lifetime imaging of the skin stratum corneum pH gradient," *Biophysical journal*, vol. 83, pp. 1682-1690, 2002.
[167] H.-J. Lin, P. Herman, J. S. Kang, and J. R. Lakowicz, "Fluorescence lifetime characterization of novel low-pH probes," *Analytical biochemistry*, vol. 294, pp. 118-125, 2001.
[168] H. J. Lin, P. Herman, and J. R. Lakowicz, "Fluorescence lifetime‐resolved pH imaging of living cells," *Cytometry Part A*, vol. 52, pp. 77-89, 2003.
[169] K. J. Newell and I. F. Tannock, "Reduction of intracellular pH as a possible mechanism for killing cells in acidic regions of solid tumors: effects of carbonylcyanide-3-chlorophenylhydrazone," *Cancer research*, vol. 49, pp. 4477-4482, 1989.
[170] I. F. Tannock and D. Rotin, "Acid pH in tumors and its potential for therapeutic exploitation," *Cancer research*, vol. 49, pp. 4373-4384, 1989.
[171] A. Hasim, A. Aili, A. Maimaiti, A. Abudula, and H. Upur, "Plasma-free amino acid profiling of cervical cancer and cervical intraepithelial neoplasia patients and its application for early detection," *Molecular biology reports*, vol. 40, pp. 5853-5859, 2013.
[172] F. M. Lyng, E. Ó. Faoláin, J. Conroy, A. D. Meade, P. Knief, B. Duffy, *et al.*, "Vibrational spectroscopy for cervical cancer pathology, from biochemical analysis to diagnostic tool," *Experimental and molecular pathology*, vol. 82, pp. 121-129, 2007.
[173] G. Anderson, J. Benedet, J. Le Riche, J. Matisic, and J. Thompson, "Invasive cancer of the cervix in British Columbia: a review of the demography and screening histories of 437 cases seen from 1985-1988," *Obstetrics & Gynecology*, vol. 80, pp. 1-4, 1992.
[174] J. W. Sellors and R. Sankaranarayanan, *Colposcopy and treatment of cervical intraepithelial neoplasia: a beginner's manual*: Diamond Pocket Books (P) Ltd., 2003.
[175] D. Koller and M. Sahami, "Toward optimal feature selection," 1996.